博士学位论文

DOCTORAL DISSERTATION

Central China Normal University

Wuhan, China

Non-Photonic Electron Angular Correlations with Charged Hadrons from the STAR Experiment: First Measurement of Bottom Contribution to Non-Photonic Electrons at RHIC

A dissertation submitted in partial fulfillment

of the requirements for the degree

Doctor of Philosophy in Physics

by

Xiaoyan Lin

Co-supervisors: Feng Liu, Huan Z. Huang

2007

To my parents and siblings

Table of Contents

List of Figures

List of Tables

Acknowledgments

First of all, I would like to acknowledge and extend my heartfelt gratitude to Prof. Lianshou Liu for introducing me into this field and for providing me with strong support and various opportunities to explore physics topics. I have greatly benefited from his broad knowledge of physics, sincere attitude on science and patience in supervising students. I also feel thankful to him for giving me an opportunity to study at UCLA.

I would like to express my deep gratitude to my co-supervisors, Prof. Feng Liu and Prof. Huan Z. Huang. Thanks for abundant fruitful discussions and for always guiding me in the right direction. Thanks for all of your help and tremendous support and for all the opportunities you have given me. My special thanks go to Prof. Charles A. Whitten Jr. for his generous help and support of me on my research. I appreciate his careful wording corrections on my thesis.

Special thanks should go to Dr. An Tai for guiding me into the heavy quark physics at the beginning of my PhD study. I would like to thank Dr. Weijiang Dong for providing and teaching me the BEMC reconstruction software. Thanks should also go to Prof. George Igo, Dr. Vahe Ghazikhanian, Dr. Jingguo Ma, Dr. Gang Wang, Priscilla Kurnadi, Jinhui Chen and all other members of the nuclear physics group at UCLA for their valuable discussions and the enjoyable time we had together.

The completion of this work would not have been possible without the efforts of the STAR collaboration and the RHIC operation group. Many thanks to the whole STAR collaboration and the RHIC CAD department. Special thanks to all the members of the STAR Heavy Flavor working group for their assistance, expertise and valuable discussions.

I would like to thank Prof. Hongfang Chen, Prof. Feng Liu, Prof. Lianshou Liu, Prof. Yugang Ma, Dr. Nu Xu and Prof. Charles A. Whitten Jr. for acting as the members of my dissertation committee.

I would like to give my thanks to Prof. Dexin Wang, who is not only a teacher but also a friend in life, for his help and friendship. Thanks should also go to Dr. Timothy

J. Hallman, Prof. Enke Wang, Prof. Fuqiang Wang, Prof. Yuanfang Wu and Prof. Jinhua Fu for their support.

I feel thankful to my classmate, also my best friend, Mingmei Xu for her help on many aspects of my life and for always standing by me. I am grateful to Yan Lv, Meiling Yu, Jiaxin Du and all other members of the high energy group at IOPP/CCNU for their helpful discussions and the joyful time we had together.

Thanks to Dr. Yifei Zhang, Dr. Haidong Liu, Dr. Haibin Zhang, Dr. Jing Liu, Dr. Aihong Tang, Dr. Zhangbu Xu, Dr. Ruan Lijuan and Dr. Chen Zhong for many helpful discussions and joyful time we had together at BNL. I would like to also thank my friends Yonghong Ren and Shaomei Yu for their kindly help on life during my living in Los Angeles.

Last but not least I would like to express my gratitude to my family for their unwavering support of me over many years.

Vita

1981	Born, Wenzhou, Zhejiang, P.R. China.
2003	B.S. in Physics, Central China Normal University, Wuhan, P.R. China.
2004-2006	Visiting student, University of California, Los Angeles, USA.
2003–present	PhD student, Central China Normal University, Wuhan, P.R. China.

Publications and Presentations

Xiaoyan Lin

Azimuthal Correlations between Non-Photonic Electrons and Charged Hadrons in p+p Collisions from STAR.

Nucl. Phys. **A783**, 497c-500c, 2007, nucl-ex/0609034.

Xiaoyan Lin

The first measurement of B meson semi-leptonic decay contribution to non-photonic electrons at RHIC.

J. Phys. G: Nucl. Part. Phys. **34** (in press), 2007, nucl-ex/0701050.

Xiaoyan Lin

Measurement of Non-Photonic Electron Angular Correlations with Charged Hadrons.

Int. J. Mod. Phys. **E** (in press), 2007, nucl-ex/0703039.

Xiaoyan Lin

D and B Meson Semileptonic Decay Contributions to the Non-Photonic Electrons.
Acta. Phys. Hung. **A**, ISBN: 963 86934 1 X (EP Systema, Budapest, 2006) 115-122.

Xiaoyan Lin
Non-Photonic Electron p_T Distributions and Correlations of Electrons from B and D Meson Decays with Charged Hadrons.
Submitted to Phys. Lett. B, hep-ph/0602067.

Xiaoyan Lin *et al.*
Scale for the Production of Jets in High Energy e^+e^- Collisions.
High Energy Physics and Nuclear Physics, Vol. **27**, No. 1, 7-11, 2003.

B.I. Abelev *et al.* [STAR Collaboration]
Energy dependence of $\pi^{\pm}$, p and $\bar{p}$ transverse momentum spectra for Au+Au collisions at $\sqrt{s_{\rm NN}} = 62.4$ and 200 GeV.
nucl-ex/0703040.

B.I. Abelev *et al.* [STAR Collaboration]
Partonic flow and Phi-meson production in Au + Au collisions at $\sqrt{s_{NN}} = 200$ GeV.
Submitted to Phys. Rev. Lett., nucl-ex/0703033.

B.I. Abelev *et al.* [STAR Collaboration]
Charged particle distributions and nuclear modification at high rapidities in d+Au collisions at $\sqrt{s_{NN}} = 200$ GeV.
Submitted to Phys. Lett. B, nucl-ex/0703016.

B.I. Abelev *et al.* [STAR Collaboration]
Mass, quark-number, and $\sqrt{s_{NN}}$ dependence of the second and fourth flow harmonics in ultra-relativistic nucleus-nucleus collisions.

Phys. Rev. **C75**, 054906, 2007, nucl-ex/0701010.

B.I. Abelev *et al.* [STAR Collaboration]
Rapidity and species dependence of particle production at large transverse momentum for d+Au collisions at $\sqrt{s_{NN}} = 200$ GeV.
nucl-ex/0609021.

B.I. Abelev *et al.* [STAR Collaboration]
Longitudinal double-spin asymmetry and cross section for inclusive jet production in polarized proton collisions at $\sqrt{s} = 200$ GeV.
Phys. Rev. Lett. **97**, 252001, 2006, hep-ex/0608030.

B.I. Abelev *et al.* [STAR Collaboration]
Neutral kaon interferometry in Au+Au collisions at $\sqrt{s_{NN}} = 200$ GeV.
Phys. Rev. **C74**, 054902, 2006, nucl-ex/0608012.

B.I. Abelev *et al.* [STAR Collaboration]
Strange particle production in p+p collisions at $\sqrt{s} = 200$ GeV.
Submitted to Phys. Rev. C, nucl-ex/0607033.

B.I. Abelev *et al.* [STAR Collaboration]
Transverse momentum and centrality dependence of high-p_T non-photonic electron suppression in Au+Au collisions at $\sqrt{s_{NN}} = 200$ GeV.
Submitted to Phys. Rev. Lett., nucl-ex/0607012.

B.I. Abelev *et al.* [STAR Collaboration]
Identified baryon and meson distributions at large transverse momenta from Au+Au collisions at $\sqrt{s_{NN}} = 200$ GeV.
Phys. Rev. Lett. **97**, 152301, 2006, nucl-ex/0606003.

Xiaoyan Lin

Studies of $D^{\star}$ Production in Au+Au and Cu+Cu Collisions at 200 GeV.

2^{nd} *Joint Meeting of the Nuclear Physics Divisions of the American Physical Society and The Physical Society of Japan, Kapalua, Maui, Hawaii, September 18-22, 2005.*

Xiaoyan Lin

The Study of D and B Meson Semi-leptonic Decay Contributions to the Non-photonic Electrons.

22^{nd} *Winter Workshop on Nuclear Dynamics, La Jolla, CA, USA, March 11-19, 2006.*

Xiaoyan Lin

Azimuthal Correlations between Non-Photonic Electrons and Charged Hadrons in p+p Collisions from STAR.

2^{nd} *International Conference on Hard and Electromagnetic Probes of High-Energy Nuclear Collisions (Hard Probes 2006), Asilomar Conference Grounds, Pacific Grove, CA, USA, June 9-16, 2006.*

Xiaoyan Lin

Study B and D Contributions to Non-Photonic Electrons via Azimuthal Correlations between Non-Photonic Electrons and Charged Hadrons.

The 19^{th} *International Conference on Ultra-Relativistic Nucleus-Nucleus Collisions (Quark Matter 2006), Shanghai, China, Nov. 14-20, 2006.*

Xiaoyan Lin

The First Measurement of B Contribution to Non-Photonic Electrons at RHIC using Azimuthal Correlations between Non-Photonic Electrons and Charged Hadrons.

XIth International Workshop on Correlation and Fluctuation in Multiparticle Production, Hangzhou, China, Nov. 21-24, 2006.

博士学位论文
DOCTORAL DISSERTATION

Abstract of the Dissertation

Non-Photonic Electron Angular Correlations with Charged Hadrons from the STAR Experiment: First Measurement of Bottom Contribution to Non-Photonic Electrons at RHIC

by

Xiaoyan Lin

Doctor of Philosophy in Physics

Central China Normal University, 2007

Professor Feng Liu, Co-supervisor

Professor Huan Z. Huang, Co-supervisor

Experimental results from the Relativistic Heavy Ion Collider (RHIC) have established the creation of an extremely dense partonic matter in central Au+Au collisions at RHIC. The measurements of suppression of high transverse momentum particles and azimuthal anisotropy v_2 for light hadrons have indicated partonic energy loss in the produced matter and the development of partonic collectivity in a very early stage of the collision. The study of energy loss and elliptic flow for hadrons carrying heavy quarks will complement these measurements and provide further insight into properties of the produced medium.

Recent experimental data from RHIC show that the nuclear modification factor of non-photonic electrons from heavy quark decays is comparable to that of light hadrons in central Au+Au collisions. This implies that heavy quarks lose a substantial amount of energy, in contradiction with existing theoretical predictions. The detailed comparison with experimental non-photonic electron energy loss depends on the relative contributions from D and B meson decays. Strong elliptic flow for non-photonic electrons has been observed recently, suggesting that charm quark carries a substantial amount of v_2. The non-photonic electron v_2 data show a tendency for the measured v_2 to decrease with

p_T at high p_T region, which could be an indication of increasing contribution to non-photonic electrons from B meson decays. The full understanding of the non-photonic electron energy loss and elliptic flow requires the knowledge of the relative D and B meson decay contributions to non-photonic electrons.

We here propose an innovative experimental method which uses the azimuthal correlations between non-photonic electrons and charged hadrons to estimate the relative contributions to non-photonic electron yield from D and B meson decays. Our method is based on the fact that for the same electron transverse momentum the near-side e-h azimuthal correlation from B decays is much wider than that from D decays. Correlations of non-photonic electrons with charged hadrons using PYTHIA Monte Carlo event generator in p+p collisions at $\sqrt{s_{NN}} = 200$ GeV are studied. The measurement of azimuthal correlations between non-photonic electrons and charged hadrons in p+p collisions at $\sqrt{s_{NN}} = 200$ GeV from the STAR experiment is presented. These analyses provide the first measurement of B meson semi-leptonic decay contribution to non-photonic electrons as a function of electron p_T for $p_T > 2.5$ GeV at RHIC.

Within the present statistical and systematic errors, our data analysis based on PYTHIA model indicates that at $p_T \sim 4.0 - 6.0$ GeV/c the measured B contribution to non-photonic electrons is comparable to the D contribution and that the measured $B/(B + D)$ ratios as a function of transverse momentum from 2.5 to 6.5 Gev/c are consistent with the FONLL theoretical calculation. Together with the observed large energy loss of non-photonic electrons and the decreasing value for the non-photonic electron v_2 at high p_T in Au+Au collisions, the measured $B/(B + D)$ ratios imply that the bottom quarks suffer considerable amount of energy loss in the dense QCD medium as well.

Keywords: Relativistic Heavy Ion Collision, Quark Gluon Plasma, Heavy Quark, Non-Photonic Electron, Semi-Leptonic Decay, Electron-Hadron Correlation, Bottom Production, Energy Loss, Elliptic Flow

中文摘要

用重味夸克半轻子衰变电子和带电强子的角关联首次测定RHIC能区底夸克和粲夸克半轻子衰变电子的相对产额

林晓燕

华中师范大学, 2007

自有生命以来人类对物质的结构以及组成物质的最小实体之间的相互作用的探讨做了永无止境的努力。在20世纪70年代所建立起来的标准模型里夸克和轻子是物质的最基本组元。自然界中存在着四种基本的相互作用力———万有引力，弱相互作用力，电磁相互作用力和强相互作用力。每一种力都以交换玻色传播子作为媒介，例如，胶子便是强相互作用的玻色传播子。

量子色动力学(QCD)是描述夸克－胶子相互作用的规范场理论。QCD有两个显著的基本特征：1)渐进自由：横动量交换越大或夸克之间的距离越小，夸克之间的相互作用越弱；2)夸克禁闭：夸克只能禁闭在强子物质内，目前还没有观测到孤立的夸克。QCD计算预言在高温和高能量密度的条件下会发生从普通强子物质到一种夸克解禁、局部热化的新的物质状态———夸克－胶子等离子体(QGP)的相变。在相对论重离子碰撞中，当两个接近光速的核彼此穿越时，将会在碰撞区域中产生极大的能量密度，这个能量密度可能会达到产生QGP的临界值。位于美国布鲁克海汶国家实验室(BNL)的相对论重离子对撞机(RHIC)为寻找QGP以及研究这种新的物质态的性质提供了一个前所未有的机会。

自2000年首次运行以来，RHIC已产生了大量的可喜实验结果。这些实验结果证实了在RHIC的金－金中心碰撞中已产生了一种极端稠密的不能用强子自由度来描述的部分子物质。大量的关于轻味强子的核修正因子(R_{AA}和R_{CP}) 和方位角各向异性分布(椭圆流v_2)的实验测量结果已经表明，部分子在碰撞所产生的高温高密物质中损失能量和部分子在碰撞早期形成集体流效应。带重味夸克(底夸克和粲夸克)的强子是研

究重离子碰撞产生的系统的早期状态动力学的理想探针。对带重味强子的能量损失和椭圆流的研究能够完善我们对物质能量损失机制以及集体流效应的认识，从而可以进一步了解相对论重离子碰撞中所产生的高温高密物质的性质。

由于受RHIC实验设备的限制，目前在RHIC直接测量底强子和粲强子非常困难，我们可以通过测量重味夸克半轻子衰变的产物间接地研究重味强子的性质。RHIC最新的实验数据表明，在高横动量区域由重味夸克半轻子衰变而来的电子(非光电子)的核修正因子和轻味强子的核修正因子具有相同的量级。这个重要的实验结果表明重味夸克穿过高温高密物质时有相当大的能量损失。这个实验现象和现有的理论预言相违背。原有的能损理论计算都是以胶子辐射做为主要的能损机制。这种能损机制预言重味夸克的能损会比轻味夸克的能损小很多，这是由于重味夸克的质量很大，“死角”效应(dead cone effect)会使重味夸克的胶子辐射压低。最近一些新的理论计算表明，对重味夸克来说，碰撞能量损失(弹性能量损失)可以和胶子辐射能量损失相比拟。这些包含胶子辐射和碰撞能量损失机制的理论计算可以改变重味夸克的能量损失，但仍然无法解释实验所测量的结果。这些理论计算中的一个主要的不确定性就是底夸克和粲夸克半轻子衰变电子的相对产额，特别是在高横动量区域。底夸克和粲夸克在QCD物质中的行为不一样，所承受的能损也不同。为了充分理解重味夸克的能量损失机制，我们需要测定底夸克和粲夸克半轻子衰变电子的相对产额。

在RHIC另一个重要的最新实验结果是在$p_T < 2$ GeV/c区域里观察到了很强的非光电子椭圆流，表明了粲夸克有相当的椭圆流，因为这个动量区域里的非光电子主要由粲夸克半轻子衰变而来。而在高横动量区域$p_T > 2$ GeV/c, 非光电子的椭圆流随着横动量的增大而减少。这一现象可以是底夸克对非光电子产额的贡献增大的迹象。由于底强子和粲强子的衰变运动学不同，相同的底强子和粲强子的椭圆流会导致很不一样的衰变电子椭圆流。为了充分地定量理解RHIC非光电子椭圆流的实验测量结果，我们也需要知道底夸克和粲夸克半轻子衰变电子的相对产额。

本论文中，我们利用重味夸克半轻子衰变电子和强子的角关联提出了一种具有创新意义的实验方法来测定底夸克和粲夸克半轻子衰变电子的相对产额。我们的方法基于这样的事实：对于相同电子横动量，底夸克衰变电子和强子的近角(伴随粒子和触发粒子在同一方向)关联分布比粲夸克衰变电子和强子的近角关联分布要宽很多。我们利用PYTHIA蒙特卡罗事件产生器研究了质心系能量200GeV的质子－质

子碰撞中重味夸克衰变电子和带电强子之间的关联。在实验数据分析上，我们利用RHIC－STAR实验组200GeV的质子－质子碰撞的实验数据测量了重味夸克半轻子衰变电子和带电强子的角关联。由这些分析我们首次测定了在RHIC上底夸克和粲夸克半轻子衰变电子的相对产额。

我们利用PYTHIA事件产生器产生了D介子和非光电子的横动量谱，并将其和STAR实验组所测量到的D介子和非光电子的横动量谱做了比较。我们发现为了让由PYTHIA产生的D介子谱和非光电子谱能同时描述STAR所测量的D介子谱和非光电子谱，D介子形成所需的碎裂函数将要比Peterson函数硬很多。我们用了δ函数作为粲夸克和底夸克的碎裂函数，产生了与实验相符合的D介子谱和非光电子谱。这种物理图像和夸克重组合模型相一致。同时，在PYTHIA 中我们研究了重味夸克半轻子衰变电子和带电强子的关联。我们发现触发电子和伴随强子的近角关联主要由衰变运动学决定，粒子产生的动力学对其影响很小，从而给出了测量底夸克和粲夸克半轻子衰变电子的相对产额的实验方法。

在STAR数据分析上，我们通过联合STAR时间投影室(TPC)给出的电离能损(dE/dx)，STAR电磁量能器(EMC)提供的能量信息和STAR－SMD给出的电磁簇射的大小和位置信息鉴别出电子(正电子)。光电子本底(主要由光子转换和中性π介子、η 介子达利兹衰变而来)通过重建标记电子(正电子)和伴随正电子(电子)的不变质量在统计上减除。光电子本底减除的效率从蒙特卡罗模拟中得到。我们给出了取得电子和强子角关联信号的详细流程，最后给出了实验上重味夸克半轻子衰变电子和带电强子的角关联分布。

利用由PYTHIA得到的底夸克半轻子衰变电子和带电强子的角关联分布以及粲夸克半轻子衰变电子和带电强子的角关联分布去拟合实验得到的角关联分布，并以底夸克半轻子衰变对非光电子产额的贡献做为拟合参数，便能得到底夸克和粲夸克半轻子衰变电子的相对产额。作为系统检查，我们在不同拟合范围上做了拟合，给出的结果在统计误差范围内相一致；同时，我们用了不同的拟合函数，得到的结果在统计误差范围内也是相符合的。PYTHIA蒙特卡罗事件产生器能够合理地模拟RHIC质子－质子碰撞事件。

在现有的统计和系统误差范围内，我们的数据分析结果表明，在$p_T \sim 4.0 - 6.0$ GeV/c的区域里，我们测量的底夸克半轻子衰变对非光电子产额的贡献可以和粲夸克

半轻子衰变的贡献相比拟。并且，我们的实验结果和FONLL微扰QCD理论计算结果相符合。同时，连同在金－金碰撞中所观测到的非光电子的能量损失以及在高横动量区域非光电子椭圆流随着横动量增大而减少的现象，我们测量的底夸克和粲夸克半轻子衰变电子的相对产额的实验结果意味着底夸克在高密的QCD物质中也将承受相当的能量损失。

我们的实验测量结果对于理解重味夸克能量损失机制和集体流效应，从而对于进一步理解高温高密QCD物质的性质具有重大的意义。

关键词：相对论重离子碰撞，夸克胶子等离子体，重味夸克，非光电子，半轻子衰变，电子－强子关联，底粒子产生，能量损失，椭圆流

CHAPTER 1

Introduction

The exploration of the structure and interactions for the smallest entities of the matter has been the non-ending endeavor of the human quest for the knowledge of Nature since the beginning of life. The Standard Model postulates that quarks and leptons are the most elementary building blocks of the matter. There are four forces in nature acting between these particles: gravitational, weak, electromagnetic and strong in order of increasing strength. Each of these forces is mediated by exchanging force bosons, e.g., gluons for the strong force.

Quantum Chromo-Dynamics (QCD) is the fundamental and precise theory for the interaction among quarks and gluons. There are two remarkable characteristics of QCD: asymptotic freedom and the confinement of quarks. QCD predicts a phase transition from hadronic matter into a new state of deconfined quarks and gluons, called the Quark Gluon Plasma (QGP), in environments at extreme temperatures and energy densities. In relativistic heavy ion collisions, when two nuclei, traveling at relativistic velocities, pass through each other, an enormous energy density is created which is high enough to reach the critical value where the QGP can exist. The Relativistic Heavy Ion Collider (RHIC) at Brookhaven National Laboratory (BNL) offers unprecedented opportunities to search for the QGP and to study the properties of the new state.

In this chapter we will recall some important features of QCD and present selected highlights from RHIC relevant to this dissertation.

1.1 Quarks, Gluons and Quantum Chromo-Dynamics

In the early 1970s deep inelastic electron collision experiments on protons indicated that nucleons that constitute atomic nuclei are themselves made of the most elementary particles — quarks and gluons. Today we know of six different types, or "flavors", of quarks, denoted u, d, s, c, b and t for up, down, strange, charm, bottom and top. Table. 1.1 presents the properties of quarks. A quark of a given flavor has three different color states: red, green and blue. The color-induced interactions, the so-called strong interactions, between quarks are mediated by gluons, which are massless bosons also carrying color charges themselves and therefore self-interacting. In nature we can only observe color neutral hadrons, the bound states of quarks. Gluons glue quarks either as a quark and an anti-quark pair (meson), or a triplet of quarks or anti-quarks (baryon).

Table 1.1: The properties of quarks.

Property	d	u	s	c	b	t
Q - electric charge	$-\frac{1}{3}$	$+\frac{2}{3}$	$-\frac{1}{3}$	$+\frac{2}{3}$	$-\frac{1}{3}$	$+\frac{2}{3}$
I_z - isospin z-component	$-\frac{1}{2}$	$+\frac{1}{2}$	0	0	0	0
S - strangeness	0	0	-1	0	0	0
C - charmness	0	0	0	$+1$	0	0
B - bottomness	0	0	0	0	-1	0
T - topness	0	0	0	0	0	$+1$

The theory of quark-gluon interactions is governed by Quantum Chromo-Dynamics (QCD) [Wil82]. QCD is the unbroken $SU(3)$ color non-Abelian gauge theory to describe the strong interactions, and together with the spontaneously broken $SU(2) \times U(1)$ electroweak theory, establishes the two basic components of the Standard Model of particle physics. QCD is an expanded version of the very successful theory of Quantum Electro-Dynamics (QED). Both QCD and QED are based on Quantum Field theory. However, there are crucial differences between QCD and QED. There is only one electric charge

in QED, and the electromagnetic force bosons, photons, are electric charge neutral and do not self-interact. On the other hand the color charge in QCD has three components. Quarks change their color states by emitting or absorbing gluons. Due to the color conservation, gluons are required to also carry color charge and as a result self-interact. In fact, it is the gluon self-interaction that makes QCD dynamics so peculiar [Kho04].

For the electromagnetic force in QED, the coupling constant $\alpha = \frac{1}{137}$ is much less than unity and the use of perturbation theory is well established in QED. However, the gluon self-interactions lead to a completely different coupling constant in QCD. The effective coupling constant of strong interaction, α_s, has been experimentally measured to be a function strongly depending on the distance of interaction or the momentum transfer, written as:

$$\alpha_s(Q^2) \approx \frac{12\pi}{\beta_0 \ln(Q^2/\Lambda_{QCD})} \tag{1.1}$$

where Q^2 is the momentum transfer, Λ_{QCD} is the famous QCD scale and β_0 is a constant. Fig. 1.1 shows the strong coupling constant, α_s, at different momentum transfer, Q, from various experiments as well as the QCD calculations.

The behavior in QCD running coupling constant illustrates two remarkable features of QCD. α_S becomes very small at very high momentum transfers or very short distances; thus quarks and gluons interact very weakly. This is known as asymptotic freedom [GW73, Pol73], which was first discovered in the early 1970s and honored by a Nobel Prize in 2004. At large distances or small momentum transfers, α_S becomes strong. The larger the distance that two quarks are separated the stronger the coupling; and thus the more self-coupled gluons holding the quarks together. That means an infinite amount of energy is needed to separate two quarks. As a result there are no isolated quarks and quarks are bound into color neutral hadrons. This is known as quark/color confinement. The confinement principle has never been rigorously proved. However, all experimental results concerning hadrons unambiguously support the quark/color confinement.

Accordingly, QCD yields two qualitatively different pictures to describe quark-gluon

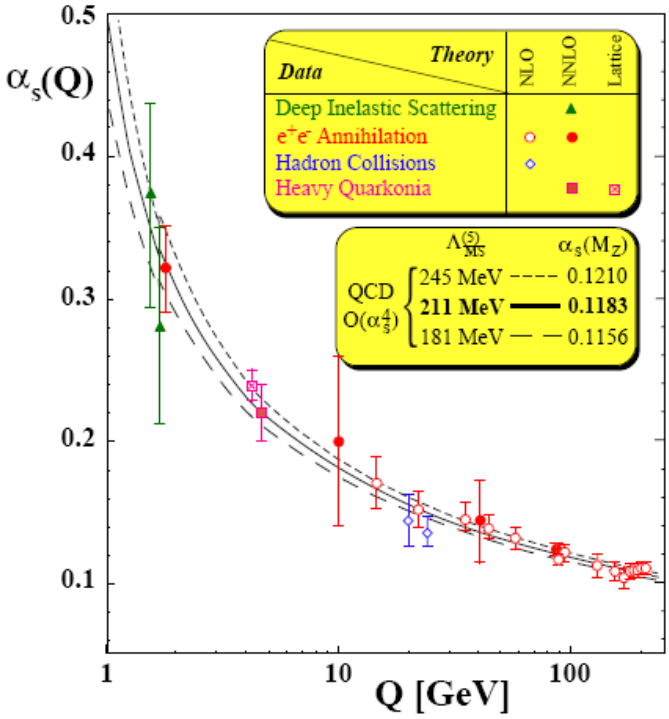

Figure 1.1: The measured QCD running coupling constant α_s from a variety of experiments compared to the QCD prediction [Bet03].

interactions. In the regime where the momentum transfer is high, i.e., the distance of interaction is small, perturbative expansions in α_s are applicable. Physics observables can be calculated in a truncated series as leading order (LO), next-to-leading order (NLO), etc. Over the past decades, there are plenty of experiments on hard processes providing quantitative tests on the validity of the perturbative QCD (pQCD) calculations. pQCD has been proven to describe a large set of high energy, large momentum transfer processes with high accuracy.

The non-perturbative quark-gluon interactions at long distances, i.e., at small momentum transfers, are always present in any process involving the strong interaction. Physicists have made significant efforts to bridge the gap between perturbative and non-perturbative regimes. Powerful numerical methods of solving QCD on a lattice of space

and time (LQCD) have been developed. The principle of LQCD is to replace continuous space-time with a discrete lattice. LQCD needs no additional assumption beyond QCD. It has exactly as many free parameters as QCD itself, which are the strong coupling constant and one mass per quark species [Pen95]. Although the performance is limited by computer memory and speed, LQCD provides a mathematically well-defined framework for non-perturbative QCD.

1.2 Quark-Gluon Plasma and Relativistic Heavy Ion Collisions

Owing to the asymptotic freedom property of QCD, it has been realized that at sufficiently high energy density hadronic matter should turn into an ultra-dense form of matter with deconfined quarks and gluons [CP75b, CP75a]. The (locally) thermally equilibrated quark-gluon system, where the color degrees of freedom become effective, is what we call Quark-Gluon Plasma (QGP). Fig. 1.2 shows a schematic picture of the phase diagram for the hadronic and deconfined quark matter. This phase transition occurs when the energy density is high enough, about an order of magnitude larger than the energy density inside of atomic nuclei, either due to the high temperature or large baryon chemical potential.

More information on this transition to the QGP is available from numerical studies by LQCD. Fig. 1.3 shows the energy density scaled by T^4 as a function of temperature scaled by the critical temperature T_c from lattice QCD [Kar02]. There is a rapid rise and saturation of the energy density for the matter when the temperature approaches $T \approx T_c \sim 160$ MeV. The energy density changes by about an order of magnitude. The level of saturation reflects the number of degrees of freedom. This rapid change in the energy density corresponds to a change in the degrees of freedom between the confined and deconfined matters, i.e., a phase transition from the hadronic matter to the QGP. The arrows are the Stefan-Boltzmann limits for an ideal gas, where quarks are massless and quarks and gluons are non-interacting. The deviation of the energy density from the Stefan-Boltzmann limit indicates that besides the effect of quark mass, there should

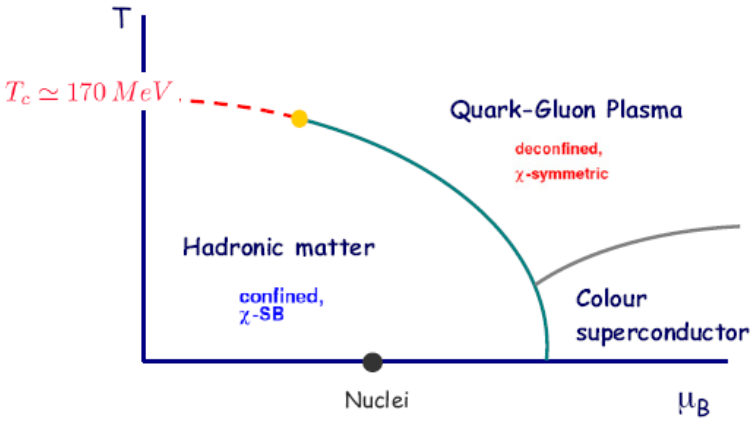

Figure 1.2: A schematic representation of QCD phase diagram in the plane of temperature (T) and baryon chemical potential (μ_B). Figure taken from [Bla06].

be substantial interactions among quarks and gluons in the newly formed QGP phase.

The QGP is believed to exist in the early Universe, on the order of microsecond after the Big Bang, and may exist in the cores of many neutron stars. In 1974, T.D. Lee suggested, "It would be interesting to explore new phenomena by distributing high energy or high nuclear density over a relatively large volume." [Lee74, LW74] It was pointed out by W. Greiner and collaborators that the required high density for the QGP could be achieved from relativistic heavy ion collisions [HSS74, Bau75]. Since then, scientists have been building facilities with higher and higher energies in order to reach and cross the phase transition boundary in the laboratory. The first measurements were made at the BEVALAC in the Lawrence Berkeley National Laboratory (LBNL) in the early 1980s with fixed target energies ranging up to 2 GeV per projectile nucleon, followed by the Schwerionensynchrotron (SIS) at the Gesellschaft Schwerionenforschung (GSI) in Darmstadt with a similar energy range. The Alternating Gradient Synchrotron (AGS) at Brookhaven National Lab (BNL) in the late 1980s could accelerate gold beams up to an energy of 11.7 GeV per nucleon. The Super Proton Synchrotron (SPS) at

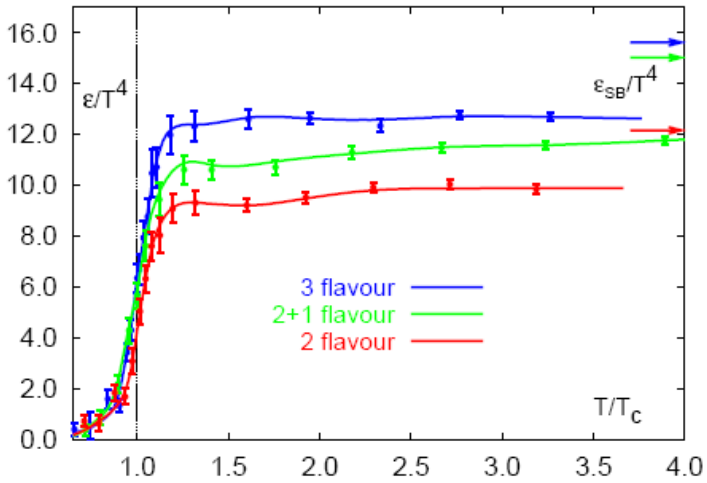

Figure 1.3: The energy density scaled by T^4 as a function of temperature scaled by the critical temperature T_c. Various number of dynamical quark flavors are considered. The arrows are the corresponding Stefan-Boltzmann values for asymptotically high temperature. Figure taken from [Kar02].

European laboratory for particle physics (CERN) also in the late 1980s can accelerate lead-ion beam up to an energy of 158 GeV per nucleon and allows the lead-lead collisions with up to $\sqrt{s_{NN}} = 17.3$ GeV. The Relativistic Heavy Ion Collider (RHIC) at BNL was commissioned in 1999. It is the first heavy ion collider and was originally designed for head-on Au+Au collisions at $\sqrt{s_{NN}} = 200$ GeV. See more details on the RHIC facility in section 2.1. The Large Hadron Collider (LHC) is being built at CERN and is expected to start running in this year (2007). It is originally designed for p+p collisions for energies up to $\sqrt{s_{NN}} = 14$ TeV. It will also collide lead ions up to energies of $\sqrt{s_{NN}} = 5.5$ TeV.

The space-time evolution of a heavy ion collision with the formation of QGP is illustrated in Fig. 1.4. Two nuclei appear as thin disks approaching each other at nearly the speed of light because of Lorentz contraction. After they smash into and pass through one another, a huge amount of the energy that they carried before the collision is deposited in the interaction region. Quarks and gluons will be deconfined and form

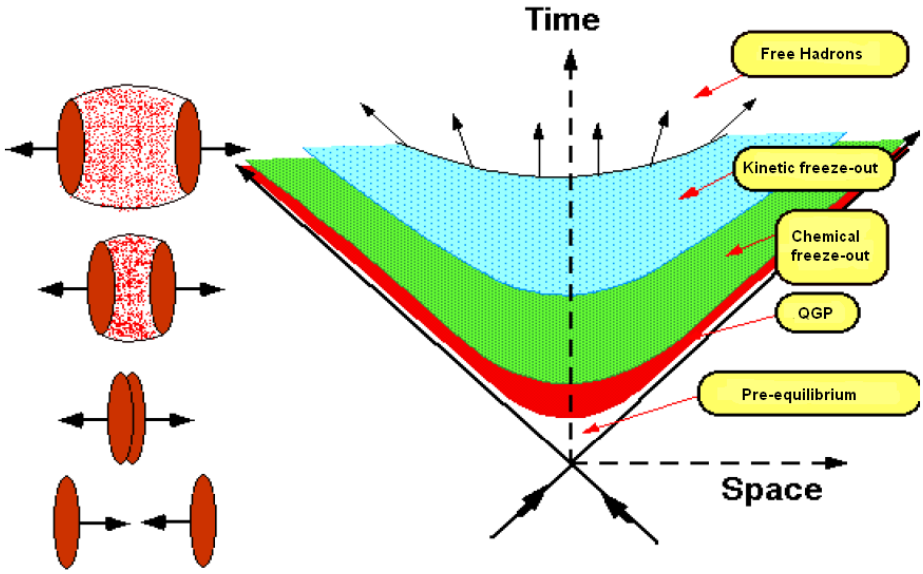

Figure 1.4: The space-time diagram of a heavy ion collision with the formation of QGP.

a quark-gluon system if the temperature exceeds the critical temperature T_c. The large interaction cross section between quarks and gluons eventually bring the system into a (locally) thermal equilibrium and the QGP is formed. The lifetime of the QGP is very short. The system immediately starts expanding and cooling down. Hadronization takes place until the chemical freeze out temperature T_{ch} is reached, when inelastic scattering ceases and the particle species are no longer changed by collisions but only by decays. The system continues expanding and cooling until elastic collisions between hadrons stop at the kinetic freeze out temperature T_{fo}, and the momentum distributions of particles are fixed. The produced particles blast out from the collision region and eventually stream into detectors.

Experimentally, we look at the information provided by the particles in the final stage to probe the properties of QGP. The RHIC experiments have produced a large body of high quality data. The early results reveal that an extremely dense, rapidly thermalizing matter which exhibits partonic degrees of freedom is produced in central Au+Au

collisions at RHIC. These results are comprehensively summarized in Ref. [Ada05a] and a number of reviews [JW05, Ris04, KH03, GVW03, BSZ00, TW02]. In the following sections, we will present selected highlights from RHIC relevant to this thesis.

1.3 Partonic Energy Loss in Dense QCD Medium

High momentum partons from hard scatterings have been used to study the energy loss of partons when traversing the dense matter. It was first proposed by Bjoken in 1982 that partons traversing bulk partonic matter might undergo significant energy loss [Bjo82]. The idea was further developed by X.N. Wang and M. Gyullasy [WG92]. Two experimental variables have been extensively used to describe the change in the p_T spectra due to energy loss of high momentum partons in the dense matter. One is called the nuclear modification factor R_{AA}, which is the comparison of the spectra in A+A collisions through those in p+p collisions, scaled by the number of binary nucleon-nucleon collisions:

$$R_{AA} = \frac{d^2N^{AA}/dp_T d\eta}{T_{AA} d^2\sigma^{pp}/dp_T d\eta} \tag{1.2}$$

where $T_{AA} =< N_{binary} > /\sigma_{inel}^{NN}$ accounts for the collision geometry, calculated from a Glauber model [Won94]. N_{binary} denotes for the number of binary inelastic nucleon-nucleon collisions, and σ_{inel}^{NN} is the inelastic cross section of nucleon-nucleon collisions. The other variable is the nuclear modification factor R_{CP}, which is defined by the ratio of the particle yield scaled by N_{binary} from central and peripheral collisions:

$$R_{CP} = \frac{(dN^{central}/dp_T)/N_{binary}^{central}}{(dN^{peripheral}/dp_T)/N_{binary}^{peripheral}} \tag{1.3}$$

These nuclear modification factors would be unity in the absence of nuclear effects.

A strong suppression, with R_{AA} or $R_{CP} \sim 0.2 << 1$, has been observed in Au+Au collisions for momentum up to $p_T \sim 10$ GeV [Adl03b, Ada03, Adl06a, Abe06a], which is one of the most exciting discoveries at RHIC, confirming the strong final state interactions of the high momentum partons with the surrounding dense matter.

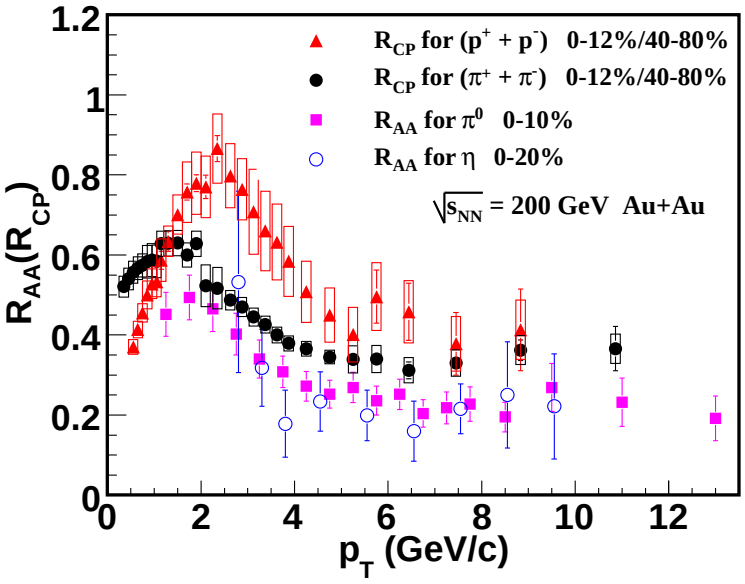

Figure 1.5: Nuclear modification factors R_{CP} for $\pi^+ + \pi^-$ and $p + \bar{p}$ from STAR and R_{AA} for π^0 and η from PHENIX. The boxes (bars) on the STAR data are systematic (statistical) errors. The PHENIX errors contain point-to-point statistical and systematic errors. Note the centrality definition is different for the STAR and PHENIX data.

Fig. 1.5 shows the nuclear modification factors R_{CP} for $\pi^+ + \pi^-$ and $p + \bar{p}$ from STAR [Abe06a] and R_{AA} for π^0 and η from PHENIX [Adl06a]. In the region of p_T greater than 6 GeV/c, there is common magnitude of suppression for π^0 and η, and the difference between charged π and protons (anti-protons) disappears. These observations indicate that the parent partons first lose energy in the produced dense medium and then fragment into particles. The R_{AA} (R_{CP}) would be particle dependent at high p_T if the energy loss were dominantly from hadronic stage since these particles have very different hadronic re-scattering cross sections. The data have experimentally established that the energy loss processes take place in the partonic level not in the hardonic level, favoring the assumption in theoretical calculations of jet quenching [GVW01, VG02, ADS05]. Gluon and quark jet fragmentations have different contributions to baryons and mesons, and baryons are more likely from gluon fragmentations at high p_T [Abr00]. The similarity

of the nuclear modification factor for protons (anti-protons) and charged pions at $p_T >$ 6 GeV/c from the STAR measurement indicates that there is no manifestation of a different energy loss for quarks and gluons, which is in contradiction to the theoretical expectation of a large difference between quark and gluon energy loss.

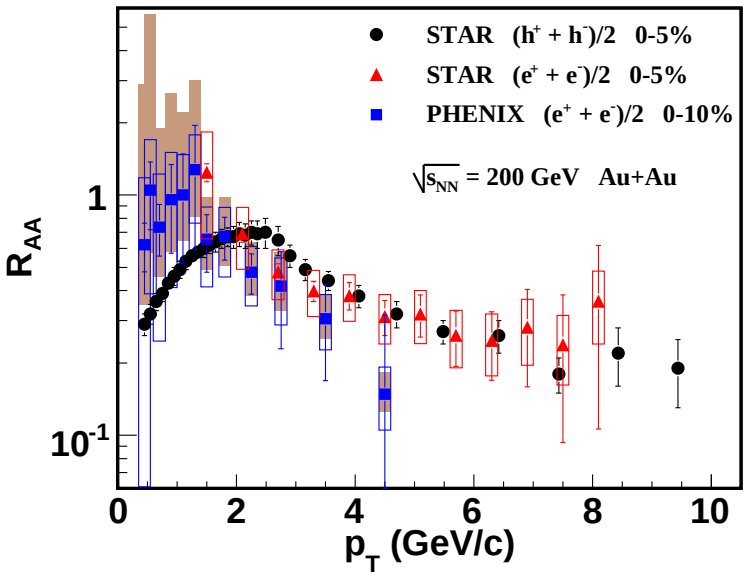

Figure 1.6: Nuclear modification factor R_{AA} of non-photonic electrons from heavy quark semi-leptonic decays from STAR and PHENIX in comparison with that of charged hadrons from STAR.

Fig. 1.6 shows nuclear modification factor R_{AA} of non-photonic electrons from STAR [Abe06b] and PHENIX [Adl06b] measurements, as well as the STAR measured charged hadron R_{AA} [Ada03]. The boxes (bars) on the STAR electron data indicate the size of systematic (statistical) errors. The error bars on the PHENIX data are statistical only. The filled boxes (open boxes) on the PHENIX data indicate the systematic errors related to the uncertainties in Au+Au (p+p) measurements. The error bars on the STAR charged hadron data represent the quadrature sum of the Au+Au and p+p spectrum uncertainties. The STAR and PHENIX electron R_{AA} data are consistent with each other within statistical and systematic errors in the overlapping p_T region. At

high p_T suppression of non-photonic electrons is similar to that for light hadrons. Non-photonic electrons are primarily from semi-leptonic decays of hadrons carrying heavy quarks. The suppression of non-photonic electrons indicates substantial energy loss for heavy quarks. These measurements imply that there is no significant difference between heavy quark and light quark energy loss, in contradiction to theoretical expectations that heavy quarks would loss much less energy [DK01]. This small flavor dependence of the parton energy loss forces us to investigate more deeply the issue of parton energy loss, both theoretically and experimentally. See more discussions on heavy quark energy loss in section 1.5.2.

1.4 Hadronization of Bulk Partonic Matter

The STAR measured R_{CP} derived from the most central 5% to the peripheral $40-60\%$ Au+Au collision centralities are shown in Fig. 1.7 for identified mesons (in panel a) and baryons (in panel b) [Sch04]. The dot-dashed line is the R_{CP} of charged hadrons for reference. In the low p_T region particle production is dominated by number of participant scaling. In the intermediate p_T range at $2 < p_T < 6$ GeV/c, the p_T dependence of R_{CP} falls into two groups, one for mesons and one for baryons, and there is little mass difference among the mesons and among the baryons. This observation suggests that there is a dependence on the number of constituent quarks. The meson and baryon values appear to merge above a p_T of 6 GeV/c, where parton fragmentation becomes important. This unique dependence on the number of constituent quarks indicates the production dynamics in the intermediate p_T region is different from both fragmentation at high p_T and hydrodynamic behavior at low p_T.

In a non-central nucleus-nucleus collision the overlapping participants form the shape of an almond. The anisotropic pressure gradients will lead to an azimuthal anisotropy in transverse momentum space in the final state. The azimuthal angular particle distribution can be expanded into a Fourier series,

$$\frac{d^2n}{p_T dp_T d\phi} \propto (1 + 2\sum_n v_n \cos n(\phi - \Psi_R)) \tag{1.4}$$

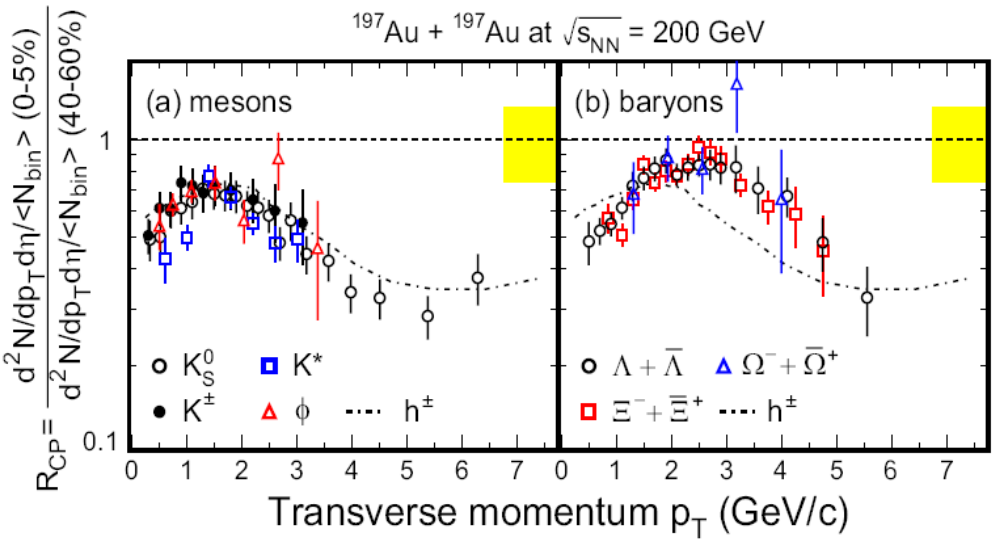

Figure 1.7: The STAR measured nuclear modification factor R_{CP} of identified mesons (panel a) and baryons (panel b) from Au+Au collisions at $\sqrt{s_{NN}}$ = 200 GeV in comparison with that of charge hadrons in dot-dashed line. The error bars on the data points include both statistical and systematic uncertainties. The shaded bands around 1 represent the systematic uncertainty in the N_{binary} calculation, based on the Glauber model.

where ϕ is the azimuthal angle of the particles, Ψ_R is the reaction plane[1] angle and v_2 is called the elliptic flow parameter [Sor99]. Elliptic flow is expected to be sensitive to the early stages of system evolution.

Fig. 1.8 shows v_2 as a function of p_T for the identified particles from STAR [Ada04] and PHENIX [Adl03a] measurements, together with the hydrodynamic model predictions [HKH01]. In the low p_T region at $p_T < 2$ GeV/c, particles exhibit hydrodynamic behavior, and there is a mass dependence of v_2. The agreement with the hydrodynamic model implies that the collective motion develops in the very early stages of the reaction. At the intermediate p_T region, the hydrodynamic calculations overpredict the flow. The

[1]The reaction plane is defined by the vectors x (impact parameter direction) and z (beam direction).

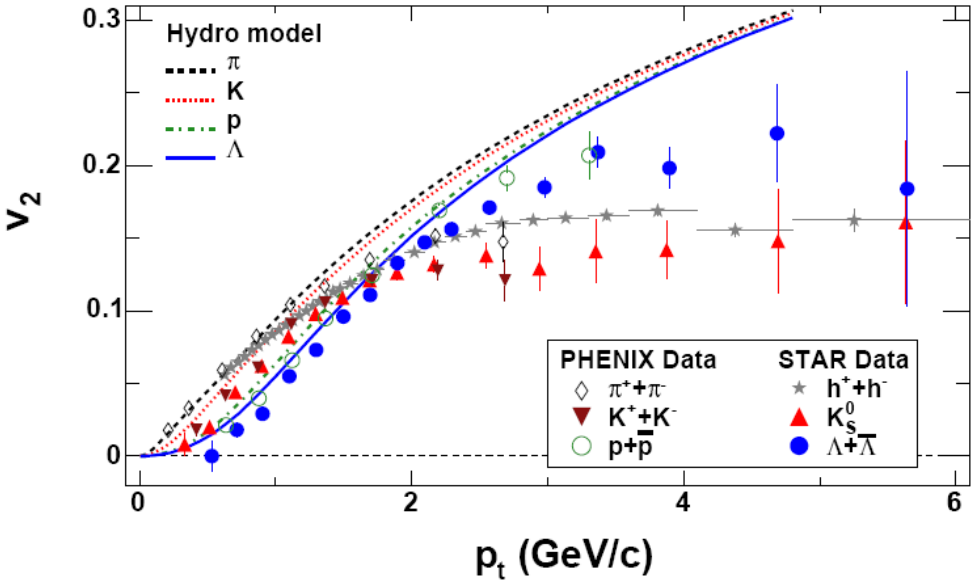

Figure 1.8: Azimuthal angular anisotropy v_2 as a function of p_T for the identified particles from STAR [Ada04] and PHENIX [Adl03a] in minimum bias Au+Au collisions at $\sqrt{s_{NN}} = 200$ GeV. The hydrodynamic calculations are from Ref. [HKH01].

v_2 values do not strongly depend on p_T in this region, and there is a distinct grouping among mesons and baryons. After scaling both v_2 and p_T by the number of constituent quarks in the corresponding particle as shown in Fig. 1.9, in the intermediate p_T region the data points fall approximately onto a single curve except pions (due to resonance decay effects [GK04, DES04]). Systematic deviation as a function of particle masses at low p_T is attributed to hydrodynamic behavior and also the detailed internal structure of hadrons [MFB05].

Quark coalescences and recombination models [MV03, HY03b, GKL03, FMN03] for hadron formation through multi-parton dynamics offer an elegant interpretation for the experimental feature of constituent quark number scaling in the nuclear modification factors and the elliptic flow in the intermediate p_T region. Hadrons are formed through coalescing of constituent quarks, which pre-exist and carry an azimuthal angu-

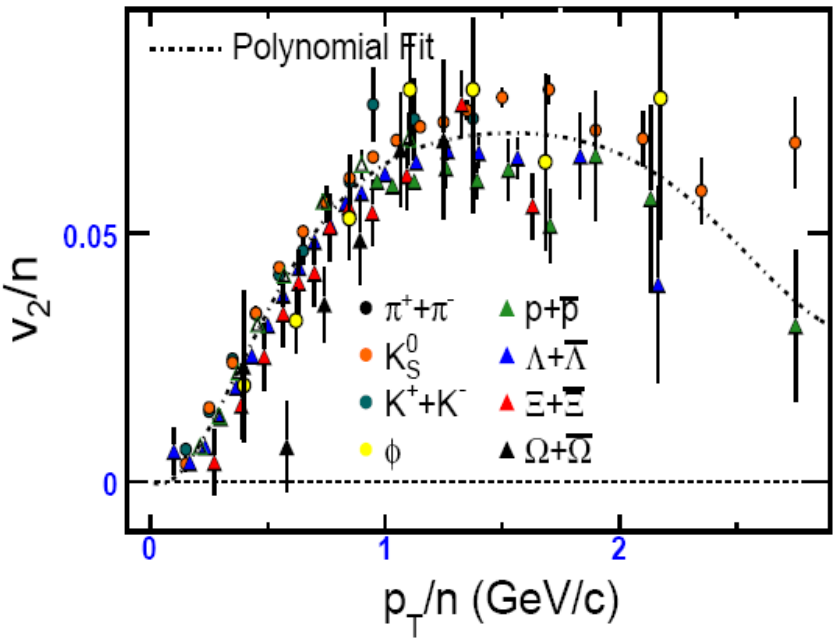

Figure 1.9: v_2/n as a function of p_T/n for identified particles from STAR and PHENIX measurements [Sor06], where n is the the number of constituent quarks. The dot-dashed line is a polynomial fit to the available data.

lar anisotropy before hadronization.

The measured features at intermediate p_T originate from partonic nature of the matter; and they have provided the most direct experimental evidence for the creation of deconfined partonic matter in nucleus-nucleus collisions at RHIC.

1.5 Non-Photonic Electron Measurement at RHIC

Heavy quarks are believed to be produced through initial parton-parton, mostly gluon-gluon, scatterings in nuclear collisions at the Relativistic Heavy Ion Collider (RHIC) energies. Theoretical calculations of heavy quark production within the perturbative Quantum Chromo-Dynamics (pQCD) framework are considered more reliable because

the heavy quark mass sets a natural scale for the pQCD. The transport dynamics of the heavy quarks in nuclear medium such as flow [GKR04] and energy loss [DK01, ZWW04] can probe QCD properties of the dense matter created in nucleus-nucleus collisions. Therefore, heavy quark measurements provide unique insights into QCD properties of the new state of matter produced in nucleus-nucleus collisions.

At RHIC, two different experimental approaches are carried out to study the open heavy flavors in relativistic heavy ion collisions. One is the direct reconstruction of heavy flavored mesons through hadronic decay channels, which is only performed by the STAR experiment. The other one is the indirect measurement via semi-leptonic decays of heavy flavored mesons (identified non-photonic/single electrons or single muons), which can be done by both STAR and PHENIX experiments. Experimentally, the direct reconstruction of D mesons is difficult because of their short lifetime, low production rates and large combinatorial background in the heavy ion environment. Statistical issues currently limit the D meson reconstruction to the low p_T region of $p_T < 3.0$ GeV/c [Ada05b]. Thus the indirect measurement through semi-leptonic decays can extend the capability to study heavy flavor production. In this section, we will address recent results from the non-photonic electron measurement at RHIC.

1.5.1 Non-Photonic Electron Spectrum

The left panel of Fig. 1.10 shows the background subtracted non-photonic electron spectra from STAR [Ada05b, Abe06b] and PHENIX [Ada06b] measurements in p+p collisions at $\sqrt{s_{NN}} = 200$ GeV together with the uncertainty band from a fixed-order-plus-next-to-leading-log (FONLL) pQCD calculation [CNV05] for non-photonic electron yield in p+p collisions. STAR has two independent electron measurements, with the Time Projection Chamber (TPC) and the Time of Flight (ToF) data for low p_T ($p_T < 4 - 5$ GeV/c) electrons shown as triangles in the plot, and with the Electro-Magnetic Calorimeter (EMC) data for high p_T ($p_T > 1.5$ GeV/c) electrons shown as black solid circles in the plot. The results from these two measurements are consistent with each other in the overlapping region. However, there are discrepancies between

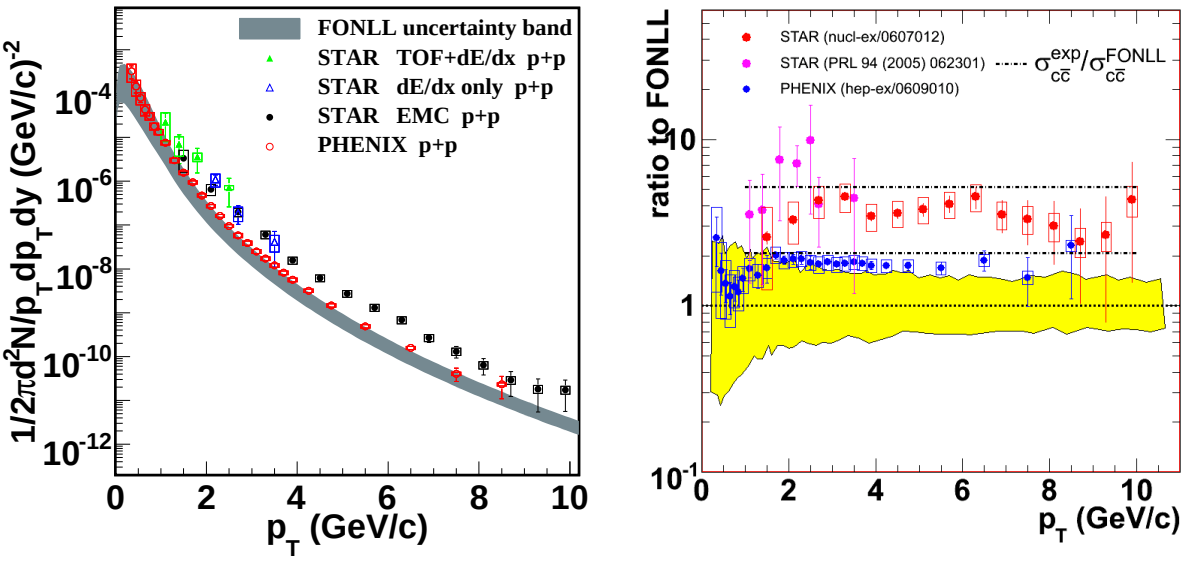

Figure 1.10: Left: Non-photonic electron spectra from STAR [Ada05b, Abe06b] and PHENIX [Ada06b] measurements in p+p collisions at $\sqrt{s_{NN}}$ = 200 GeV. The bars (boxes) indicate the size of statistical (systematic) errors. The band is the theoretical uncertainty of the FONLL pQCD predication for the non-photonic electron yield in p+p collisions [CNV05]. Right: Ratio of the measured non-photonic electron yield to the FONLL pQCD calculation in p+p collisions.

STAR and PHENIX measurements, and between STAR and the FONLL calculation. The right panel of Fig. 1.10 shows the ratio of STAR and PHENIX measured non-photonic electron yields to the FONLL calculated non-photonic electron yield in p+p collisions. The FONLL calculation shows large uncertainties (yellow band) due to parameter choices of quark masses, factorization and renormalization scales, etc. The upper limit of the FONLL calculation is compatible with the PHENIX data. The STAR non-photonic electron production is ~ 5 times larger than predicted by the FONLL calculation. However, the FONLL calculation can describe the shape of measured spectra reasonably well. The dashed lines are the ratio of STAR and PHENIX measured total charm cross section to the FONLL calculation. A factor of ~ 2 discrepancy can be

seen between STAR and PHENIX measurements. The total charm cross section from STAR is derived by a combined fit of three independent measurements: direct reconstruction of D meson, measurement of single muons and measurement of non-photonic electrons [Zho07], while PHENIX obtained the total charm cross section by integrating the non-photonic electron cross section for $p_T > 0.4$ GeV/c [Ada06b]. The capability to direct reconstruct D meson is an advantage for the STAR experiment, while the PHENIX experiment has superior signal to background ratio for the measurement of non-photonic electrons due to reduced amount of detector material compared to STAR.

The reason for the discrepancy between the two experiments remains open. STAR will have a low detector material run next year which will reduce the yield of background photonic electrons and thus the systematic uncertainty will be re-addressed. Besides, both STAR and PHENIX are developing vertex detector upgrades. The high precision measurements of vertex position provided by the vertex detectors will allow clean D and B meson samples in the future.

1.5.2 Non-Photonic Electron Energy Loss

Experimental results from RHIC over the past years have established that dense partonic matter is created in Au+Au collisions at RHIC. The study of flavor dependence in partonic energy loss will expand our understanding of the properties of the hot and dense nuclear matter. The disagreement between STAR and PHENIX non-photonic electron measurements is a common normalization factor to p+p and Au+Au collisions, thus giving the consistent nuclear modification factor R_{AA} for non-photonic electrons in the overlapping p_T region as we've already seen in Fig. 1.6.

The energy loss mechanism via gluon radiation caused by the propagation of a fast parton (quark) through the QCD medium has successfully described the light hadron suppression at RHIC [AG04, Vit06]. Gluon bremsstrahlung off a heavy quark is different from the case of a massless parton. Gluon radiation is suppressed at angles smaller than the ratio of the quark mass to its energy [DK01] — the dead cone effect. The suppression of small-angle radiation results in a much smaller heavy quark quenching.

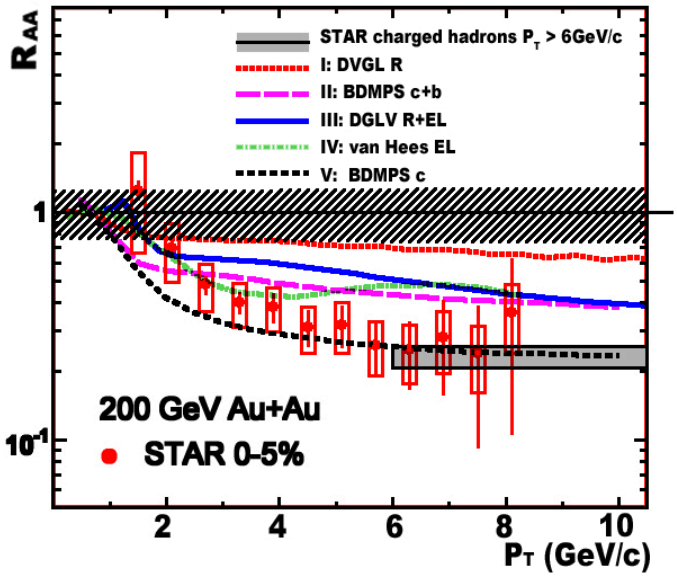

Figure 1.11: Several theoretical calculations of nuclear modification factor R_{AA} for non-photonic electrons in central Au+Au collisions at $\sqrt{s_{NN}}$ = 200 GeV in comparison with the STAR measurement.

In contrast to this expectation a strong suppression of non-photonic electrons has been observed in central Au+Au collisions at RHIC, as shown in Fig. 1.6. This implies that heavy quarks lose a substantial amount of energy, which cannot be explained by current theoretical predictions based on gluon radiation as the dominant mechanism for energy loss [ADS05, DGV06].

Fig. 1.11 shows several theoretical calculations of non-photonic electron suppression in central Au+Au collisions in comparison with the STAR data. Curve-I is from DGLV theory [DGV06] based on the medium induced gluon radiation energy loss mechanism with the default gluon density, $dN_g/dy = 1000$, which is used to describe light quark suppression. Curve-II is from BDMPS theory [ACD06] with a transport coefficient $\hat{q} = 14$ GeV^2/fm, which also assumes gluon radiation as the energy loss mechanism. Both curve-I and curve-II cannot describe the observed data. Recent calculations show that the collisional energy loss for heavy quarks is comparable to the radiation energy

loss [Mus05], and this will contribute to R_{AA}. Curve-III is based on the same theory as curve-I but includes both radiation and collisional energy loss [WHD05]. This calculation changes the heavy quark energy loss, but still predicts less suppression than observed. The heavy quark energy loss in curve-IV is introduced by the elastic rescattering of heavy quarks in the medium [HGR06]. This calculation also failed to describe the observed suppression.

Note that the calculations from curve-I to curve-IV all take the relative contributions of D and B mesons from the pQCD calculations [CNV05], where B decay contribution to non-photonic electrons becomes larger than that from D decays at $p_T \sim 4$ GeV/c. Electrons from bottom quarks are much less quenched than that from charm quarks due to the larger mass of their quark parents [DGV06]. Interestingly, curve-V in Fig. 1.11, which is the same calculation as curve-II but only takes the electrons from charm quarks, can reasonably describe the measured suppression.

One of the major, both experimental and theoretical, uncertainties is the relative charm and bottom decay contributions to the yield of non-photonic electrons at high p_T. The full understanding of non-photonic electron (heavy quark) energy loss motivates the measurement of the relative contributions to non-photonic electrons from D and B meson semi-leptonic decays.

1.5.3 Non-Photonic Electron Elliptic Flow

As discussed in section 1.4, the v_2 of light hadrons in the low p_T region can be well produced by the hydrodynamic model, indicating early thermalization and strongly interacting matter in the early stages of the collisions; and the characteristics of light hadrons at the intermediate p_T region, which can be explained by the quark coalescence model, suggests that the v_2 is largely developed in the partonic phase. The measurement of heavy quark v_2 will complement these observations. If heavy quark flows, it will support partonic level thermalization. If the heavy quark v_2 follows the number of constituent quark scaling, it will strengthen the case of a matter with partonic degrees of freedom. Due to the large mass difference between heavy quarks and light quarks, the

measurement of heavy quark v_2 will be also important for the quark coalescence model. The heavy quark v_2 measurement will enhance our understanding of relativistic heavy ion collisions.

Currently, the direct v_2 measurements of heavy flavor hadrons are not available yet at RHIC. The measurement of non-photonic electron v_2 is expected to reflect the heavy quark azimuthal anisotropy. Ref. [DES04] shows there is a strong correlation between the v_2 of D meson decayed electrons and the v_2 of D mesons.

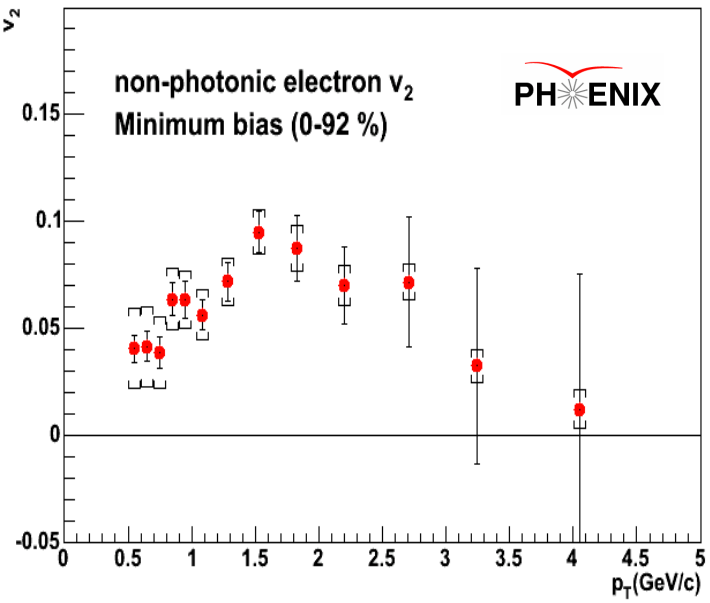

Figure 1.12: Non-photonic electron v_2 as a function of p_T in minimum bias Au+Au collisions at $\sqrt{s_{NN}}$ = 200 GeV from PHENIX [Ada06a]. The boxes (brackets) depict the statistical (point-by-point systematic) errors.

Fig. 1.12 shows the recent measurements of non-photonic electron v_2 in minimum bias Au+Au collisions at $\sqrt{s_{NN}}$ = 200 GeV from PHENIX [Ada06a]. Strong elliptic flow for non-photonic electrons is observed at low p_T region of $p_T < 2$ GeV/c, where non-photonic electrons are mainly from charm quark decays, suggesting a non-zero v_2 for the charm quark. The large v_2 together with the observed large suppression of non-

photonic electrons, provides strong evidence that heavy quarks are strongly coupled to the produced medium. At high p_T the v_2 tends to decrease with p_T. This could be an indication of increasing contribution to non-photonic electrons from B meson decays. The same D and B hadron v_2 can lead to very different non-photonic electron v_2 due to the different decay kinematics between D and B hadrons [Zha07]. The quantitative understanding of the non-photonic electron v_2 measurements requires the knowledge of the relative charm and bottom contributions to non-photonic electrons.

1.6 Thesis Outline

In this thesis, we present the first measurement of the B meson semi-leptonic decay contribution to non-photonic electrons at RHIC using non-photonic electron azimuthal correlations with charged hadrons in p+p collisions at $\sqrt{s_{NN}} = 200$ GeV from the STAR experiment. In chapter 2 the RHIC accelerator facility as well as the STAR detectors will be introduced. In chapter 3 we will present an innovative method which uses the azimuthal correlations between non-photonic electrons and charged hadrons to estimate the relative D and B contributions to non-photonic electrons. The detailed data analysis for inclusive electron identification, background electron reconstruction and the e-h azimuthal correlation signal extraction will be performed in chapter 4. Finally in chapter 5 we will present measurements of the B meson semi-leptonic decay contribution to non-photonic electrons as a function of p_T for $p_T > 2.5$ GeV/c, using comparisons of the experimental e-h correlation results with PYTHIA simulations. We will also discuss the comparison of our results to the FONLL pQCD calculation.

CHAPTER 2

Experimental Apparatus

The Relativistic Heavy Ion Collider (RHIC) at Brookhaven National Laboratory (BNL) has been used to explore some of nature's most basic – and most intriguing – ingredients and phenomena. In this chapter, we will discuss the RHIC machine complex, the STAR detector system and the major STAR sub-detectors used in this dissertation research.

2.1 RHIC Complex

The Relativistic Heavy Ion Collider (RHIC) at Brookhaven National Laboratory (BNL) commissioned in 1999, consists of two superconducting magnet colliding rings, each 3.8 km circumference. It is a world-class scientific research facility. It can collide nuclei ranging from protons to gold ions at top center-of-mass collision energies ranging from 500 GeV per nucleon-nucleon pair for p+p collisions to 200 GeV per nucleon-nucleon pair for Au+Au collisions. Asymmetric collisions such as deuteron on gold can also be handled by RHIC. The physics goal of this extraordinary new accelerator is to seek out the universe's tiniest features, particles smaller than nucleons in nuclei and to explore how these particles interact with each other.

Fig. 2.1 shows a schematic diagram of the RHIC complex [Sch06]. Table. 2.1 lists some of the design parameters of RHIC. The whole RHIC complex includes a Van de Graaff accelerator, a linear proton accelerator, the booster synchrotron, the Alternative Gradient Synchrotron (AGS) and the RHIC collider rings. Before the injection into the RHIC rings, the nuclei have to experience pre-accelerations. For gold beam operations, the gold ions with charge $Q = -1e$ are generated by the Pulsed Sputter Ion Source in

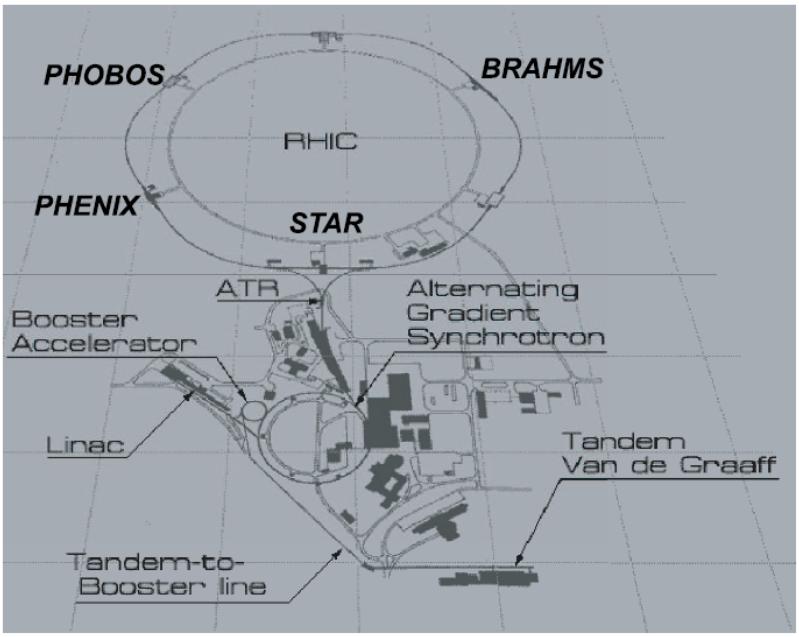

Figure 2.1: A schematic diagram of the RHIC complex.

the Tandem. They are initially accelerated through the Tandem Van de Graaff facility and a series of stripping foils. The ions leave the Tandem with an energy of ~ 1.0 MeV per nucleon and a net charge of $Q = +32e$. After the initial acceleration, the ions are then transferred to the Booster Synchrotron where they are accelerated to an energy of 95 MeV per nucleon and further stripped to a net charge of $Q = +77e$ before they are injected to the AGS. The AGS accepts the ions leaving from the Booster, accelerates them to an energy of 8.86 GeV per nucleon and removes the remaining two electrons. The fully stripped ions with $Q = +79$ are finally injected into the RHIC rings where they are accelerated to the collision energy. In proton beam operations, protons are injected from Linac to the Booster Synchrotron, followed by the acceleration in the AGS and the injection into RHIC rings.

The two concentric superconducting rings are denoted as blue ring and yellow ring. The rings have six interaction points where the two rings cross, allowing the particle

Table 2.1: The list of some RHIC design parameters.

Parameter	Value
Luminosity ($Au + Au$)	2×10^{26} cm^{-2}sec^{-1}
Luminosity ($p + p$)	4×10^{30} cm^{-2}sec^{-1}
Top beam energy (Au)	100 GeV/u
Top beam energy (proton)	250 GeV/u
# of bunches per ring	60
Revolution frequency	78 kHz
Ions per bunch (Au)	10^9
Ions per bunch (proton)	10^{11}
# of interaction points	6
Beam life time	~10 hours
Ring circumference	3833.845 m

Table 2.2: Experimental runs at RHIC from year 2000 to year 2006. Some short runs are not listed here.

Run (year)	Collision	Collision energy (GeV)	Luminosity delivered to STAR
Run-1 (2000)	Au+Au	130	3 (μb^{-1})
Run-2 (2001)	Au+Au	200	59 (μb^{-1})
Run-3 (2002/03)	d+Au	200	19.7 (nb^{-1})
Run-3 (2003)	p+p	200	2.5 (pb^{-1})
Run-4 (2003/04)	Au+Au	200	1270 (μb^{-1})
Run-4 (2004)	Au+Au	62.4	20.7 (μb^{-1})
Run-4 (2004)	p+p	200	3.2 (pb^{-1})
Run-5 (2004/05)	Cu+Cu	200	15.0 (nb^{-1})
Run-5 (2005)	p+p	200	12.7 (pb^{-1})
Run-6 (2006)	p+p	200	47.3 (pb^{-1})

beams to collide. Four interaction points are currently equipped with four experimental detector systems: STAR (6 o'clock), PHENIX (8 o'clock), PHOBOS (10 o'clock) and BRAHMS (2 o'clock).

RHIC has run in p+p, d+Au, Au+Au and Cu+Cu configurations since the first commissioning run in the summer of year 2000. Table. 2.2 shows the experimental runs at RHIC from year 2000 to year 2006. In this dissertation research, we focus on the analysis of p+p collisions recorded by the STAR detector in year 2005.

2.2 The STAR Detector

The Solenoidal Tracker at RHIC (STAR) is one of the four detector systems constructed at RHIC, specializing in tracking thousands of particles which can be produced by a

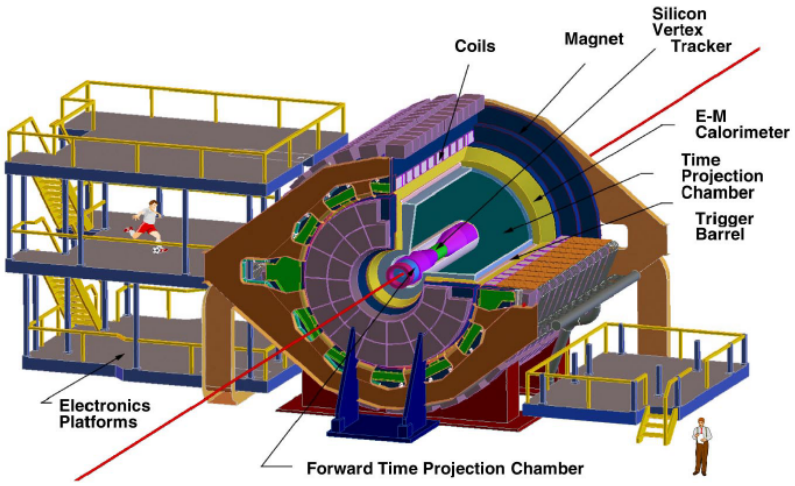

Figure 2.2: Layout of the STAR detector with cutaway showing the inner components.

single collision at RHIC. STAR is a detector of cylindrical geometry with a large acceptance designed to study a broad rang of physical observables. An emphasis was placed on mid-rapidity physics in order to study both the soft (non-perturbative) and hard (perturbative) aspects of the physics at RHIC. There are several sub-systems in the STAR detector system, nearly all of which cover the complete 2π in azimuth. Fig. 2.2 shows a perspective view of the STAR detector with a cutaway showing the inner components [Ack03]. The functions of the STAR subsystems are listed in Table. 2.3

The whole detector is placed in a uniform magnetic field with a maximum field strength of 0.5 Tesla. The magnetic field allows the tracking detectors to measure the bend of trajectories of charged particles, thus determining their momenta. The STAR magnet is adjustable and has been run in full field, reversed full field and half field configurations.

Table 2.3: The STAR subsystems and their functions.

Major STAR subsystem	Major function
Time Projection Chamber (TPC)	Tracking mid-rapidity charged particles and particle identification
Silicon Vertex Tracker (SVT)	Tracking interaction region charged particles
Forward Time Projection Chamber (FTPC)	Tracking forward region charged particles
Time of Flight (TOF)	Particle identification
Barrel Electro-Magnetic Calorimeter (BEMC)	Measuring mid-rapidity electrons, positrons and photons, and triggering high p_T events
Endcap Electro-Magnetic Calorimeter (EEMC)	Measuring large-rapidity electrons, positrons and protons
Zero-Degree Calorimeter (ZDC)	Measuring neutrons along the beam direction, used for event triggering
Central Trigger Barrel (CTB)	Measuring charged particles at mid-rapidity with a fast response for event trigger

The major sub-detectors of STAR used in this dissertation research are the Time Projection Chamber (TPC) [And03] and the Barrel Electro-Magnetic Calorimeter (BEMC) with the Shower Maximum Detector (SMD) [Bed03]. Details of these sub-detectors will be discussed in the following subsections.

2.2.1 Time Projection Chamber

Heavy ion collisions at RHIC can result in very high density tracking environment. For example, a central Au+Au collision may produce more than 1000 primary particles per unit of pseudo-rapidity. Therefore, RHIC is a very demanding environment in which to operate a detector. The central element of the STAR detector is a large volume, large acceptance Time Projection Chamber. Its acceptance covers ± 1.8 units of pseudo-rapidity through the full azimuthal range of 2π. It measures 4 m in diameter by 4.2 m long, making it the largest TPC in the world. The TPC records the tracks of particles, measuring their momenta, and identifies the particles by their ionization energy loss (dE/dx). Particles are identified over a momentum range from 100 MeV/c to greater than 1 GeV/c and momenta are measured over a range of 100 MeV/c to 30 GeV/c [And03].

Fig. 2.3 shows a schematic view of the STAR TPC, which sits in a homogeneous magnetic field up to half a Tesla along the z axis, provided by a solenoidal magnet outside the drift chamber. The major mechanical components of the TPC consist of the outer field cage (OFC), the inner field cage (IFC), the high voltage central membrane (CM), read out end caps and some other support devices. The CM, set at a voltage of -28 kV, separates the TPC into two longitudinal drift regions, each 2.1 m long. The concentric IFC and OFC cylinders (radius = 0.5 and 2.0 m, respectively) and the anode read out end caps, which are 2.1 m away from the CM, define two coaxial cylindrical drift volumes of 24.75 m^3. The CM, concentric field cage cylinders and the read out end caps define a uniform electric field of $\sim$ 135 V/cm between the CM and each end cap. Consequently the electric field and the magnetic field are parallel inside the TPC. Electric field uniformity is critical since track reconstruction precision is better than 1

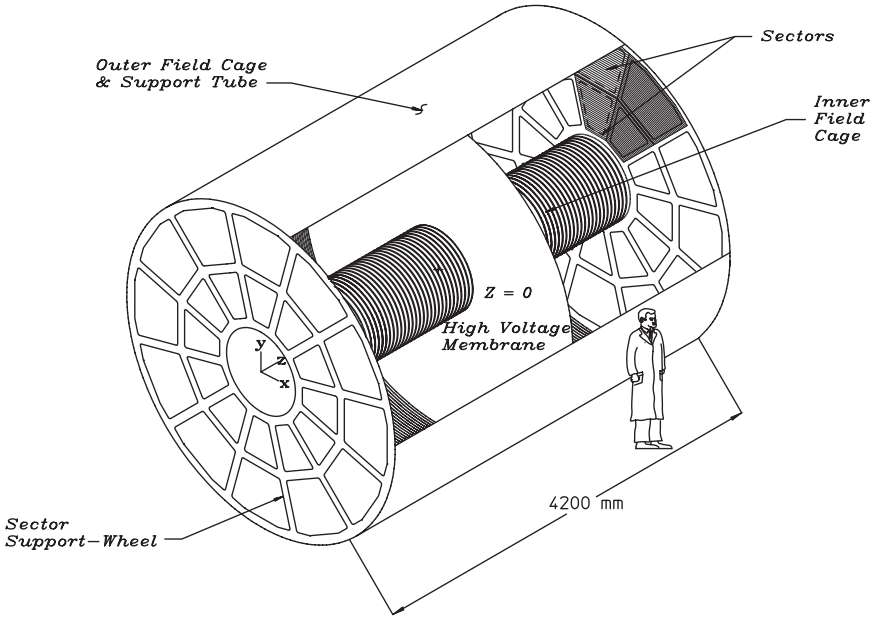

Figure 2.3: The schematic view of the TPC in STAR.

mm and electron drift paths are up to 2 meters.

The working gas of the TPC is P10 gas (10% methane, 90% argon). A charged particle traveling through the gas-filled TPC volume ionizes the gas along its trajectory. Due to the influence of the electric field between the CM and the end caps, the released secondary electrons from this ionization process drift to one anode end cap and positive ions drift in the opposite direction to the CM. Once the electrons drift to the end caps, they are detected by a Multi Wire Proportional Chamber (MWPC) with pad readout. The arrival time is recorded. Since the drift velocity of the electrons is known, the z coordinate of a point on the particle trajectory inside the TPC can be deduced from the time of drift for electrons from the point of origin to the anodes on the end cap and the known average electron drift velocity. The x and y coordinates are determined by the projection of the signal onto the pad plane mounted below the MWPC. There are a total of 136,608 pads in the pad readout.

The 3-D coordinate space points finding is the first step of the TPC track reconstruction process, resulting in a collection of points in global Cartesian coordinates. The tracking software performs two distinct tasks. First, algorithms associate space points to form tracks and second they fit the points on a track with a helix model to extract information such as the momentum of the particle. The resulted track collection from the TPC is combined with any other available tracking detector reconstruction results and then refit by application of a Kalman filter routine - a complete and robust statistical treatment [Don05]. This track collection consists of the global tracks. Using the helix parameters these global tracks are extrapolated to the closest approach to the beam collision line. The global average is the primary collision vertex position. The primary vertex resolution improves as the square root of the number of tracks used. A resolution of 350 μm is achieved with more than 1000 tracks [And03]. When the 3-D distance of closest approach (DCA) of a global track to the primary vertex is less than 3 cm, a refit of this track will be performed by forcing the track to originate from the primary vertex. The resulted collection from the refits consists of primary tracks.

The TPC performs as a 70 million pixel digital camera, allowing for the 3-D reconstruction of nearly all of the charged particles produced in each heavy ion collision at RHIC. Fig. 2.4 illustrates the reconstruction of a large number of charged particles in an event from Au+Au collisions at $\sqrt{s_{NN}} = 200$ GeV.

The ionization energy loss dE/dx for a particle traversing the TPC gas volume is a valuable tool allowing identification of particle species. The mean rate of dE/dx can be described by the Bethe-Bloch equation 2.1 [BR93],

$$-\frac{dE}{dx} = \frac{4\pi N e^4}{m_e c^2}\frac{1}{\beta^2} Z^2 (\ln \frac{2m_e c^2}{I}\beta^2\gamma^2 - \beta^2 - \frac{\delta(\beta)}{2}) \tag{2.1}$$

where N is the number density of electrons in the matter traversed, Z is the charge of the traveling particle, $m_e c^2$ is the rest energy of the electron, β is the velocity of the particle, $\gamma = \sqrt{1/(1-\beta^2)}$, I is the mean excitation energy of the atoms of the chamber gas and $\delta(\beta)$ is the relativistic medium polarization term. Different types of particles with the same momentum passing through the TPC gas lose a different amount

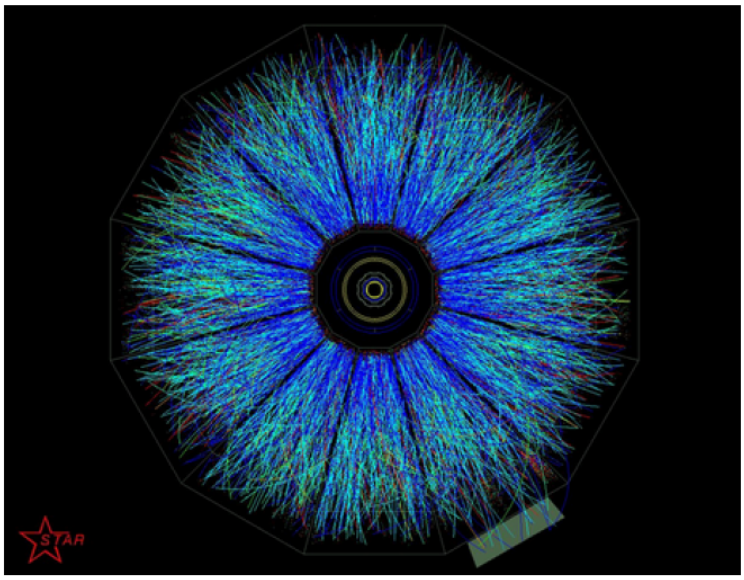

Figure 2.4: An event recorded by the STAR TPC from first Au+Au collisions at $\sqrt{s_{NN}}$ = 200 GeV. End view of the Time Projection Chamber from the beam direction.

of energy. Fig. 2.5 shows the energy loss for both primary and secondary particles in the STAR TPC as a function of the particle momentum. Different particles form different bands. The curves in Fig. 2.5 indicate the expected ionization energy loss for different particle species according to the Bethe-Bloch equation. The typical resolution of dE/dx in Au+Au collisions is $\sim 8\%$ [And03]. Kaons and pions can be separated by the TPC up to a momentum of about 0.7 GeV/c, and the protons can be separated from kaons and pions up to a momentum of about 1.1 GeV/c.

The STAR TPC has been running stably and reliably for several years. STAR has published many exciting physics results utilizing the TPC. In this dissertation, we will use the TPC as a major detector for electron identification and momentum measurement.

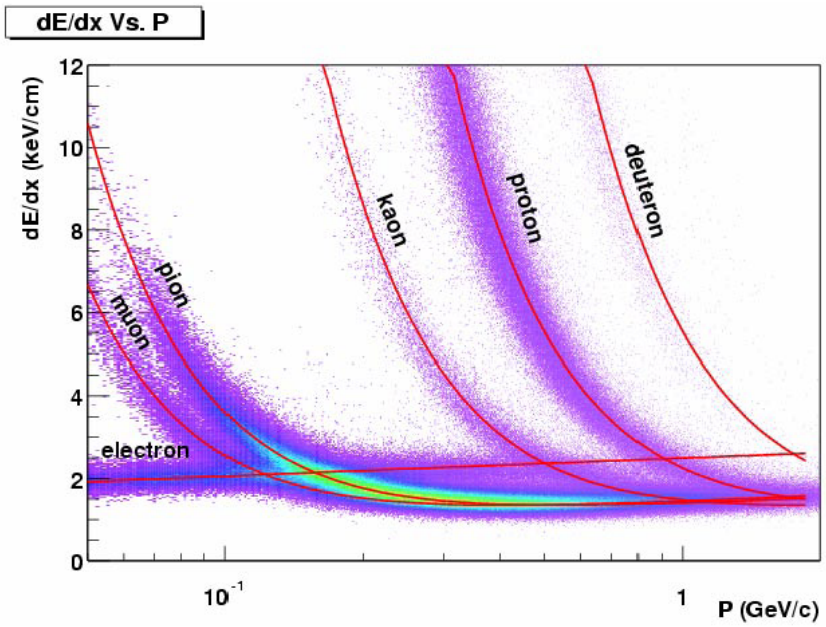

Figure 2.5: The dE/dx distribution for primary and secondary particles in the STAR TPC as a function of the momentum of primary particles. The magnetic field was 0.25 T.

2.2.2 Barrel Electro-Magnetic Calorimeter

The Barrel Electro-Magnetic Calorimeter (BEMC) allows STAR to trigger on and study rare, high p_T processes (jets, leading hadrons, direct photons, heavy quarks) and extends the capabilities of STAR to provide large acceptance for photons, electrons, π^0 and η mesons in systems spanning polarized p+p through Au+Au collisions [Bed03].

The BEMC is located inside the aluminum coil of the STAR solenoid within a cylindrical space approximately 41 cm deep, by 6.2 m in length. It is sandwiched between the TPC's gas chamber and the magnet coils. Fig. 2.6 shows a schematic drawing of

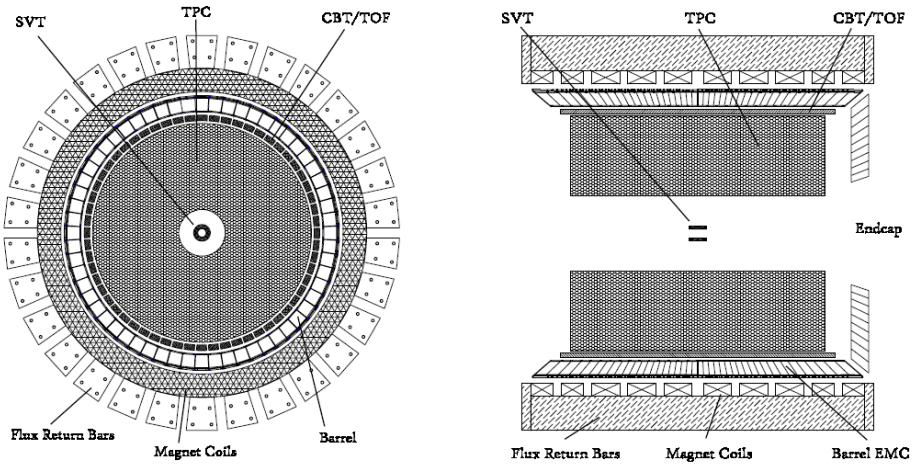

Figure 2.6: Cross sectional views of the STAR detector. The Barrel Electro-Magnetic Calorimeter is between the TPC and the magnet coils.

the STAR detector. The BEMC covers $|\eta| \leq 1.0$ and 2π in azimuth, thus matching the acceptance for full TPC tracking. The inner surface of the BEMC has a radius of about 220 cm and parallel to the beam axis.

The design for the BEMC includes a total of 120 calorimeter modules, each subtending 6^0 in $\Delta\phi$ and 1.0 unit in $\Delta\eta$. These modules are mounted 60 in ϕ and 2 in η. During Run-5 3/4 of the total barrel was instrumented to full azimuthal coverage and $-1 < \eta < 1$. The west half $(+Z)$ of the barrel was fully instrumented. Each module is roughly 26 cm in width by 293 cm long with an active depth of 23.5 cm. Each module is further segmented into 40 towers, 2 in ϕ and 20 in η, with each tower covering 0.05 in $\Delta\phi$ by 0.05 in $\Delta\eta$. The full BEMC is thus physically segmented into a total of 4800 towers. Each of these towers is projective and points back to the center of the interaction region. Fig. 2.7 shows the schematic view of a BEMC module illustrating the projective

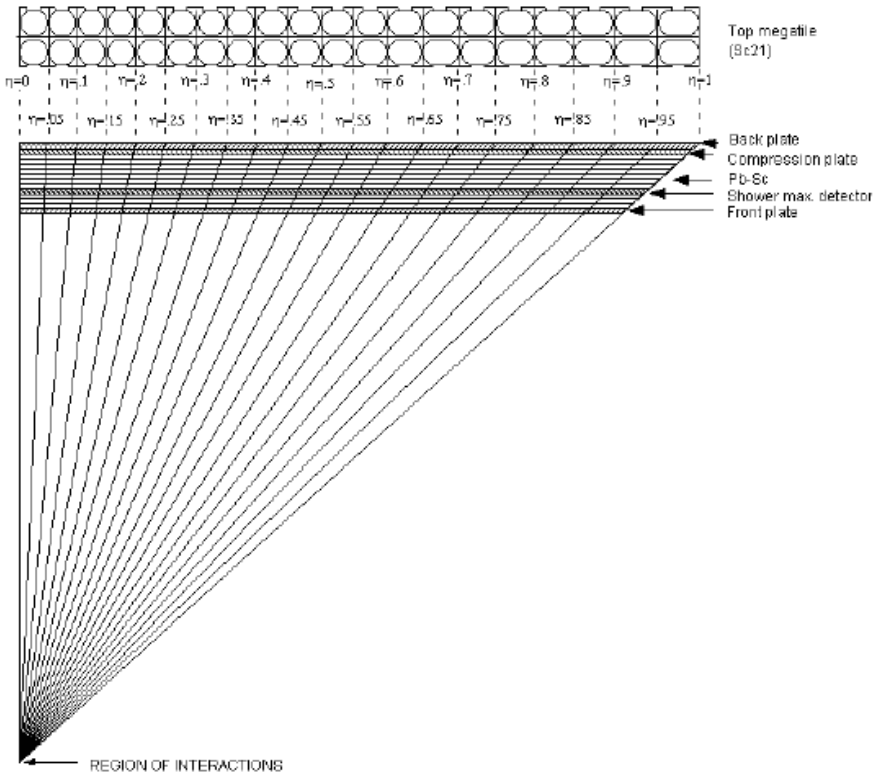

Figure 2.7: Side view of a BEMC module showing the projective nature of the towers. The towers are all pointing to the center point of the interaction region.

nature of the towers in the η-direction.

The BEMC is a sampling calorimeter using lead and plastic scintillator. This design is cost effective because of the large area and complex geometry of the BEMC. The core of each module consists of a lead-scintillator stack and a shower maximum detector (SMD) embedded approximately 5 radiation lengths below the inner surface of the BEMC. The details of SMD will be discussed in section 2.2.3. Fig. 2.8 shows an end view of a STAR BEMC module. There are 20 layers of 5 mm thick lead, 19 layers of 5 mm thick scintillator and 2 layers of 6 mm thick scintillator. The thicker scintillator layers are associated with the pre-shower detector. The electronics for the pre-shower

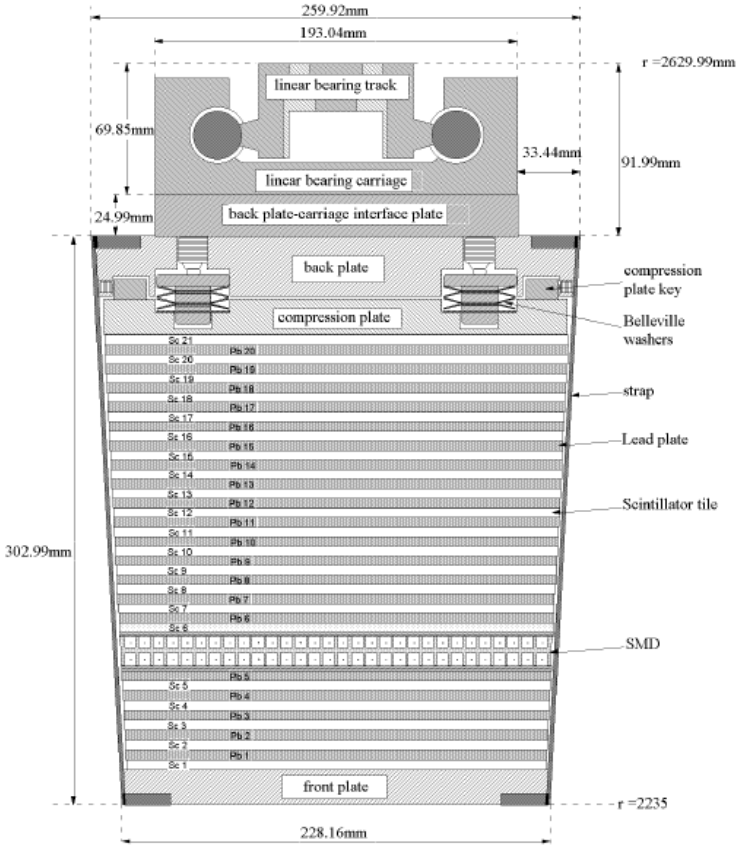

Figure 2.8: End view of a BEMC module showing the mounting system and the compression components.

detector was not installed until 2004. The pre-shower detector data were not used for this analysis.

2.2.3 Barrel Shower Maximum Detector

The Barrel Shower Maximum Detector (BSMD) is the partner detector of the BEMC. It is highly segmented and used to provide refined position resolution and measurement of the shower profile. Each of the 4800 towers of the BEMC spans $\Delta\phi \times \Delta\eta = 0.05 \times 0.05$ which at the radius of the inner face of the detector corresponds to a tower size $\sim 10 \times 10$ cm^2 at $\eta = 0$ increasing towards $\eta = 1$. While the BEMC towers provide precise energy

measurements for isolated electromagnetic showers, the high spatial resolution provided by the SMD is essential for π^0 reconstruction, direct photon identification and electron identification [Bed03].

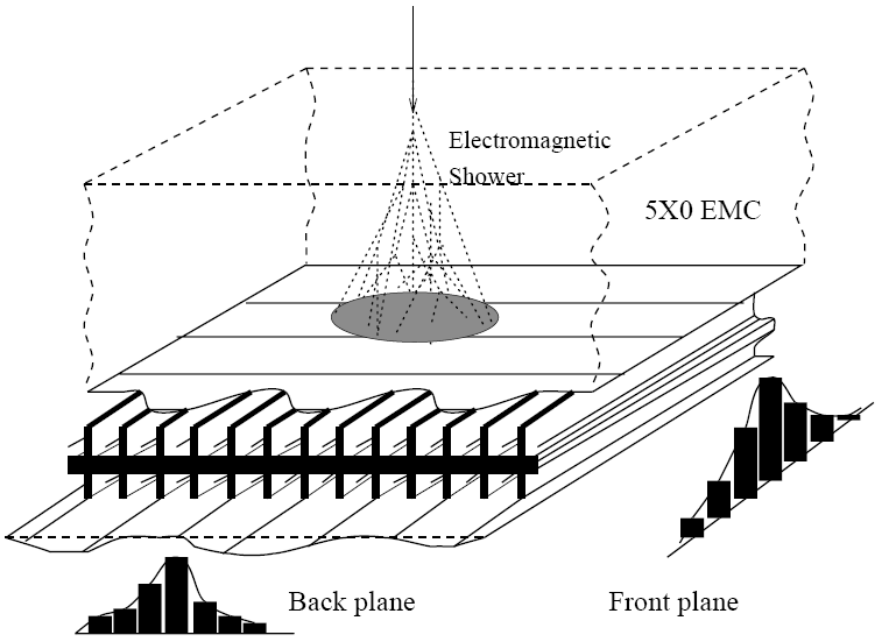

Figure 2.9: Schematic illustration of the double layer SMD.

The conceptual design of the SMD is shown in Fig. 2.9. The SMD is located at about 5 radiation length depth from the inner surface of the BEMC modules, where the SMD has an approximately linear response versus energy in the energy range from 0.5 to 5 GeV [Bed03]. The location of the SMD corresponds to the maximum shower development where a profile measurement can be made optimally with the selected shower maximum detector technology (gas proportional chamber with strip readout).

The unique feature of the STAR SMD is its double layer design. A two sided aluminum extrusion provides ground channels for two independent planes of proportional

wires. There are two independent PC Board cathode planes with strips etched in the η and ϕ directions, respectively, allowing reconstruction of a two dimensional image of the shower. The SMD is essentially a multi-wire proportional chamber - strip readout detector using gas amplification. Fig. 2.10 shows a cross sectional view of the SMD, and the design parameters and specifications are summarized in Table 2.4.

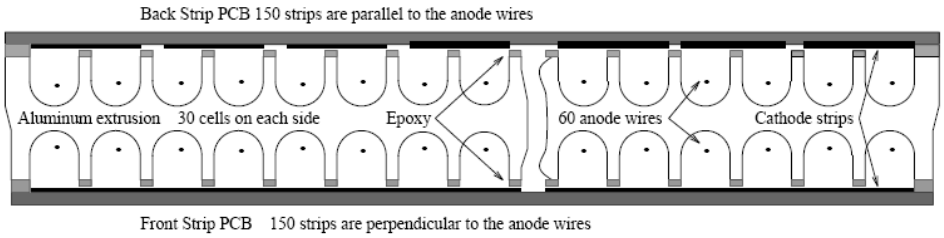

Figure 2.10: Cross sectional view of the SMD showing the extruded aluminum profile, the wires and cathode strips.

The detector strips sense the induced charge from the charge amplification near the wire. There are a total of 36000 strips in the full detector, 300 strips per BEMC module. One set of 150 strips is perpendicular to the wires, providing an image of the shower spatial distribution in the η direction. These are the η strips. Each of these η strips has size of about 0.1 radians in ϕ, i.e. the module width of about 23cm. The η strips have two groups, one narrower and one wider in width. The 75 strips in η for $|\eta| < 0.5$ have a width of about 1.54 cm; and the other 75 strips in η for $|\eta| > 0.5$ have a width of about 1.96 cm. The other set of 150 strips is parallel to the wire channels of the aluminum extrusion. These are the ϕ strips. These ϕ strips are physically 1.33 cm wide and have lengths of 0.1 units in η. 15 of these strips form a patch/sub-division. There are 10 patches in each module. Each of these patches spans $\Delta\phi \approx 0.1$ and $\Delta\eta = 0.1$.

Table 2.4: Design parameters and specifications for the STAR SMD.

Parameter	Value
Chamber Depth Inside EMC	$\sim 5X_0$ at $\eta = 0$
Rapidity Coverage (Single Module)	$\Delta\eta = 1.0$
Azimuthal Coverage (Single Module)	$\Delta\phi = 0.105$ R (6 degrees)
Occupancy (p+p)	$\approx 1\%$
Occupancy (Au+Au)	> 5 to $\approx 25\%$ (depends on threshold cut)
Chamber Depth (Cathode to Cathode)	20.6 mm
Anode Wire Diameter	50 μm
Gas Mixture	90% Ar/10% CO_2
Gas Amplification	≈ 3000
Signal Length	110 ns
Strip Width(Pitch) in η for $\|\eta\| < 0.5$	1.46 (1.54) cm
Strip Width(Pitch) in η for $\|\eta\| > 0.5$	1.88 (1.96) cm
Strip Width (Pitch) in ϕ	1.33 (1.49) cm
Number of Strips per Module	300
Total Number of Modules	120
Total Number of Readout Channels	36000

The double sided SMD design has some important features, including improved reliability, improved functionality in a high occupancy environments, improved hadron rejection and π^0/γ separation, and simplified mechanical construction. The later point is significant. The double sided extrusion design made it easy to satisfy the mechanical constraints for insertion within the EMC stack.

The STAR BEMC with its partner detector SMD can extend the capabilities of STAR to identify and measure electrons. We will use the BEMC with the SMD as another major detector in this dissertation research.

The BEMC is highly sensitive to electrons or photons, as they interact with the lead layers almost immediately upon entering the detector. An electromagnetic shower begins when a high-energy electron or photon enters the lead material. At high energy, photons interact with matter primarily via pair production - that is, they convert into an electron-positron pair, interacting with the lead atom or electron in order to conserve momentum. High-energy electrons and positrons primarily emit photons, a process called bremsstrahlung. These two processes continue in turn, until photons fall below the pair production threshold, and energy losses other than bremsstrahlung start to dominate for electrons: the number of shower particles then decays exponentially. The process is shown schematically in Fig. 2.11.

Charged hadrons are much less affected by the electromagnetic interaction with the lead atoms. Many charged hadrons will be produced in every collision at RHIC. When striking the BEMC, a significant fraction, $\sim 20-30\%$ of high energy charged hadrons do not deposit a significant amount of energy via nuclear interactions, instead depositing $\sim 250-350$ MeV of equivalent energy in the calorimeter due largely to electromagnetic ionization (the dE/dx energy loss described by the Bethe-Bloch equation 2.1). These hadrons are so-called "Minimum Ionizing Particles" (MIP) producing "MIP hits" in the EMC towers. The energy deposition of non-showering, high p_T hadrons is approximately constant and provide a convenient calibration reference [CPR02].

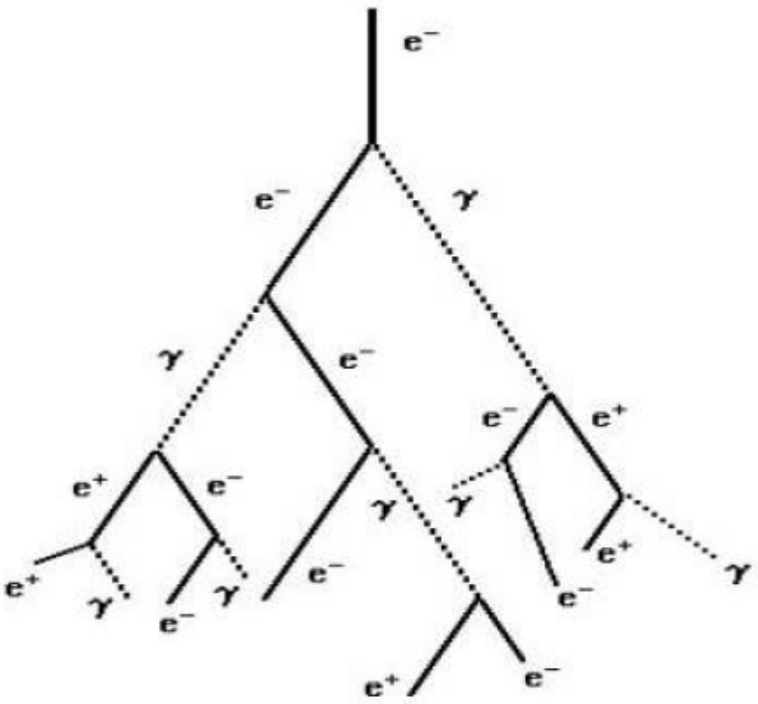

Figure 2.11: Schematic diagram of an electron initiated electromagnetic shower.

CHAPTER 3

PYTHIA Monte-Carlo Studies

We compare the D meson and non-photonic electron p_T distributions measured from the STAR experiment at RHIC with the PYTHIA Monte Carlo event generator in p+p collisions at $\sqrt{s_{NN}} = 200$ GeV. A delta fragmentation function much harder than the Peterson function, consistent with the recombination scheme for charm meson formation, is needed to simultaneously describe the STAR measurements of the D meson p_T shape and of the single non-photonic electron p_T distribution. Correlations of non-photonic electrons with charged hadrons are studied. We propose experimental methods to quantitatively determine the relative contributions of D and B meson semi-leptonic decays to the non-photonic electrons.

3.1 D Meson and Non-Photonic Electron Spectra

The heavy quark production in p+p and p+A collisions provides a reference for heavy meson formation in nucleus-nucleus collisions and for nuclear modification factors of heavy quarks in the nuclear medium. The Peterson function [PSS83]

$$D(z \equiv p_D/p_c) \propto \frac{1}{z[1 - 1/z - \varepsilon/(1-z)]^2} \tag{3.1}$$

has often been used to describe the charm fragmentation function, where the parameter $\epsilon \approx 0.05$ (default in PYTHIA [SLM01]) is in reasonable agreement with the results from fits to charm production in e^+e^- and γp collisions [NO00, Gla03]. However, in charm hadroproduction, it was observed that the c-quark p_T distributions of next-to-leading-order (NLO) pQCD calculations agree well with the measured open charm p_T spectrum [Ada97, Alv96], indicating that a much harder fragmentation function peaked

near $z \approx 1$ in Eq. 3.1 is needed in charm hadroproduction. A more detailed discussion of this observation can be found in Ref. [VBH92, FMN98]. In low energy nuclear collisions an intrinsic k_T distribution was introduced to the initial parton transverse momentum distribution to boost the p_T of heavy quarks produced [FMN98]. However, it is found that at RHIC energy previous k_T parameters were insufficient to enhance the heavy quark p_T to match the RHIC measurement [Vog03]. Coalesence [LK02, LM03] or recombination [FMN03, HY03a, GKL03] models have also been proposed for charmed meson formation by combining a charm quark with a light up or down quark, presumably of soft p_T [RS03]. Thus the charmed hadron p_T would coincide with the bare charm quark p_T distribution in this hadronization scheme. These various hadron formation schemes can lead to significantly different charmed meson p_T distributions when interpreting non-photonic electron p_T spectra from experimental measurements.

3.1.1 D Meson Transverse Momentum Distributions

We evaluate the p_T distributions of the charm quark and D mesons from PYTHIA v6.22 [SLM01] and compare the PYTHIA results with the STAR measurements [Ada05b, Tai04]. The charm quark fragmentation function will be modified from the default Peterson function and the other PYTHIA parameters are tuned in order to describe the experimental D meson data as well as the STAR non-photonic electron spectra [Abe06b].

Fig. 3.1 shows charm quark spectra from PYTHIA calculations and NLO pQCD predictions for charm quark spectra [Vog03] together with the STAR D meson spectrum, where the measured D meson data points from d+Au collisions at $\sqrt{s_{NN}} = 200$ GeV have been scaled by $N_{bin} = 7.5$ – the number of binary collisions. The PYTHIA spectra have been scaled to the measured dN/dy of 0.028 ± 0.004 ($stat.$) ± 0.008 ($syst.$) [Ada05b] for D^0 at mid-rapidity. The scaling factors are listed in Table 3.1. The theoretical curve with the MRST HO PDF has been normalized to the measured total $c\bar{c}$ cross section ($1.3 \pm 0.2 \pm 0.4$ mb) [Ada05b] by a factor of 3.4.

The stars in Fig. 3.1 depict the charm quark p_T distribution from a PYTHIA calculation with the following parameters (set I) from reference [Adc02]: PARP(67) = 1 (factor

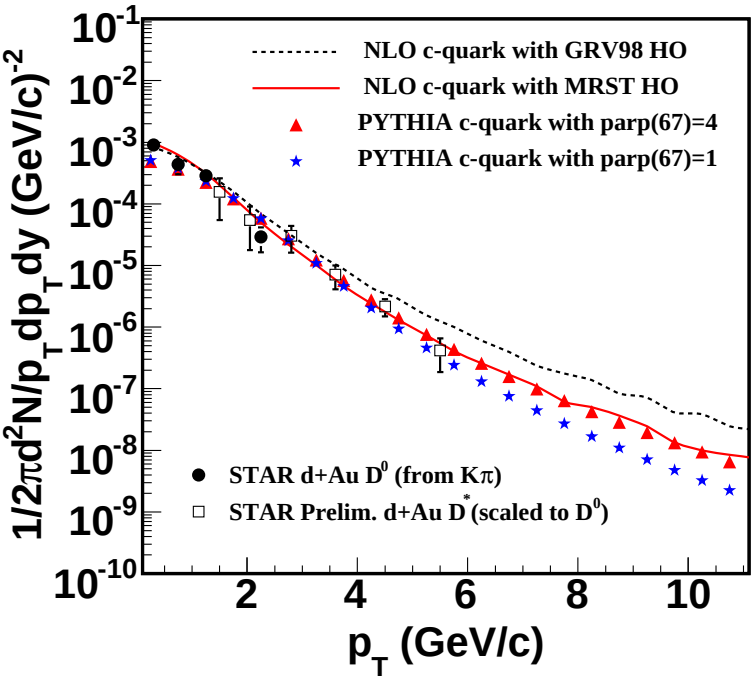

Figure 3.1: Charm quark p_T distributions from PYTHIA calculations compared with next-to-leading-order pQCD predictions for charm quark spectra and the STAR measured D meson data from d+Au collisions scaled by $N_{bin} = 7.5$.

multiplied to Q^2) , $< k_t >= 1.5$ GeV/c, $m_c = 1.25$ GeV/c^2, $K_{factor} = 3.5$, MSTP(33) = 1 (inclusion of K factors), MSTP(32) = 4 (Q^2 scale) and CTEQ5L PDF. We further tuned the value of PARP(67) to 4, which enhances the c-quark production probability through gluon splitting and is introduced to take into account higher order effects in the pQCD calculation [NS00]. The results are shown as triangles in Fig. 3.1. We found that this change mainly affects c-quark production at high p_T and can effectively reproduce the NLO pQCD calculation. We will refer to this set of parameters as parameter set II in the rest of this thesis. The total cross section changes very slightly from parameter set I to parameter set II because it mainly affects the high p_T region. Thus the normalization factors for the PYTHIA spectra also change slightly between these two sets of parameters as shown in Table 3.1.

Table 3.1: The scaling factors used to normalize the PYTHIA charm quark and D^0 spectra to the measured dN/dy of 0.028 ± 0.004 ($stat.$) ± 0.008 ($syst.$) for D^0 at mid-rapidity.

Spectrum	Scaling factor
c-quark with parp(67) = 4	1.01
c-quark with parp(67) = 1	1.03
D^0 with parp(67) = 4, $\varepsilon = 10^{-5}$	1.60
D^0 with parp(67) = 1, $\varepsilon = 10^{-5}$	1.62
D^0 with parp(67) = 4, $\varepsilon = 0.05$	1.72
D^0 with parp(67) = 1, $\varepsilon = 0.05$	1.75

We compared the charm quark spectra from PYTHIA calculations to the STAR published D^0 spectrum [Ada05b] together with the STAR preliminary D^* spectrum [Tai04]. The combination of STAR measured D^* and D^0 meson spectra into a single D meson spectrum is hampered by the large uncertainties in the ratio $D^*/D^0 = 0.4 \pm 0.09 \pm 0.13$ [Tai04] which is experimentally not well known at RHIC. The STAR D meson spectrum covers a limited p_T range and is not well constrained at high p_T. Without further tuning other PYTHIA parameters, we find that the generated bare charm quark spectra from PYTHIA calculations using parameter set I and parameter set II approximately match the STAR D meson p_T distribution. As demonstrated in Fig. 3.1, the PYTHIA calculation with parameter set II also yields a charm quark p_T distribution similar to the NLO pQCD calculations [Vog03, CNV05], which coincides with the STAR D meson p_T spectrum as well. These comparisons do not imply that the PYTHIA calculations with these two parameter sets and NLO pQCD calculations are equivalent in physics contents.

The D^0 p_T distributions from PYTHIA calculations are shown in Fig. 3.2, where the PYTHIA spectra have been scaled to the measured dN/dy for D^0 at mid-rapidity.

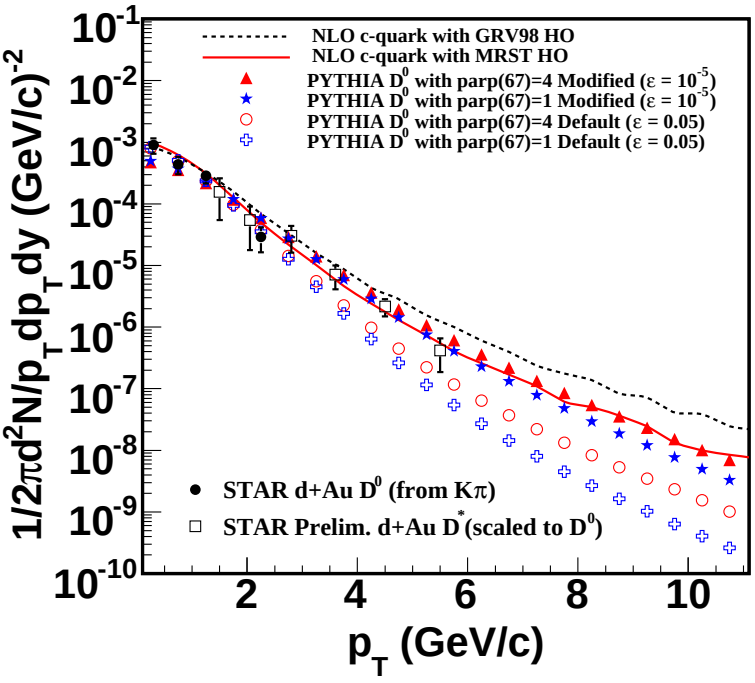

Figure 3.2: D^0 p_T distributions from PYTHIA calculations compared with next-to-leading-order pQCD predictions for charm quark spectra and the STAR measured D meson data from d+Au collisions scaled by $N_{bin} = 7.5$.

The scaling factors are listed in Table 3.1. The D^0 spectra from PYTHIA calculations using the default Peterson fragmentation function is shown as open circles for parameter set II and crosses for parameter set I. The default Peterson function refers to the value of the parameter ε in Peterson function being 0.05 for charm quarks and 0.005 for bottom quarks. The default Peterson fragmentation for charm quarks is too soft to reproduce the measured D^0 spectrum together with D^* spectrum. We modified the value of the parameter ε to 10^{-5} for both charm and bottom quarks. In this case the fragmentation function is nearly $\delta(1-z)$. The results are shown as stars for parameter set I and triangles for parameter set II in Fig. 3.2. The PYTHIA calculations using the modified Peterson fragmentation function ($\varepsilon = 10^{-5}$) with parameter set I and set II can reasonably reproduce the measured D meson p_T distribution.

While the k_T broadening can make the charm p_T distribution harder at low beam energies [FMN98], the intrinsic k_T has little effect on the p_T distribution at RHIC energies [Vog03]. A harder fragmentation function is needed for the hadronization of charm quarks if the pQCD calculation is to describe the measured STAR data. Recent FONLL calculations yielded a harder p_T distribution for heavy flavored mesons and the effective fragmentation in these calculations seem to be harder though the scheme in FONLL is different from the fragmentation function in the PYTHIA model.

3.1.2 Non-Photonic Electron Transverse Momentum Distributions

The STAR independent measurements of the reconstructed D^0 meson and of the single electrons from heavy quark semi-leptonic decays measured with TOF and TPC are consistent [Ada05b]. The electron measurement there only covers up to $p_T < 4$ GeV/c and has no sensitivity to the B meson contribution. We also checked the consistency between D meson data and non-photonic single electron data in p+p collisions within our PYTHIA calculations.

Fig. 3.3 shows the electron spectra from PYTHIA calculations using the modified Peterson fragmentation function for charm quarks and bottom quarks with parameter set II in the left panel and parameter set I in the right panel. Fig. 3.4 shows the electron spectra from PYTHIA calculations using the default Peterson fragmentation function for charm quarks and bottom quarks with parameter set II in the left panel and parameter set I in the right panel. The parameters for bottom quarks in set II and set I are all the same as for charm quarks except $m_b = 4.8$ GeV/c^2. The PYTHIA spectra of electrons from charm meson decays (blue open triangles) are scaled by the same factor used to scale the PYTHIA D^0 spectra to the measured dN/dy for D^0 at mid-rapidity. The electron spectra from B meson decays (green bands) are normalized by the ratio of $\sigma_{b\bar{b}}/\sigma_{c\bar{c}}$ based on the NLO pQCD calculation [Vog02]. The band corresponds to the theoretical uncertainty of this ratio (0.45% - 0.60%) [Vog02]. We used the value at the center of this range (0.525%) to calculate the sum of the electrons (red solid lines).

Fig. 3.3 and Fig. 3.4 also show the comparison to the measured non-photonic single

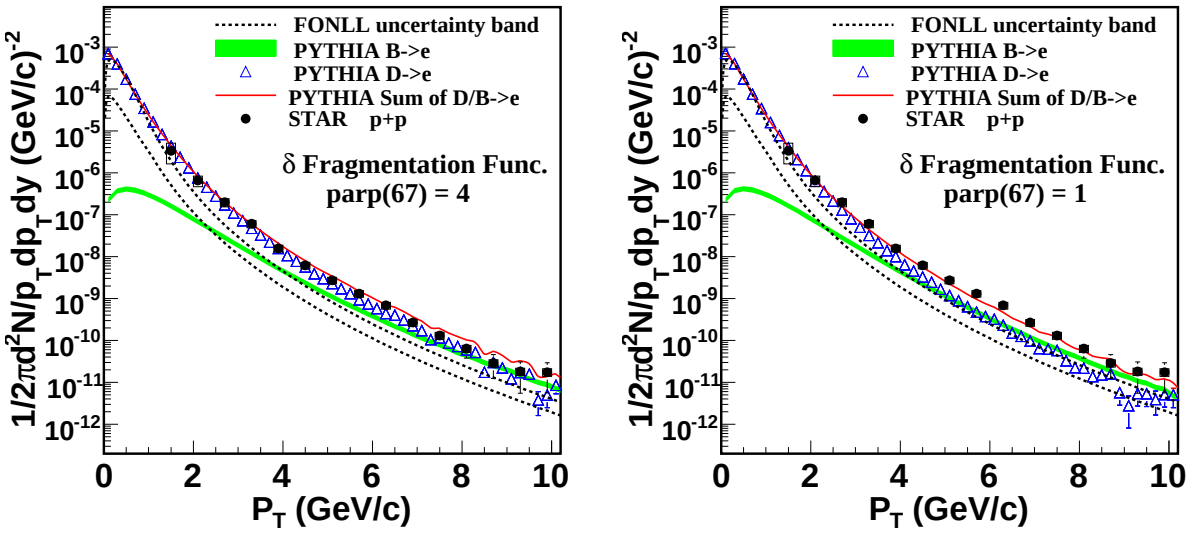

Figure 3.3: Electron spectra from PYTHIA calculations with the δ fragmentation function for charm and bottom quarks compared with background subtracted single electron spectrum measured by STAR from p+p collisions and the prediction for theoretical uncertainty electron band. The $\sigma_{b\bar{b}}/\sigma_{c\bar{c}}$ ratio from NLO pQCD calculation is used to scale the PYTHIA spectra. Left panel: The PYTHIA spectra are from parameter set II. Right panel: The PYTHIA spectra are from parameter set I.

electron data in p+p collisions from the STAR (black dots) [Abe06b] experiment and the FONLL calculation for the theoretical uncertainty band of the electron spectrum from charm and bottom in p+p collisions (dashed lines) [CNV05].

The electron spectra from PYTHIA calculations using the default Peterson fragmentation function are softer than the STAR measured electron data as shown in Fig. 3.4. The spectra from the default Peterson fragmentation function are compatible with the upper limit of the FONLL calculation. The FONLL prediction of electron spectrum gives a fair description of the shape of the STAR measured spectra. But there is a discrepancy in the overall scale and the FNOLL calculation is significant below the STAR data at high p_T. More discussions on the theoretical uncertainties of the FONLL calculation and the discrepancy between FONLL calculations and the STAR measurement

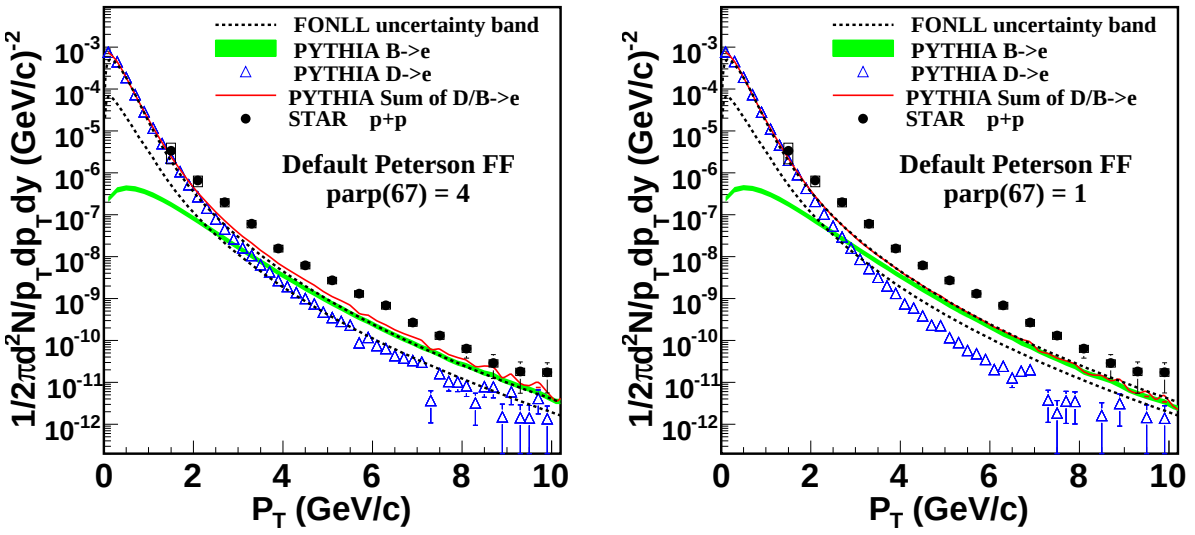

Figure 3.4: Electron spectra from PYTHIA calculations with the default Peterson function in PYTHIA for charm and bottom quarks compared with background subtracted single electron spectrum measured by STAR from p+p collisions and the prediction for theoretical uncertainty electron band. The $\sigma_{b\bar{b}}/\sigma_{c\bar{c}}$ ratio from NLO pQCD calculation is used to scale the PYTHIA spectra. Left panel: The PYTHIA spectra are from parameter set II. Right panel: The PYTHIA spectra are from parameter set I.

can be found in Section 1.5.1.

The measurement of electron p_T distribution alone has a reduced sensitivity to the p_T distribution of D mesons as shown in reference [BKG03]. As shown in Fig. 3.3, within the statistical and systematic errors of the STAR electron data, the PYTHIA calculations, using the δ fragmentation function for both charm and bottom quarks, with both parameter set II and parameter set I can yield electron p_T distributions similar to the STAR non-photonic electron measurement. The STAR direct D meson measurement and non-photonic electron measurement are consistent within our PYTHIA calculations. A δ fragmentation function is needed to simultaneously describe the STAR measurements of the D meson p_T shape and of the single non-photonic electron p_T distribution. This δ fragmentation function scheme indicates that the contribution of electrons from

B decays is not dominant for the measured p_T region up to 6 - 8 GeV/c if the $\sigma_{b\bar{b}}/\sigma_{c\bar{c}}$ ratio is $\sim 0.45\% - 0.60\%$ based on NLO pQCD calculation.

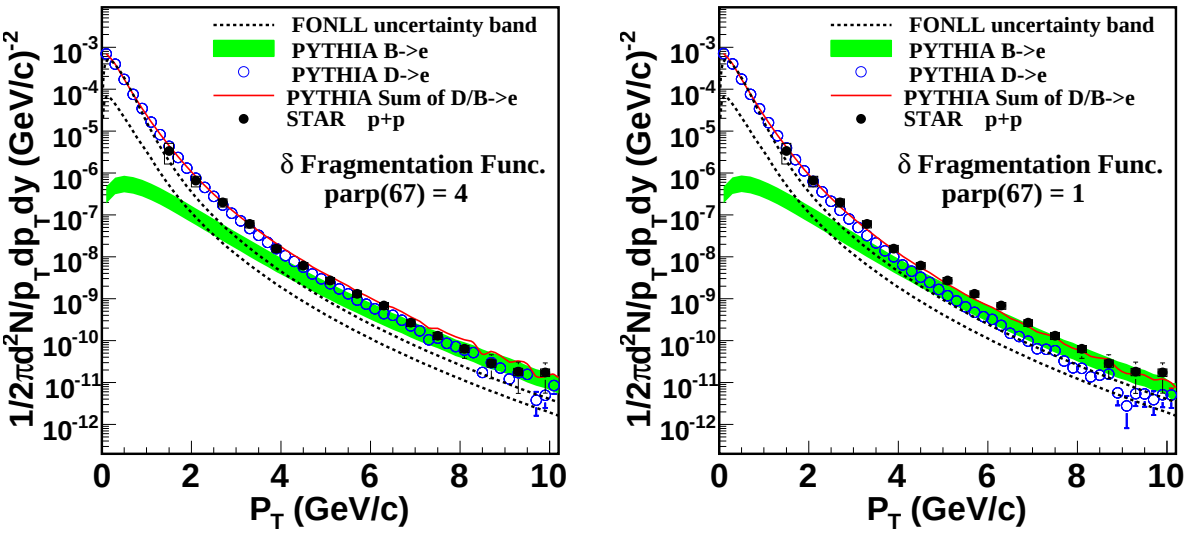

Figure 3.5: Electron spectra from PYTHIA calculations with the δ fragmentation function for charm and bottom quarks compared with background subtracted single electron spectrum measured by STAR from p+p collisions and the prediction for theoretical uncertainty electron band. The $\sigma_{b\bar{b}}/\sigma_{c\bar{c}}$ ratio from FONLL calculation is used to scale the PYTHIA spectra. Left panel: The PYTHIA spectra are from parameter set II. Right panel: The PYTHIA spectra are from parameter set I.

The recent FONLL calculation [CNV05] gives a total $c\bar{c}$ cross section in p+p collisions of $\sigma_{c\bar{c}}^{FONLL} = 256^{+400}_{-146}$ μb, and the total cross section for bottom production is $\sigma_{b\bar{b}}^{FONLL} = 1.87^{+0.99}_{-0.67}$ μb. The theoretical uncertainty of $\sigma_{b\bar{b}}/\sigma_{c\bar{c}}$ ratio we used here (0.45% - 0.60%) based on the NLO pQCD calculation [Vog02] may be an underestimate according to this recent FONLL calculation. We then extend the uncertainty of $\sigma_{b\bar{b}}/\sigma_{c\bar{c}}$ ratio according to the FONLL calculation. We use the values of $\sigma_{b\bar{b}}^{FONLL}(upper)/\sigma_{c\bar{c}}^{FONLL}(upper)$ and $\sigma_{b\bar{b}}^{FONLL}(lower)/\sigma_{c\bar{c}}^{FONLL}(lower)$ to determine the uncertainty range of $\sigma_{b\bar{b}}/\sigma_{c\bar{c}}$ ratio and it is $\sim 0.436\% - 1.09\%$. The center value is determined by $\sigma_{b\bar{b}}^{FONLL}(center)/\sigma_{c\bar{c}}^{FONLL}(center)$ $\sim 0.53\%$ and is used to calculate the sum of the electron spectra. The results are shown

in Fig. 3.5. The B decay contribution to non-photonic electrons starts to become dominant at p_T around 4 GeV/c if the $\sigma_{b\bar{b}}/\sigma_{c\bar{c}}$ ratio approaching the higher end of the theoretical uncertainty region of $\sim 0.436\% - 1.09\%$ from the FONLL calculation.

3.2 Experimental Methods to Estimate Relative Contributions to Non-Photonic Electrons from Charm and Bottom Decays

It is critical that the B and D meson semi-leptonic decay contributions to non-photonic electrons to be separated experimentally. We propose experimental methods to estimate relative contributions from charm and bottom decays.

3.2.1 Azimuthal Correlations Between Non-Photonic Electrons and Charged Hadrons

We have studied the azimuthal correlations between heavy quark semi-leptonic decay electrons and inclusive charged hadrons. Since in the experimental data we cannot differentiate heavy quark decay hadrons from others, we used inclusive hadrons in our correlation study. Fig. 3.6 shows the $\Delta\varphi$ distributions between non-photonic electrons and inclusive charged hadrons of $p_T > 0.3$ GeV/c for various electron trigger p_T ranges. The distributions are scaled by the number of electron triggers. These plots are from PYTHIA calculations with parameter set II and the modified heavy quark fragmentation function. The solid lines in Fig. 3.6 are for electrons from B meson decays and the dashed lines are for electrons from D decays. As demonstrated in Fig. 3.6, there is a significant difference between B and D meson decays in the near-side correlations. The width of near-side peak for electrons from D decays is much narrower than those for the B decays. The wide width from B meson decays is due to the larger energy release (Q value) in the B meson semi-leptonic decays leading to a broad angular correlation between daughter hadrons and electrons. Fig. 3.7 shows the distributions of electron p_T versus its parent p_T. For an electron at high p_T from B meson decays, the B meson

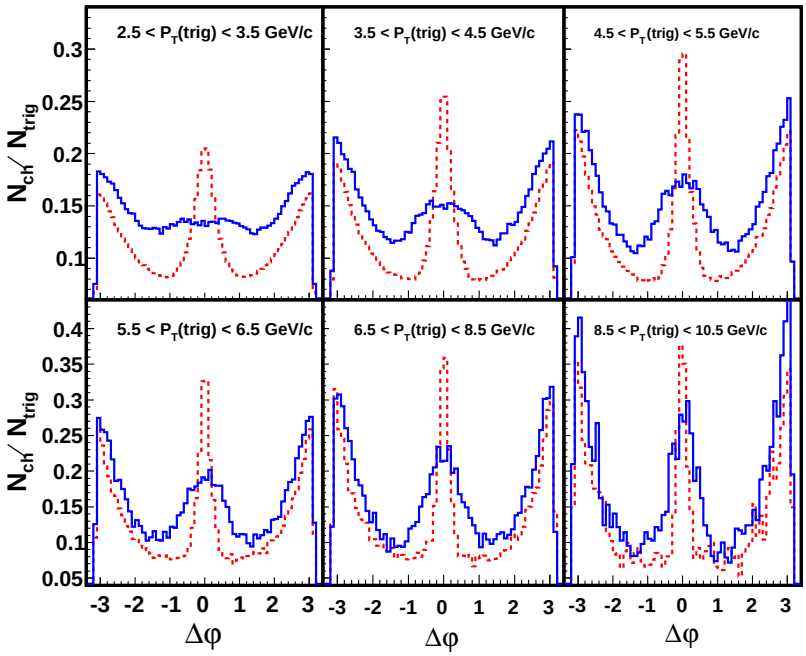

Figure 3.6: $\Delta\varphi$ distributions between non-photonic electrons and charged hadrons with six electron trigger p_T cuts and associated hadron $p_T > 0.3$ GeV/c. Solid lines show electrons from B meson decays. Dashed lines show electrons from D meson decays.

does not have to be at high transverse momentum because the electron can get large momentum from the b-quark mass. In the case of D meson decays, the D meson needs to have a large momentum in order to boost the daughter electron to a high p_T. The lowest electron trigger p_T, $2.5-3.5$ GeV/c, is larger than the D meson mass, making the near-side correlation sharper. However, the electron trigger p_T doesn't become larger than the B meson mass until $5.5 < p_T(trig) < 6.5$ Gev/c. Therefore, the motion of the B meson is less relativistic than that of the D meson. There is no sharp peak at the near-side correlation emerging until the electron trigger p_T is approaching twice the B meson mass.

We found the difference in the near-side correlations between D decays and B decays is largely due to the decay kinematics, not the production dynamics. We trace back three steps to find the hadrons from D meson decays and study the non-photonic electrons

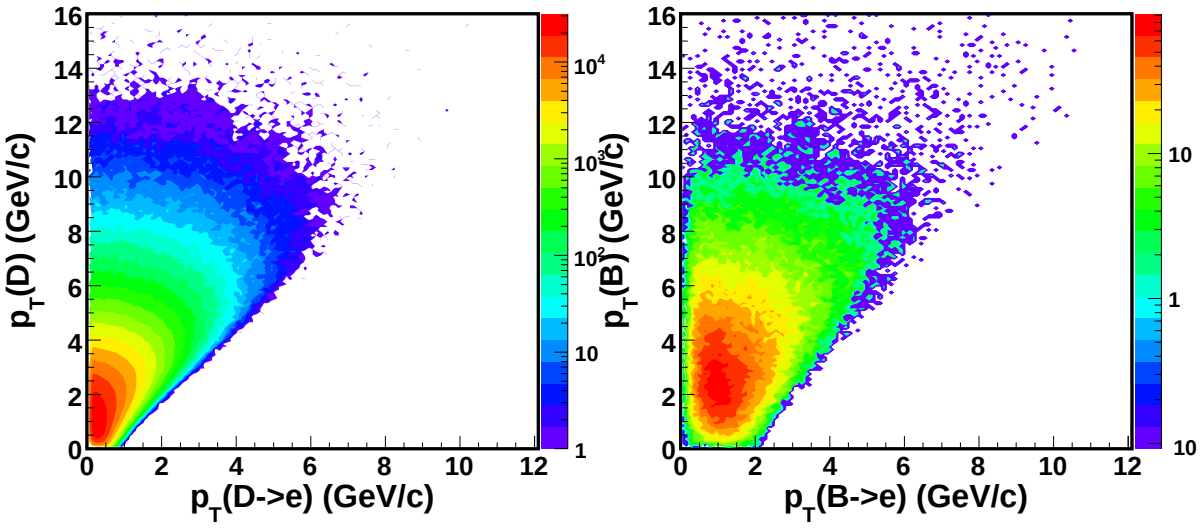

Figure 3.7: The distributions of electron p_T versus its parent p_T. Left: Electrons from D decays. Right: Electrons from B decays.

azimuthal correlations with those hadrons from D meson decays. Fig. 3.8 gives the distributions with two electron trigger p_T ranges as an example. The left panels are the correlations between non-photonic electrons and inclusive charged hadrons. The middle panels are the correlations between non-photonic electrons and the hadrons from D meson decays. The right panels are the subtractions. We can see the contribution to the near-side correlation is mostly due to the hadrons from D meson decays. This plot is from PYTHIA calculations with the δ fragmentation function and parameter set II.

The comparison of $\Delta\varphi$ distributions between PYTHIA calculations with the default Peterson fragmentation function and the δ fragmentation function is shown in Fig. 3.9 for D decays and in Fig. 3.10 for B decays. Variations on the fragmentation function from the default Peterson function to the δ fragmentation function do not change the correlation shapes in a significant way. The comparison of $\Delta\varphi$ distributions between PYTHIA calculations with parameter set II and parameter set I is shown in Fig. 3.11 for D decays and in Fig. 3.12 for B decays. We can see the correlation shapes are very similar between parameter set II and parameter set I.

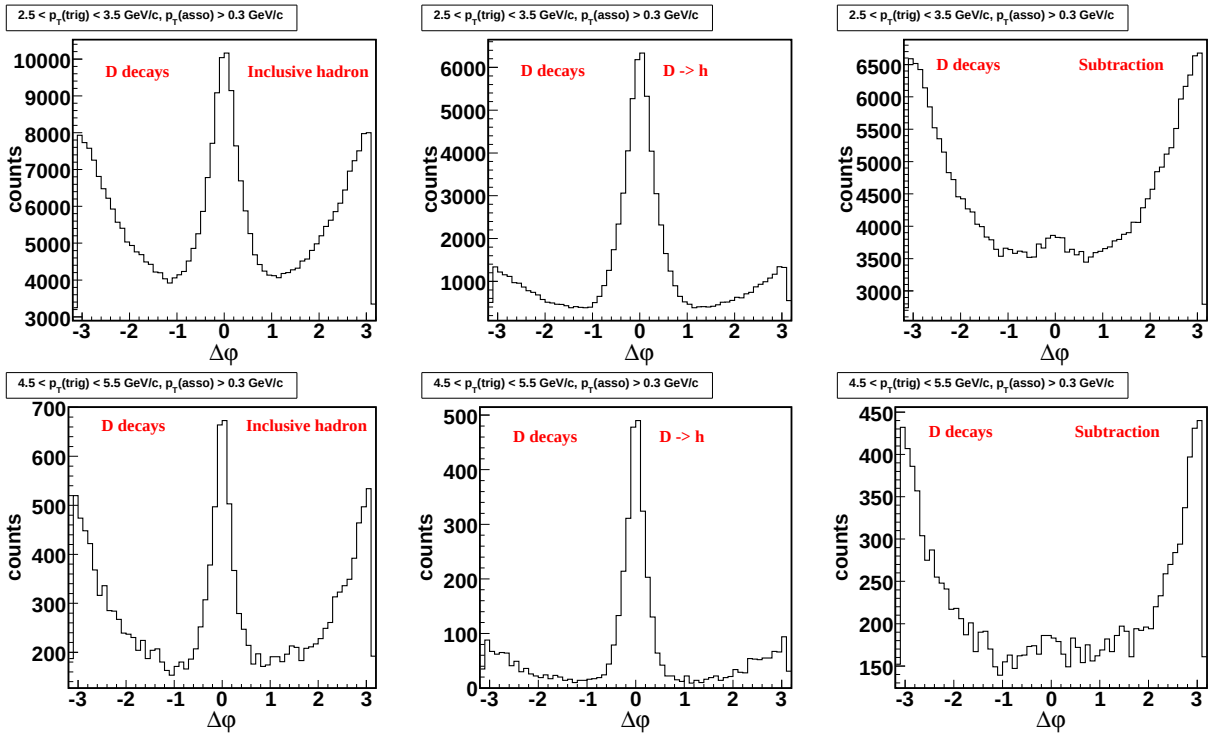

Figure 3.8: Left: Azimuthal correlations between non-photonic electrons and inclusive charged hadrons. Middle: Azimuthal correlations between non-photonic electrons and the hadrons from D meson decays. Right: The subtraction of left panel and the middle panel. This plot is from PYTHIA calculations with the δ fragmentation function and parameter set II.

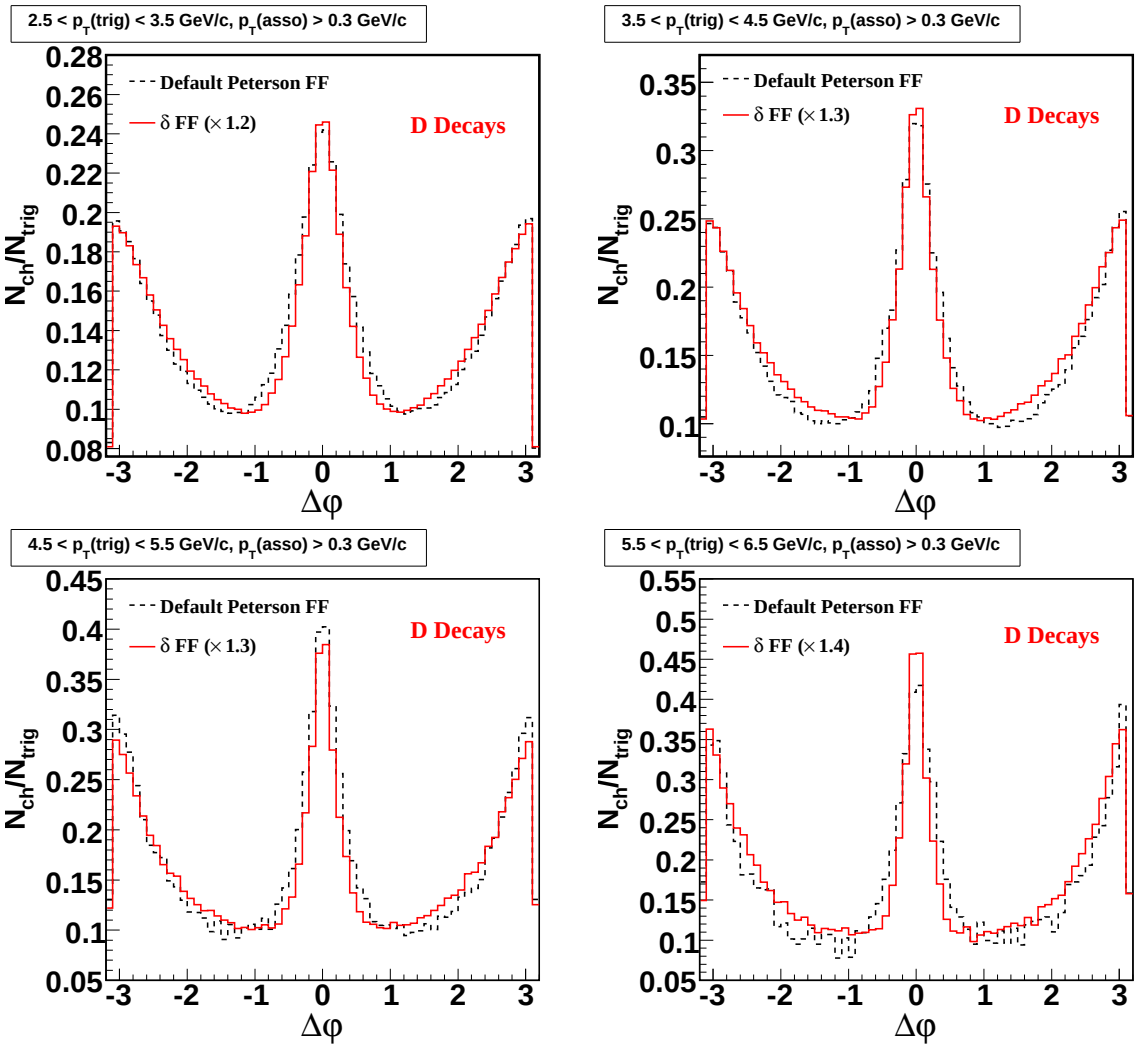

Figure 3.9: Comparison of $\Delta\varphi$ distributions for D decays between PYTHIA calculations with the default Peterson fragmentation function and the δ fragmentation function.

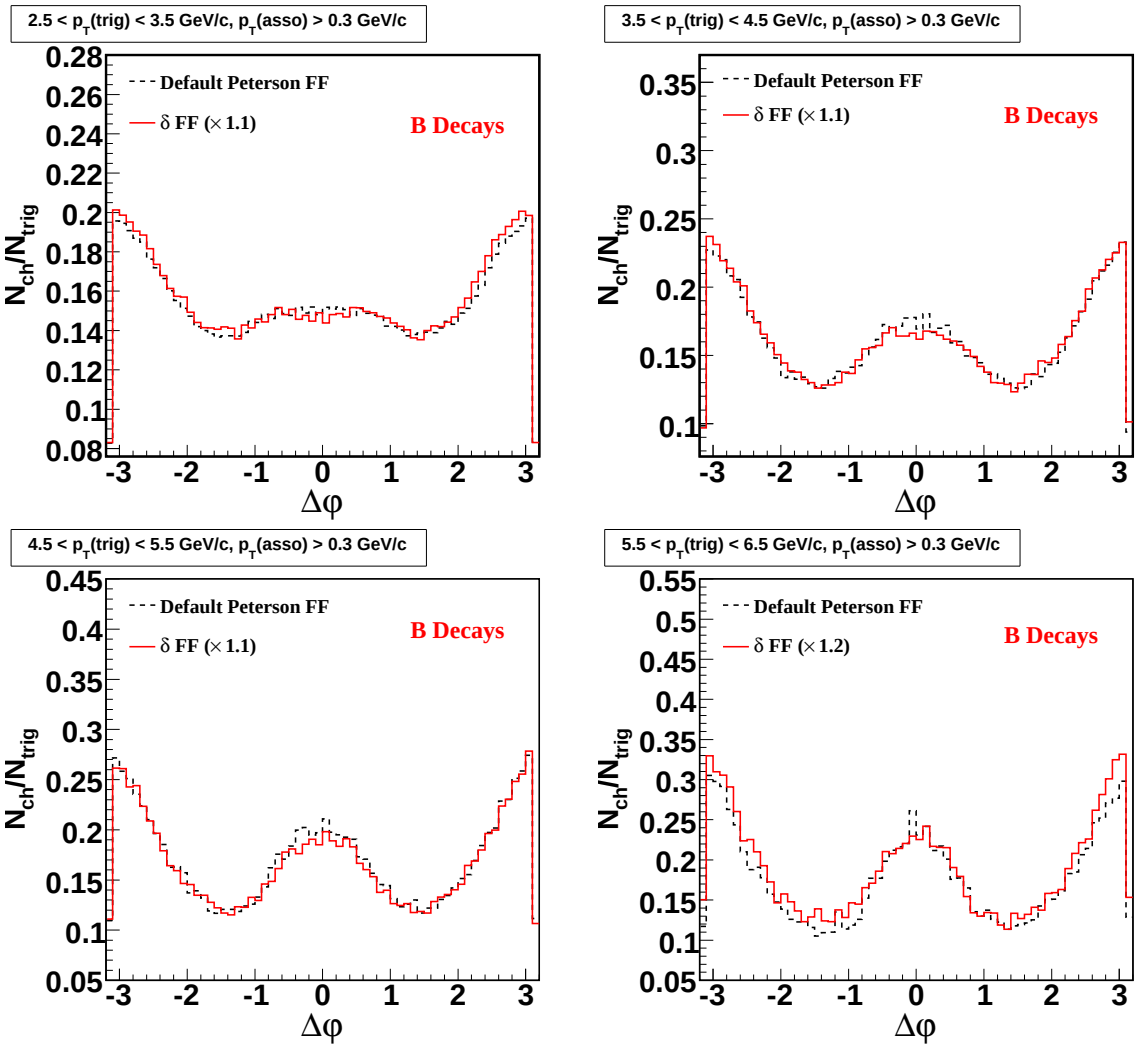

Figure 3.10: Comparison of $\Delta\varphi$ distributions for B decays between PYTHIA calculations with the default Peterson fragmentation function and the δ fragmentation function.

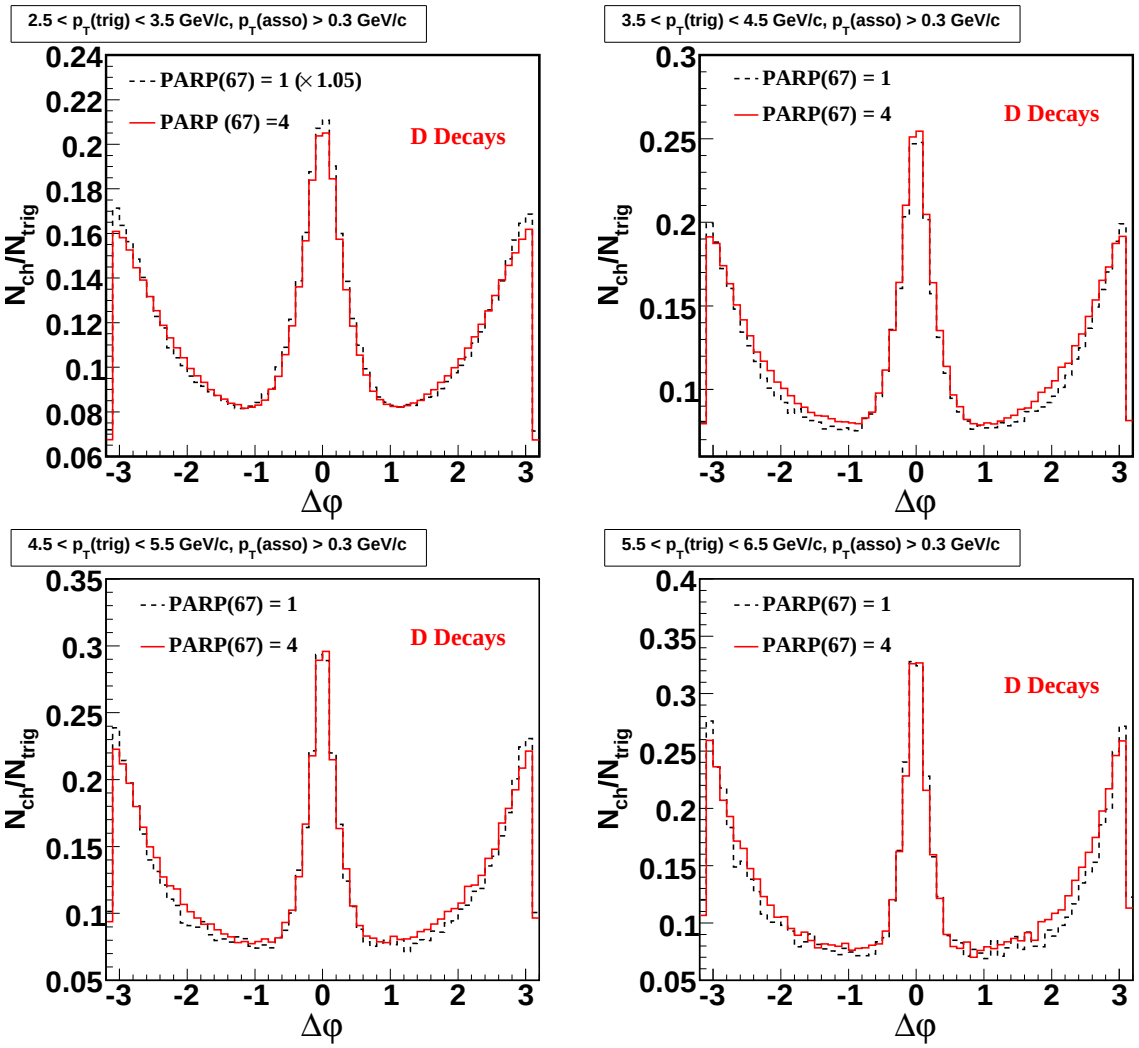

Figure 3.11: Comparison of $\Delta\varphi$ distributions for D decays between PYTHIA calculations with parameter set II and parameter set I.

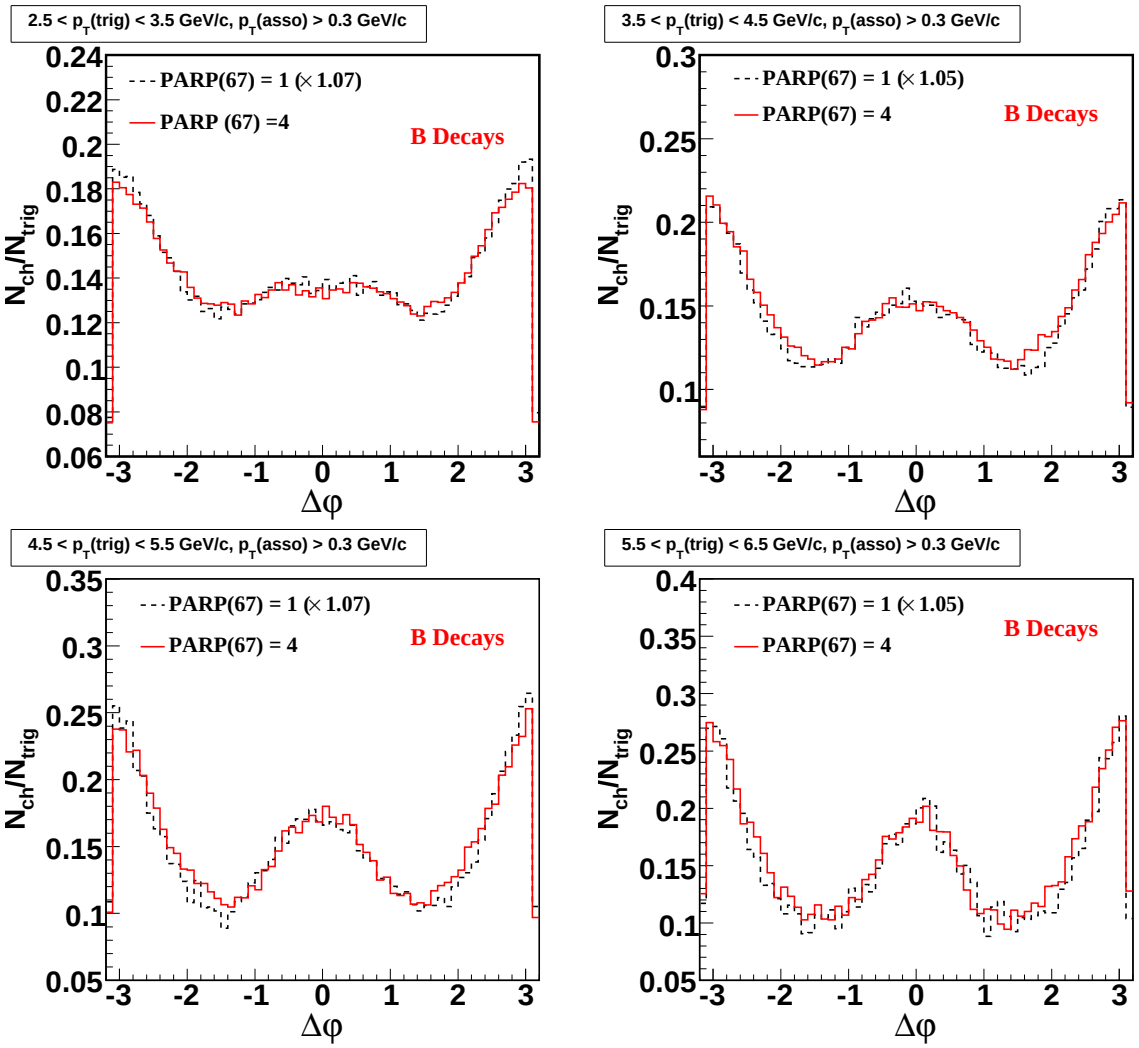

Figure 3.12: Comparison of $\Delta\varphi$ distributions for B decays between PYTHIA calculations with parameter set II and parameter set I.

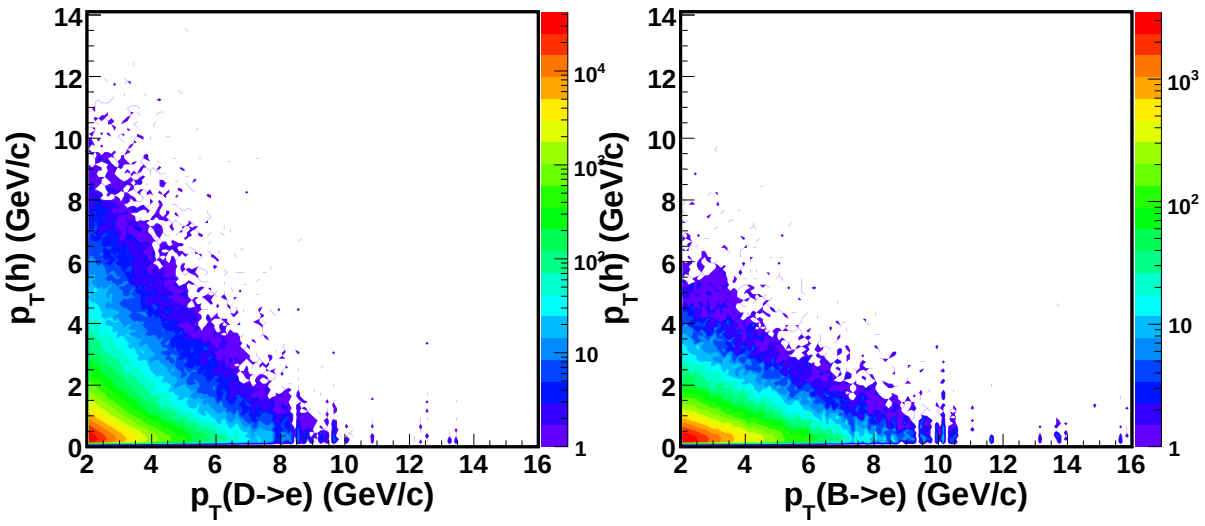

Figure 3.13: The distributions of electron p_T versus inclusive hadron p_T. Left: Electrons from D decays. Right: Electrons from B decays.

The distribution of electron p_T versus inclusive hadron p_T is different between D decays and B decays as shown in Fig. 3.13. Thus the efficiency of associated hadron p_T cut is different between D decays and B decays. Therefore, it is better to use a lower p_T cut on the associated particle in order to avoid analysis bias.

The bottom contribution to the non-photonic electrons can be determined directly from the electron spectra in PYTHIA. The results are given in the second column of Table 3.2. Note these ratios are from PYTHIA spectra without the $\sigma_{b\bar{b}}/\sigma_{c\bar{c}}$ normalization. However, this method cannot be used to determine the bottom contribution experimentally. In order to experimentally determine the bottom contribution fraction, we use the $\Delta\varphi$ distributions for B decays and D decays to fit the $\Delta\varphi$ distribution for PYTHIA inclusive case (either B decays or D decays), and let the B contribution fraction as a parameter. The fraction is determined by minimizing the χ^2 value. And the fitting error is determined by one σ shift of χ^2/ndf from the minimum value. The fitting error will be reduced by increasing the statistics. The results are shown in the third column of Table 3.2. The results are consistent with those directly from the electron spectra. This

Table 3.2: Fractions of B meson decay contributions from electron spectra and $\Delta\varphi$ distribution fitting in PYTHIA calculations with parameter set II and δ fragmentation function for charm and bottom quarks.

$p_T(trig)$ (GeV/c)	From Spectra (%)	From Fitting (%)
2.5 - 3.5	12.64 ± 0.04	12.64 ± 1.37
3.5 - 4.5	21.65 ± 0.12	21.65 ± 2.55
4.5 - 5.5	30.50 ± 0.26	30.50 ± 4.76
5.5 - 6.5	36.66 ± 0.48	36.66 ± 7.87
6.5 - 8.5	42.24 ± 0.71	42.24 ± 11.10
8.5 - 10.5	49.82 ± 1.72	49.82 ± 25.11

indicates that the method we proposed is self-consistent. This approach can be used to experimentally estimate the B and D contributions to the non-photonic electrons.

3.2.2 Particle Production in the Cone around Triggered High-p_T Non-Photonic Electrons

We further studied the particle production within a cone around triggered high p_T electrons from heavy quark decays. We focused on the scalar summed p_T distributions of inclusive charged hadrons in the cone (p_T refers to the transverse momentum in the laboratory frame). Here the cone is defined by $|\eta_h - \eta_e| < 0.35$ and $|\varphi_h - \varphi_e| < 0.35$ (η is pseudorapidity and φ is azimuthal angle). The summed p_T distributions of inclusive charged hadrons in three triggered electron p_T ranges are shown in Fig. 3.14. The distributions are scaled to unity. The dashed lines are for D decays and the solid lines are for B decays. These plots are from PYTHIA calculation with parameter set II and the δ fragmentation function for charm and bottom quarks. We also can see that there is a significant difference between B decays and D decays. The summed p_T distributions for D meson decays are much wider than those for B meson decays. The comparison

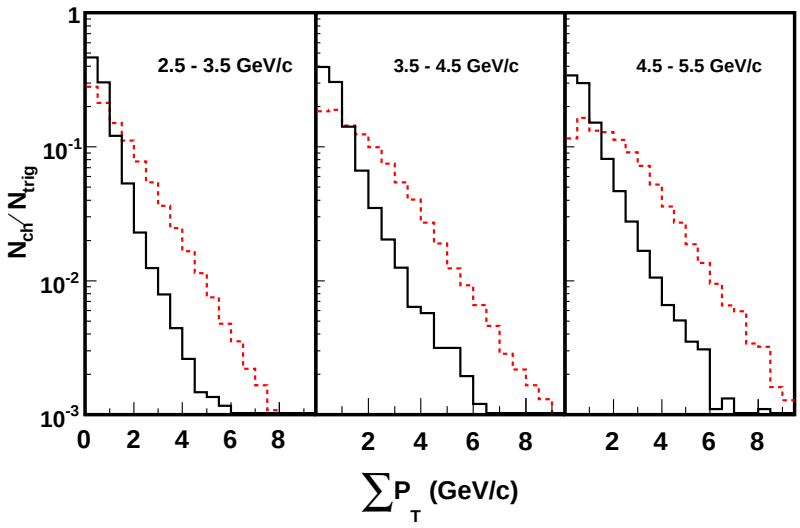

Figure 3.14: Summed p_T distributions of charged hadrons around triggered non-photonic electrons with three electron trigger p_T cuts. Solid lines show electrons from B meson decays. Dashed lines show electrons from D meson decays.

of summed p_T distributions between PYTHIA calculations with the default Peterson fragmentation function and the δ fragmentation function is shown in Fig. 3.15 for D decays and in Fig. 3.16 for B decays. The comparison of summed p_T distributions between PYTHIA calculations with parameter set II and parameter set I is shown in Fig. 3.17 for D decays and in Fig. 3.18 for B decays. We also find that the summed p_T distributions do not change significantly when varying the fragmentation function from the default Peterson function to the δ fragmentation function, and that the distributions are very close between PYTHIA calculations with parameter set II and parameter set I. The difference between B decays and D decays can also be used to distinguish B and D decay contributions. We use the summed p_T histograms from B decays and D decays to fit the summed p_T histogram from PYTHIA inclusive case to determine the B decay contribution. The results are shown in Table 3.3. The results are consistent with those directly from the electron spectra. The ratios for the same trigger p_T ranges are different between Table 3.3 and Table 3.2. It is because we removed those electrons which have no

hadrons in the cone around them when we calculated the bottom contribution from the electron spectra for Table 3.3. This removes different fractions from B and D decays, which has to be corrected by simulations. This was done to make the results directly from the electron spectra comparable to the results from hadron summed p_T histogram fitting. It will be more practical for small acceptance experiments to investigate the B decay contribution using summed p_T histogram fitting.

Table 3.3: Fractions of B meson decay contributions from electron spectra and summed p_T histogram fitting in PYTHIA calculations with parameter set II and the δ fragmentation function for charm and bottom quarks.

$p_T(trig)$ (GeV/c)	From Spectra (%)	From Fitting (%)
2.5 - 3.5	8.25 ± 0.05	8.25 ± 1.50
3.5 - 4.5	14.94 ± 0.13	14.94 ± 2.54
4.5 - 5.5	22.60 ± 0.29	22.60 ± 4.13

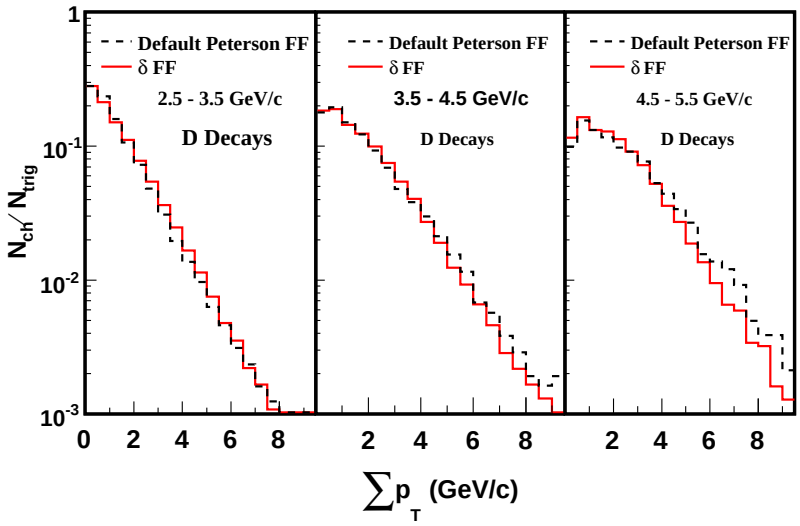

Figure 3.15: Comparison of summed p_T distributions for D decays between PYTHIA calculations with the default Peterson fragmentation function and the δ fragmentation function.

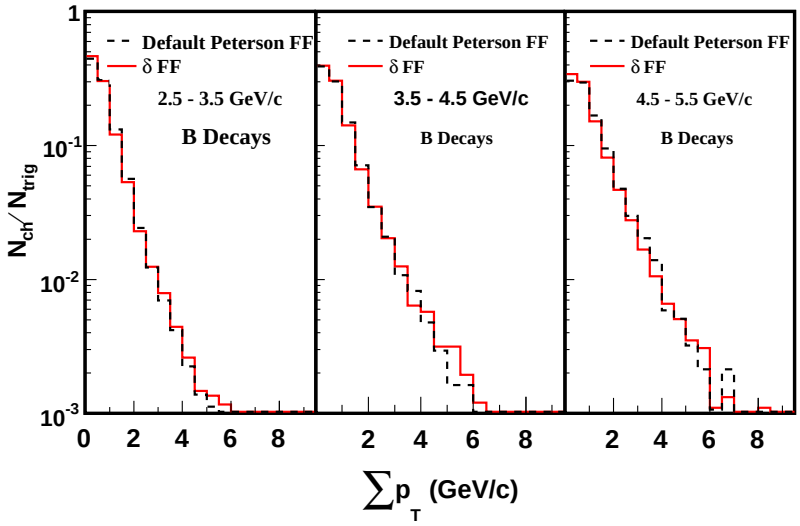

Figure 3.16: Comparison of summed p_T distributions for B decays between PYTHIA calculations with the default Peterson fragmentation function and the δ fragmentation function.

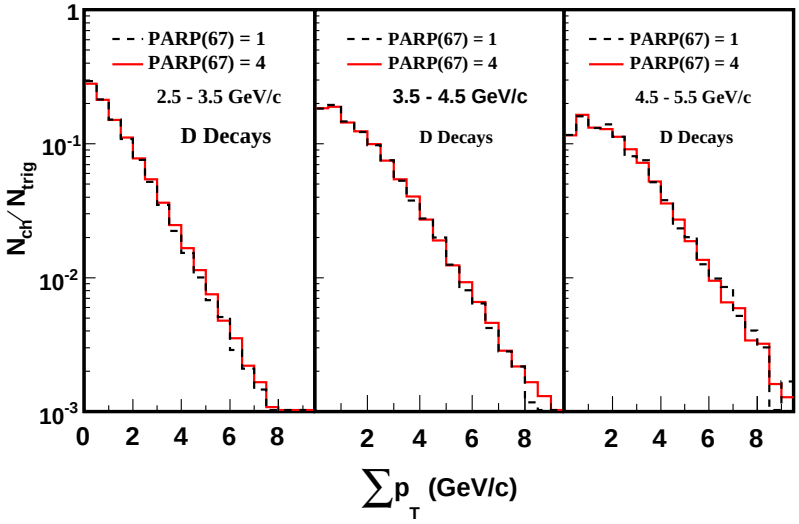

Figure 3.17: Comparison of summed p_T distributions for D decays between PYTHIA calculations with parameter set II and parameter set I.

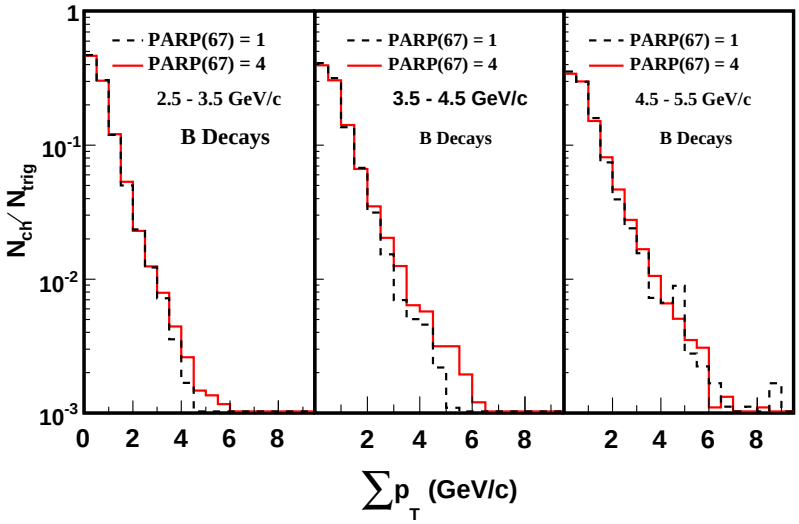

Figure 3.18: Comparison of summed p_T distributions for B decays between PYTHIA calculations with parameter set II and parameter set I.

CHAPTER 4

Data Analysis

This chapter is dedicated to a detailed description of the analysis for the azimuthal correlations between non-photonic electrons and charged hadrons. We start this chapter by presenting the data set that is used in this analysis, including trigger selection, event vertex cut, etc. The analysis procedure includes inclusive electron identification and background electron removal. We will give a detailed description of the method and procedure to extract the signal of e-h azimuthal correlations. We end this chapter by showing the results of the non-photonic electron azimuthal correlations with charged hadrons.

4.1 BEMC High Tower Trigger

The STAR trigger system [Bie03] is a 10 MHz pipelined system based on a fast detector output that controls the event selection for the much slower tracking detectors. The trigger system is functionally divided into different levels with level 0 being the fastest while level 1 and level 2 are slower. The final trigger decision is made in level 3 based on tracking in the slow detectors. The level 0 trigger is distinct from all higher levels in that level 0 selects events for processing while all other levels only function as event aborts. The level 0 is the only level which does not incur large dead times from the opening of the gating grid in the TPC. It is deadtimeless and capable of action on each RHIC beam crossing.

The BEMC is an important part of STAR's level 0 trigger, capable of triggering on high p_T physics through its electromagnetic component. It is fast and sensitive to the

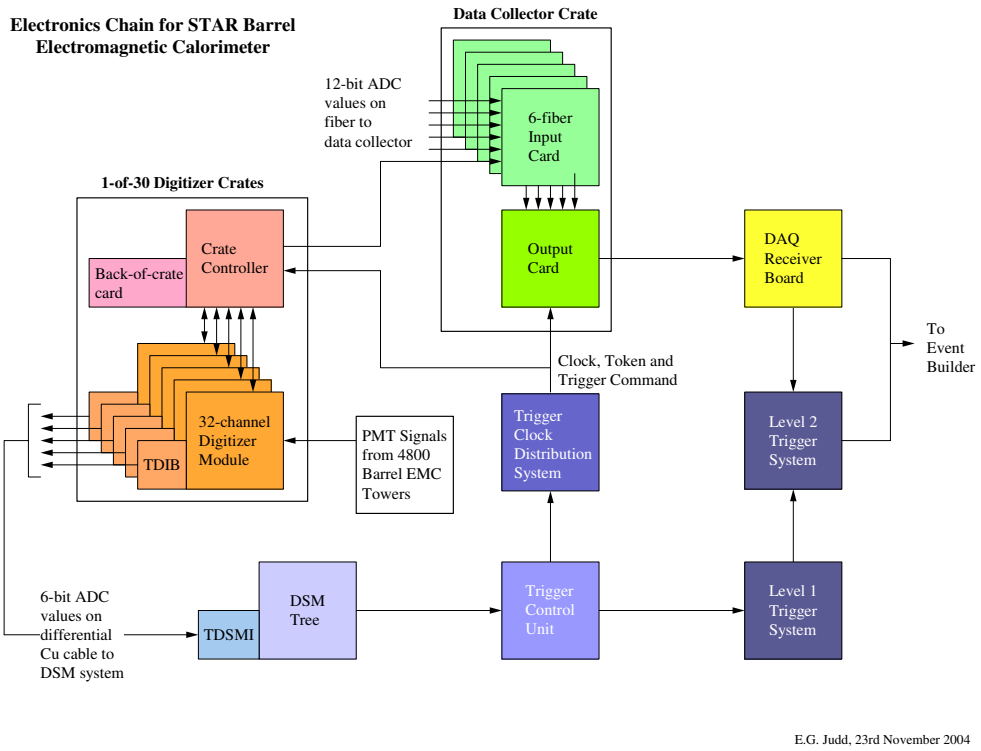

Figure 4.1: The trigger and data acquisition electronics chain for the STAR BEMC [Sta].

energy from electromagnetic showers.

The STAR level 0 trigger needs to provide a trigger to the TPC within about 1 μs ($\sim$10 RHIC crossings) and to the STAR level 0 trigger processors within about 700 ns, including cable delays. For reasons of speed and limited bandwidth, the EMC trigger uses trigger primitives instead of the full EMC data. There are two kinds of trigger primitives from the EMC front end electronics. One set of primitives called "patch trigger" consists of 300 tower sums, digitized to 6 bits each, from patches of 0.2 by 0.2 in $\eta - \phi$. The other set of primitives called "high tower trigger" is 300 high tower values of 6 bits from the single largest 0.05×0.05 tower signal within each 0.2×0.2 patch. These primitives are processed to make final trigger decisions based on total E_T, jet triggers, photon triggers, etc. These results are then passed to STAR level 0 in 700 ns to participate as a component of the final level 0 decision [Bed03]. The trigger and data

acquisition electronics chain for the STAR BEMC is shown is in Fig. 4.1.

Of interest to the analysis in this dissertation is the high tower trigger. Events with an energy deposition in a single tower of the BEMC above a certain threshold can be selected to enhance the sample of events, in which a high transverse momentum photon or electron is produced.

4.2 Event Selection

The data set used in this analysis is p+p events at $\sqrt{s_{NN}} = 200$ GeV recorded by STAR in Run-5. As discussed in section 2.2, the main detectors utilized in this analysis are the TPC and the BEMC with SMD. We require both the TPC and BEMC information.

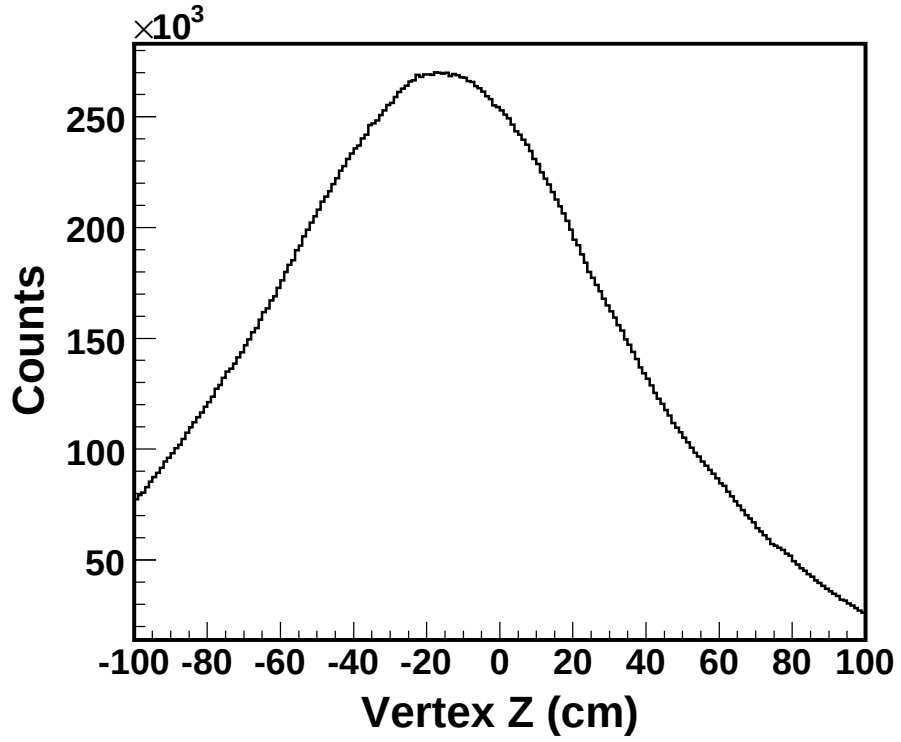

Figure 4.2: The position of the primary vertex Z for p+p run in year 2005.

In RHIC Run-5, the STAR detector has accumulated several data sets from p+p

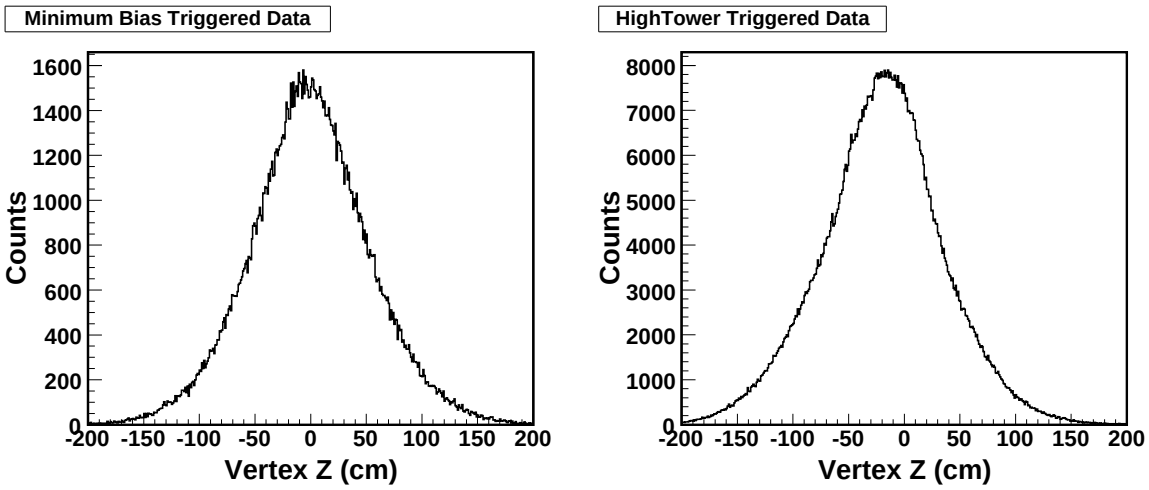

Figure 4.3: Left: The position of the primary vertex Z for minimum bias triggered events. Right: The position of the primary vertex Z for BEMC high tower triggered events. The statistics used to make these two plots is only about 10% of that is used to produce Fig. 4.2.

collisions at $\sqrt{s_{NN}}$ = 200 GeV, including minimum bias triggered data[1], BEMC high tower triggered data, jet patch triggered data, etc. For this dissertation research, we use the BEMC high tower triggers to enrich the event samples with high p_T electrons producing signals in the calorimeter. The threshold for HighTower-1 and HighTower-2 is the energy deposition in a single tower of the BEMC of 2.6 GeV and 3.5 GeV, respectively. The STAR magnet has been run in full field and half field configurations during p+p data taking in Run-5. In this analysis, we make use of events where the STAR magnet was operating at the full field.

Our analysis was restricted to events with a primary vertex Z from -40 cm to 30 cm of the center of the TPC along the beam direction. Fig. 4.2 shows the position distribution of primary vertex Z. The offset to negative Z region of primary vertex Z distribution is due to the trigger setup. Fig. 4.3 shows primary vertex Z distributions

[1]The minimum bias p+p events are triggered on a coincident signal of two Beam-Beam Counters(BBCs), which are mounted around the beam pipe at ±3.7 m from the interaction point, covering pseudorapidity $3.4 < |\eta| < 5.0$ [Kir03].

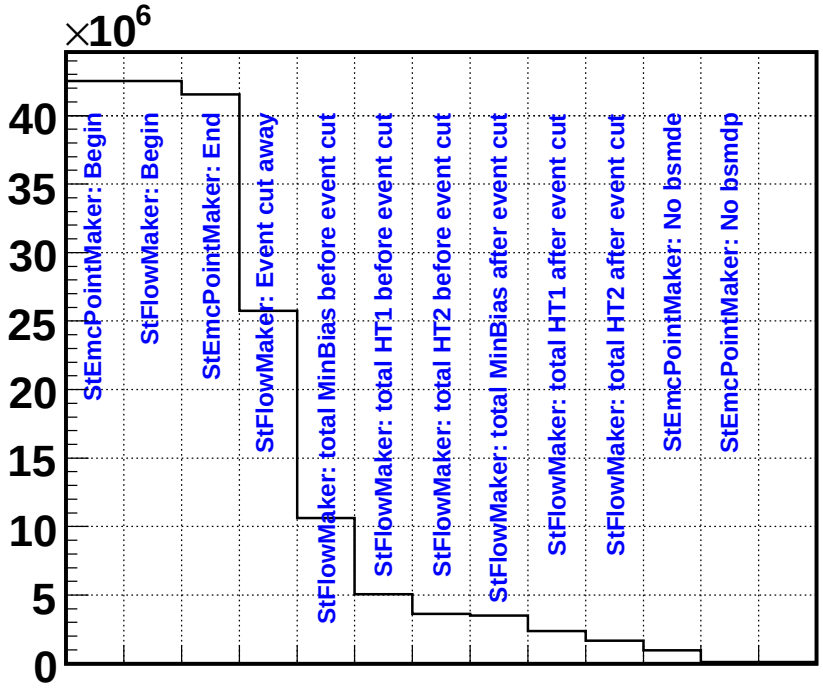

Figure 4.4: Detailed event statistics for p+p 200 GeV e-h analysis. Only events with valid BEMC information, high tower triggers and satisfying the vertex Z cut are kept.

for minimum bias triggered events (left panel) and BEMC high tower triggered events (right panel). An apparent asymmetry exists in the BEMC high tower triggered events. HighTower-1 and HighTower-2 only triggered in the west half ($+Z$) of the BEMC during Run-5. The effective threshold in the barrel depends on the vertex position. The farther negative the vertex Z, the lower the effective threshold, thus the more events pass the threshold in the negative Z region. We apply an asymmetric primary vertex Z cut in order to maximize the statistics and minimize the photon conversion background from material in the STAR detector configuration.

Fig. 4.4 shows a detailed tally of event statistics used in this analysis. There are about 42.5 million full-field events with valid BEMC information and TPC information. After various event selections and cuts about 2.4 million HighTower-1 full-field events and 1.7 million HighTower-2 full-field events were used to produce the results shown in

this dissertation.

4.3 Electron Identification and Hadron Rejection

Electron identification was carried out by combining ionization energy loss in the TPC with energy deposition in the BEMC and shower profile in the SMD. Note that for the electron identification, we didn't do trigger selection for the data set.

4.3.1 dE/dx from the TPC

The TPC is the main tracking detector in STAR for identifying charged particles as discussed in section 2.2.1. The measurement of the ionization energy loss, dE/dx, for charged tracks in the TPC gas is used to identify electrons in the first stage. Fig. 4.5 shows the distribution of dE/dx versus momentum for the tracks satisfying the following requirements:

- -0.7 < psedorapidity η < 0.7
- 20 < No. of fit points < 50
- 15 < No. of dE/dx points < 100
- 0.52 < No. of fit points divided by No. of maximum points < 1.2
- 0 < Chi square < 3.0
- 0 < Global DCA < 1.5

The reason to set up those cuts will be discussed in Table 4.1. The electron band crosses the hadron bands as shown in Fig. 4.5. Therefore, the TPC alone can give useful but not definitive information for electron identification. Fig. 4.6 is the projection of Fig. 4.5 onto the dE/dx axis with a transverse momentum cut of $p_T > 2.0$ GeV/c. We can see two peaks with the electron dE/dx peak to the right and the hadron dE/dx peak to the left. The ramp on the right side of the electron dE/dx peak is due to track merge.

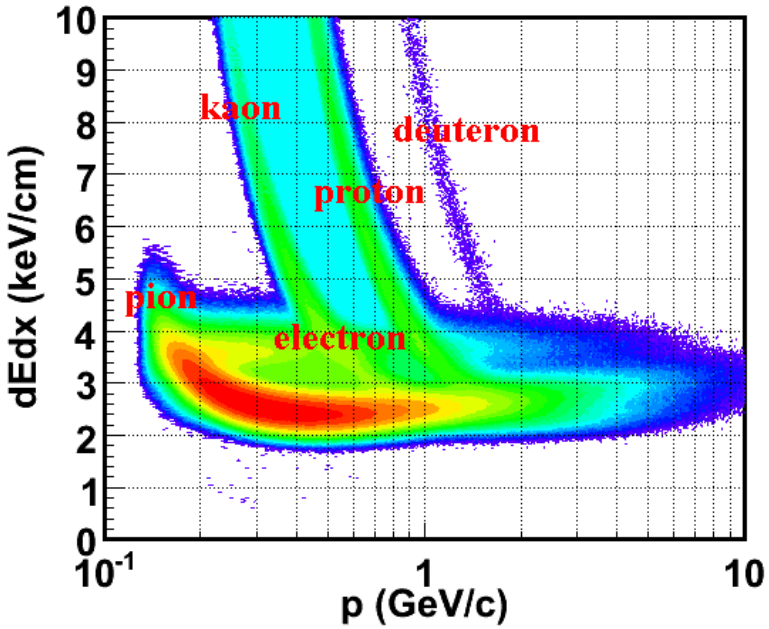

Figure 4.5: The distribution of dE/dx versus momentum for 2005 p+p data.

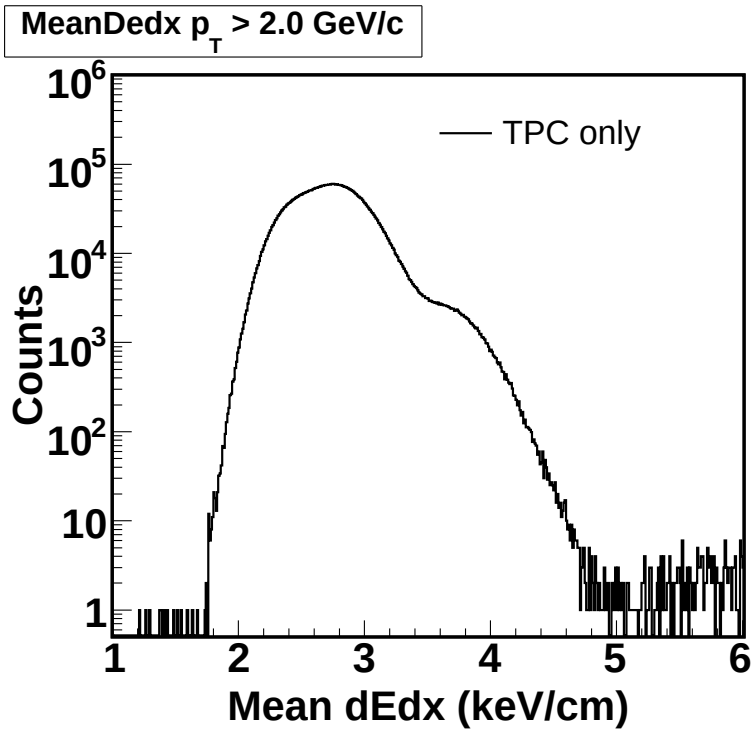

Figure 4.6: The projection of Fig. 4.5 with a p_T cut of $p_T > 2.0$ GeV/c.

If two tracks are very close to each other, the TPC track reconstruction software tends to reconstruct them as one track with dE/dx equaling the sum dE/dx of them. With the TPC only, the electron peak and hadron peak are not well separated, and the signal (electron) to background (hadron contamination) ratio is small. Although requiring the dE/dx values of the selected tracks to be near the expected electron band rejects a significant fraction of the hadron contamination, the TPC's particle identification ability is not enough to completely separate hadrons from electrons. For the e-h correlation study, we demand a very pure electron sample. Thus, additional detectors are needed for electron identification.

4.3.2 Information from the BEMC with SMD

The TPC reconstructed charged tracks with $p_T > 2.0$ GeV/c are extrapolated onto the BEMC tower inner plane, the SMD η plane and the SMD ϕ plane respectively. Electrons and photons will go into the BEMC towers, create electro-magnetic showers and deposit almost all of their energies in the BEMC. Therefore, the BEMC provides the energy information for these particles. The SMD, which is about 5 radiation lengths below the inner surface of the BEMC, is used to measure the positions and the sizes of the showers. The software package to reconstruct electro-magnetic particles by reconstructing their showers has been developed by Dr. Dong. See reference [Don06] for a detailed discussion on the reconstruction of these electro-magnetic particles and for the comparison between the software developed by Dr. Dong and other available software packages.

Only some towers in the east half ($-Z$) of the BEMC were calibrated for some of the runs during Run-5 p+p collisions, and there is no SMD in the east half of the BEMC. HighTower-1 and HighTower-2 only triggered in the west half of the BEMC. Thus, we only use the data from the west half of the BEMC. The TPC tracks are projected onto three planes of the 60 modules in the west half of the BEMC. A virtual projection point is the combination of the information from the three separated projections. The projections onto the SMD η and ϕ planes provide the η and ϕ information. The BEMC point reconstruction software developed by Dr. Dong is used to reconstruct the BEMC

points. Each BEMC point has a tower which geometrically contains the projection point to the tower inner plane, and is associated with the TPC track. More than one reconstructed BEMC points can share a tower hit, thus multiple BEMC points can be associated with one TPC track. More than one TPC tracks can also share one tower. One requirement for electron candidate is that the track should have at least one associated BEMC point.

Ratio of p/E

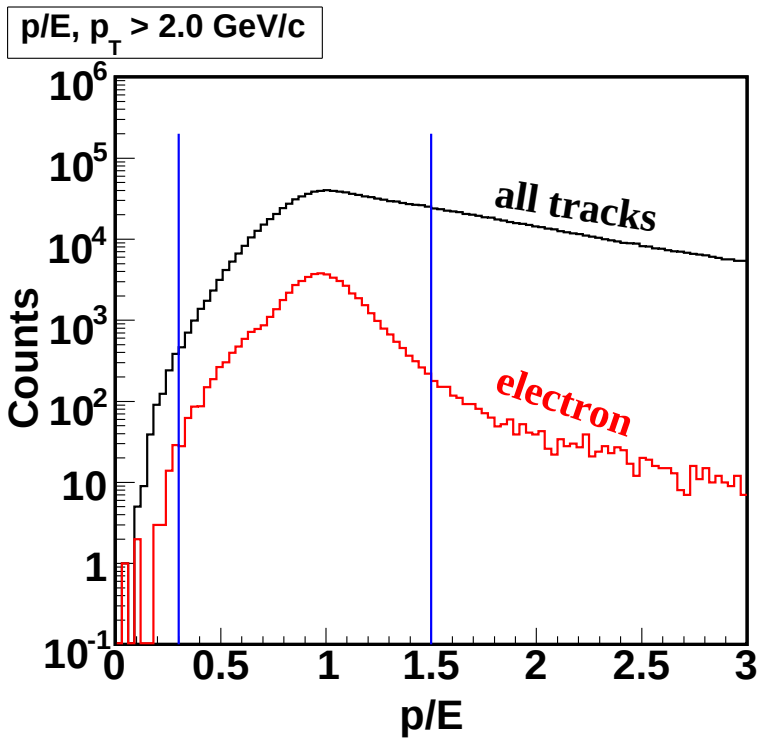

Figure 4.7: The red curve is the p/E distribution for electron candidates. The black curve is the p/E distribution for all tracks passing the basic track quality cuts and with BEMC association. The blue lines denote where we set the cut.

The BEMC towers have about 21 radiation lengths. When electrons strike the towers, they will deposit almost all of their energy in the towers. Hadrons, even those

which shower within the calorimeter, typically deposit far less than their total energy in a tower. Thus, the comparison of the TPC tracked momentum to the tower energy, p/E, is an electron identifier. The ratio of p/E should be around one for electrons.

Fig. 4.7 shows the p/E distribution for electrons candidates (red curve) as well as the p/E distribution for all tracks passing the basic track quality cuts and with BEMC association (black curve). Here, the electron candidates mean the tracks passing all the other electron identification cuts, including the number of SMD hit cut, projection distance cut and dE/dx cut, except the p/E cut. A cut of $0.3 < p/E < 1.5$ can keep most of the electrons going into the BEMC while rejecting a lot of hadrons.

Number of SMD Hits

Hadronic showers are typically incompletely developed by the $\sim 5X_0$ depth of the SMD, where the electromagnetic showers from electrons and photons have their maximal spatial extent. Therefore, the number of SMD hits produced by hadrons, in general, is smaller than that produced by electrons. The resulting difference of the number of SMD hits is used for additional hadron suppression. The upper panel of Fig. 4.8 shows the number of SMD hits for electron candidates which pass all other electron identification cuts except the number of SMD hits cut. The bottom panel of Fig. 4.8 is the number of SMD hits for TPC preselected hadrons, which have dE/dx 3σ away from the electron dE/dx band and pass the basic track quality cuts. The difference of number of SMD hits between electrons and hadrons can be clearly seen. We require $1 <$ Number of SMD η Hits < 15 and $1 <$ Number of SMD ϕ Hits < 15 for electron candidates.

Projected Position Match

The BEMC matches the acceptance of the full TPC for tracking. Some TPC tracks are associated with the BEMC points due to random combinatorics. We compare the distance between the TPC track projection position and the reconstructed BEMC point position. Due to the poorly developed showers in the case of hadrons, this distance

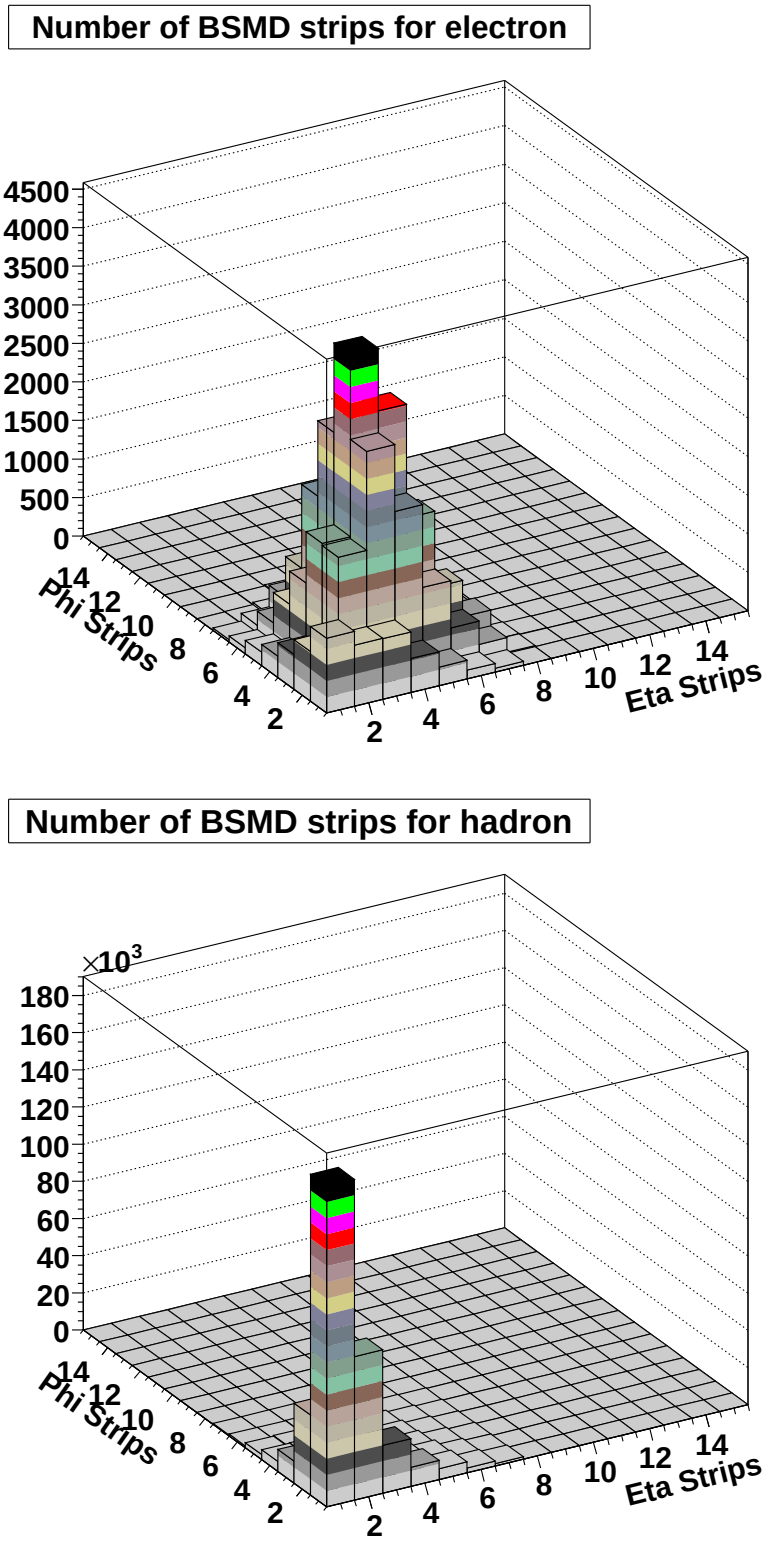

Figure 4.8: The number of SMD hits for electron candidates (upper panel) and hadrons (bottom panel).

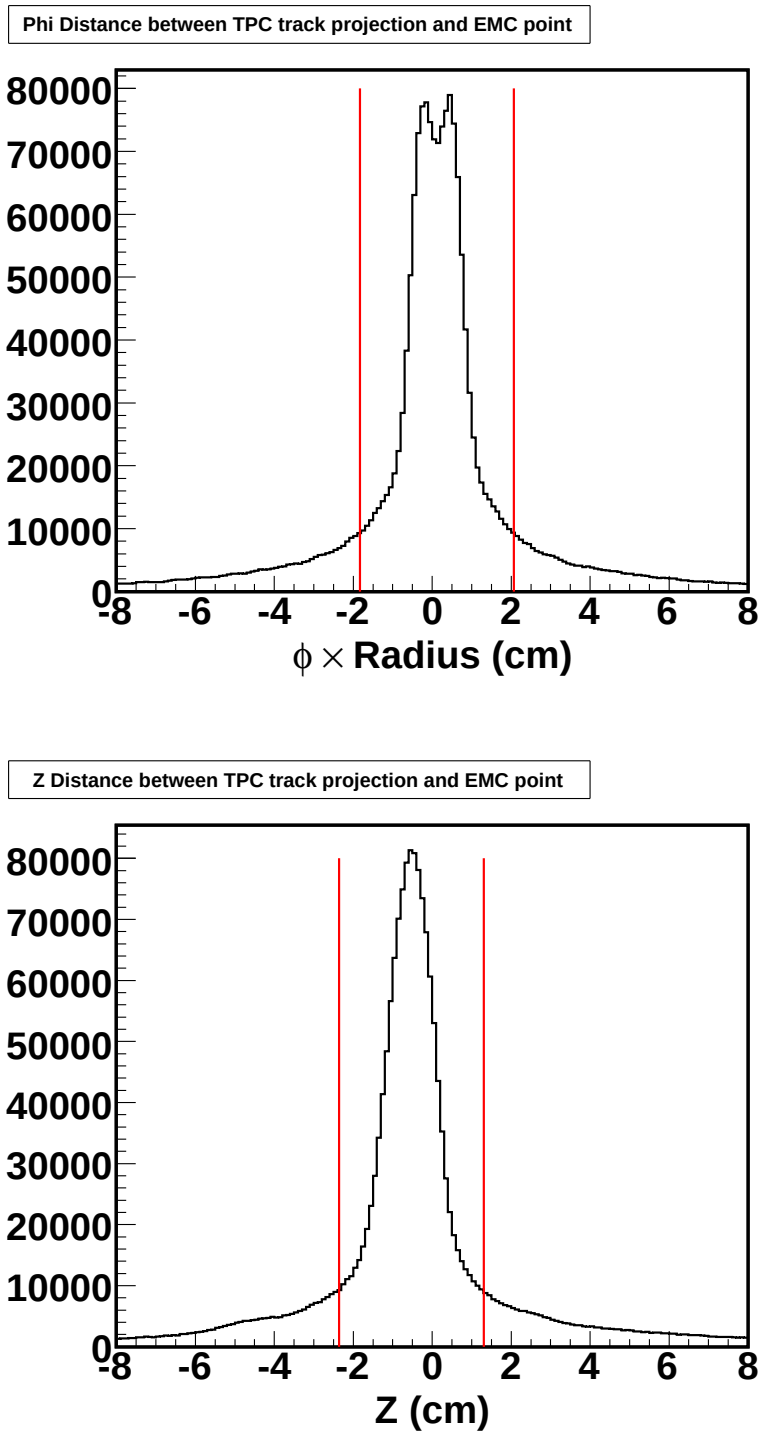

Figure 4.9: The distance between the TPC track projection position and the reconstructed BEMC point position in ϕ direction (upper panel) and Z (η) direction (bottom panel) for all tracks with BEMC point association.

will have a much wider distribution for hadrons than for electrons. The high spatial resolution of the SMD allows us to cut away a lot of the random associations by cutting on this distance. Fig. 4.9 shows the distributions of the difference between the projected TPC track position and the BEMC reconstructed shower position in ϕ direction (upper panel) and Z (η) direction (bottom panel). The distribution of ϕ difference has two peaks and the distribution of Z (η) difference is offset to a slightly negative value. These characteristics are due to a slightly inaccurate radius value used in the software for the inner plane of the BEMC. The lines in Fig. 4.9 denote where we set the cuts. They are about 3σ on each side of the peaks.

4.3.3 All Electron Identification Cuts Combined

Fig. 4.10 shows how the dE/dx distribution changes when the BEMC and SMD electron identification cuts applied one by one. The BEMC and SMD electron identification cuts dramatically reduce hadron contamination while not reducing electron sample much. The electron signal to hadron contamination ratio is enhanced after all the cuts are combined; and the electron peak and hadron peak are well separated.

The resulting dE/dx distribution is fit with multiple Gaussian functions. Two of them are used to fit the hadron dE/dx peaks and one of them is used to fit the electron dE/dx peak. Fig. 4.11 shows the dE/dx distributions of the tracks after the BEMC and SMD cuts with three Gaussian fits for four p_T bins. The lines in Fig. 4.11 denote a final dE/dx cut applied to the tracks. The value of the final dE/dx cut is chosen by balancing between statistics and the purity of electron sample. It is approximately from -0.5σ to 3σ on the electron dE/dx band. Table 4.1 lists a summary of all the electron identification cuts.

The purity of the inclusive electron sample is calculated from the fit and cut parameters. It is defined as the number of inclusive electrons passing the electron identifications cuts divided by the number of all the tracks satisfying the same cuts. Table 4.2 gives the purity of the final inclusive electron sample. After all the TPC, BEMC and SMD cuts are combined, the purity of electron sample is above 98% up to $p_T \sim 6.5$ GeV/c.

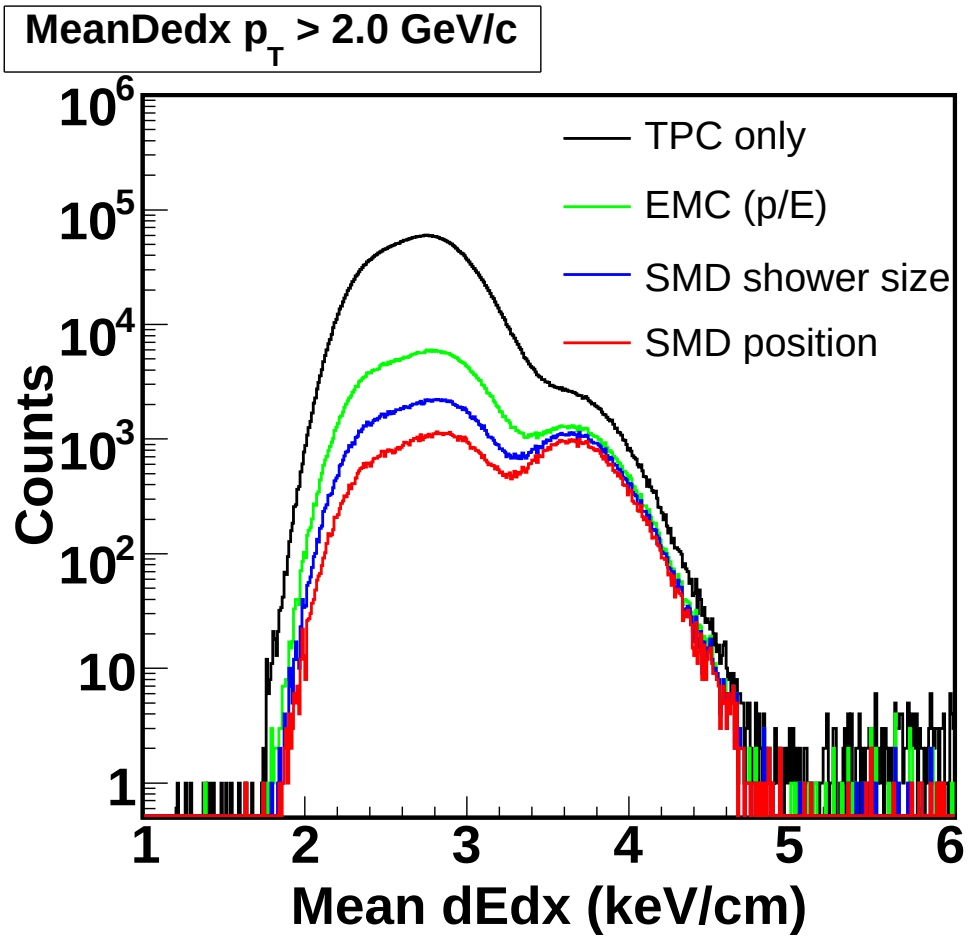

Figure 4.10: The dE/dx distributions of the tracks after applications of each BEMC and SMD electron identification cut.

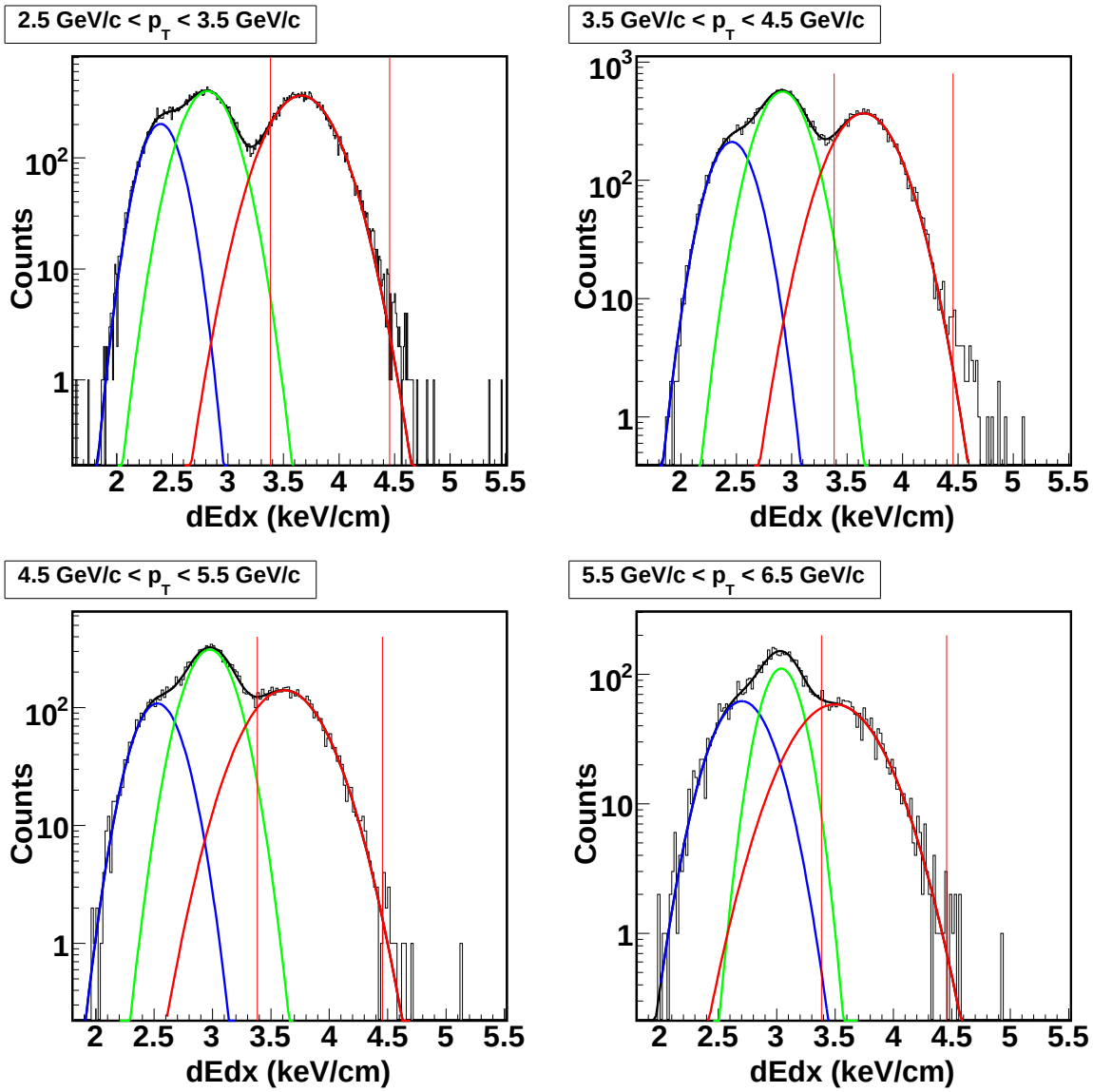

Figure 4.11: The dE/dx distributions of the tracks after BEMC and SMD electron identification cuts for p_T between 2.5 GeV/c to 6.5 GeV/c in four bins. Three Gaussian functions are used to fit the dE/dx distributions, with two of them for hadron dE/dx peaks and one of them for the electron dE/dx peak.

Table 4.1: The summary of electron identification cuts.

Parameter	Value	Comments
No. of fit points	[20, 50)	Ensure good track quality
No. of dE/dx points	[15, 100)	Ensure good track quality
Ratio of No. of fit points to No. of maximum points	[0.52, 1.2)	Eliminate the double counting of split tracks
Chi square	[0, 3)	Ensure good track quality
Global DCA	[0, 1.5)	Reduce photonic electron background
Pseudorapidity η	[-0.7, 0.7)	Avoid large conversion background from the detector material
Transverse momentum p_T	$\geq$ 2.0 GeV/c	Avoid the overlapping region in dE/dx between electrons and deuterons and protons. Ensure good response from BEMC for EM showers.
dE/dx (keV/cm)	[3.3839, 4.4556)	About -0.5σ to 3σ
p/E	[0.3, 1.5)	p/E should be around one for electrons.
No. of SMD η hits	[2, 15)	Electrons have larger shower size than hadrons
No. of SMD ϕ hits	[2, 15)	Electrons have larger shower size than hadrons
Projection distance in ϕ ($\times$ SMD ϕ radius) (cm)	[-1.8325, 2.0699)	About -3σ to 3σ
Projection distance in Z (cm)	[-2.3640, 1.3092)	About -3σ to 3σ

Table 4.2: The purity of the inclusive electron sample.

Electron p_T (GeV/c)	Purity
2.5 - 3.5	$99.84 \pm 0.28\%$
3.5 - 4.5	$98.94 \pm 0.72\%$
4.5 - 5.5	$98.05 \pm 1.56\%$
5.5 - 6.5	$98.39 \pm 2.29\%$

4.4 Photonic Electron Background Reconstruction

In the STAR environment, the inclusive electron sample consists of several sources of electrons:

- Photon conversions ($\gamma \longrightarrow e^+ + e^-$) in the detector material between the interaction point and the TPC. There are several sources for the conversion photons: direct photons, photons from π^0, η decays, etc.
- π^0, η, etc. scalar meson Dalitz decays.

  $\pi^0 \longrightarrow e^+ + e^- + \gamma$ $(1.198 \pm 0.032)\%$

  $\eta \longrightarrow e^+ + e^- + \gamma$ $(0.60 \pm 0.08)\%$
- ρ, ω, ϕ vector meson Dalitz decays and/or di-electron decays.
- Kaon decays
- Heavy quark (charm and bottom) hadron semi-leptonic decays.
- Other possible contributions such as Dell-Yan, heavy quarkonium decay, thermal electrons, etc.

In this analysis, semi-leptonic decay of heavy flavor hadrons is the source of the electron signal — non-photonic electrons. Other possible sources such as Dell-Yan, heavy

quarkonium decay, thermal electrons, etc are believed to have negligible contributions as shown in the theoretical predictions [Sjo01, Rap01]. The first four sources are considered to be photonic background. As studied in the Ref. [Adc02, Don05], the dominant sources of photonic electron background are photon conversions, π^0 and η Dalitz decays. Contributions from all other sources of photonic background combined are only a few percent of the total background and can be ignored when compared to systematic uncertainties. Here, we reconstruct the dominant sources of photonic background.

The invariant mass of electron-positron pairs from photon conversions or Dalitz decays will be very small, while there is no such correlation for non-photonic electrons. Thus the photonic background can be reconstructed by pairing electrons/positrons with their partners and calculating their invariant mass.

As a first step in this procedure, we use electron identification criteria to tag one electron/positron track from the primary collision vertex, and find the corresponding global track of the primary electron/positron track[2]. As a second step we loop all other global tracks in the same event in order to find the partner track of the tagged electron/positron. Those tracks which have $p_T > 0.1$ GeV/c within the TPC acceptance and pass a loose cut on dE/dx around the electron band are considered as the partner tracks. The dE/dx cut for the partner tracks is from -3σ to 3σ. The reason we use loose cuts for the partner track is to maximize the partner finding efficiency. Then as a third step we calculate the Distance of Closest Approach (DCA) of the global electron/positron track and its partner track. Then we trace the momenta of these two global tracks back to the point where the DCA of the pair is located, and we calculate invariant mass of the pair using the momenta at the DCA of the pair. Before we pair electrons/positrons with their partners, we apply some geometric cuts on the pairs such as DCA, opening angle, etc. Fig. 4.12 shows the distributions of DCA and angles of opposite sign and same sign electron pairs. The cuts we used are listed in Table. 4.3.

The invariant mass distribution of e^+e^- pairs are depicted by the grey filled area in Fig 4.13. This sample contains the true photonic background as well as the combina-

[2]Every primary track has a corresponding global track but not vice versa.

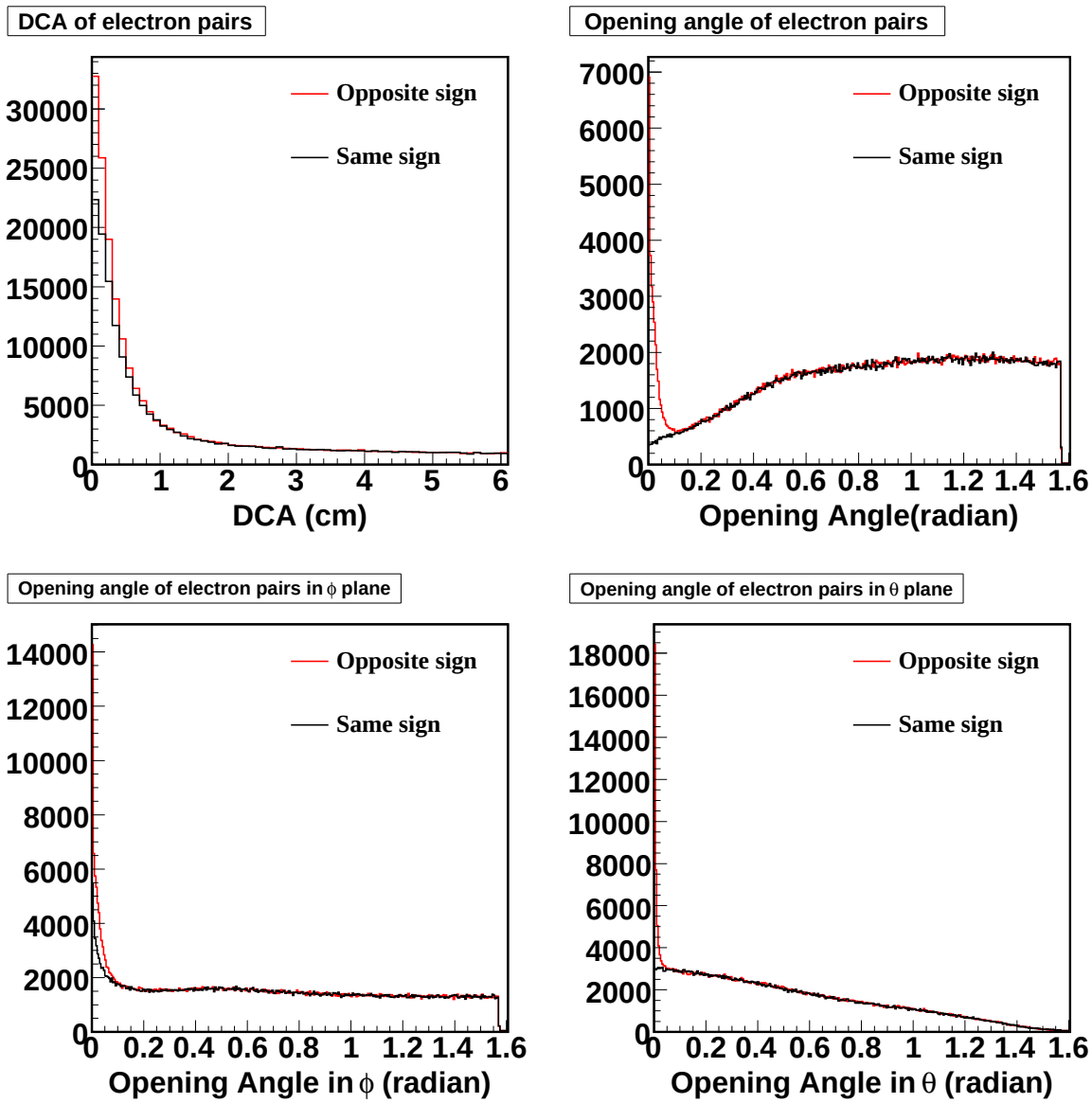

Figure 4.12: The distributions of DCA and angles of opposite sign and same sign electron pairs.

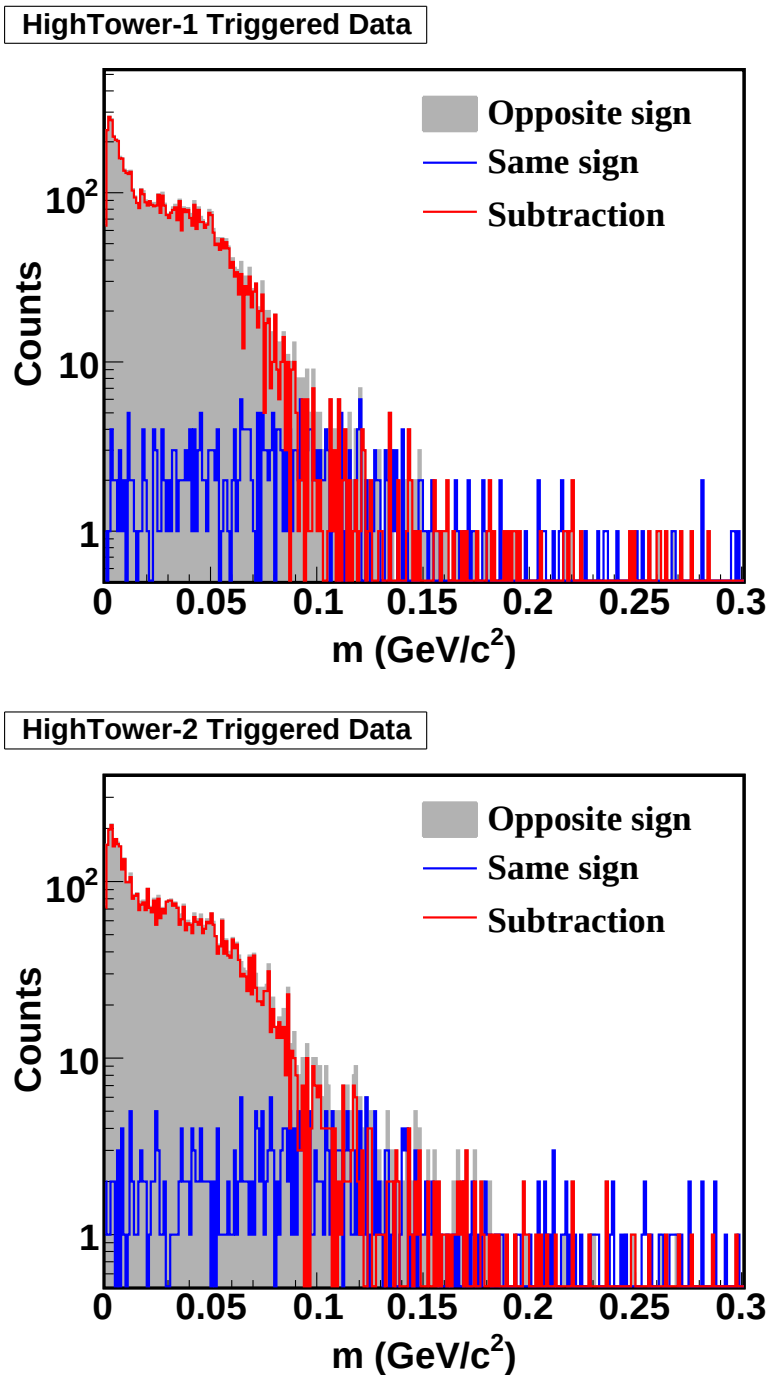

Figure 4.13: Invariant mass distributions of opposite sign electron pairs and combinatorial background (same sign electron pairs) for HighTower-1 triggered data in upper panel and HighTower-2 triggered data in bottom panel.

Table 4.3: Geometric cuts of the pairs for the invariant mass method.

Variable	Cut
Track to Track DCA (cm)	(0, 1)
Opening Angle (radian)	(0, 0.15)
Opening Angle in ϕ (radian)	(0, 0.1)
Opening Angle in θ (radian)	(0, 0.05)

torial background, where non-photonic electrons may be falsely identified as photonic electrons. The combinatorial background can be estimated by calculating the invariant mass of same-sign electron pairs shown as blue solid curve in Fig 4.13. The combinatorial background is small in p+p collisions. The red solid curve in Fig 4.13 is the subtraction. From the red curve an apparent sharp peak near zero can be seen in the invariant mass distribution. A cut of mass < 0.1 GeV/c^2 removes most of photonic background. The secondary broad peak on the right side in the invariant mass distribution is caused by the limited TPC tracking resolution [Don06]. For convenience, we refer to those electrons having opposite sign partners and their invariant masses satisfying the mass cut as the *OppSign* sample which contains the true reconstructed photonic background and random combinatorics, and those electrons having same sign partners and their invariant masses satisfying the mass cut as the *SameSign* sample which is a close approximation of random combinatorics. Then the reconstructed photonic background (*Reco-Pho*) can be obtained by Eq. 4.1.

$$Reco\text{-}Pho = OppSign - SameSign \tag{4.1}$$

The true photonic electrons (*Pho*) can be estimated by Eq. 4.2,

$$\begin{aligned} Pho &= Reco\text{-}Pho + Not\text{-}Reco\text{-}Pho \\ &= \frac{Reco\text{-}Pho}{\varepsilon} = \frac{OppSign - SameSign}{\varepsilon} \end{aligned} \tag{4.2}$$

where ε is the efficiency of this invariant mass method which can be calculated from simulations. The previous analysis has shown that the photonic electron reconstruction efficiency, ε, is around 70% in p+p collisions for the p_T region that we are studying [Abe06b]. We will use this value for our analysis. The uncertainties of photonic electron reconstruction efficiency will be the dominant source for the systematic error of our final results.

Fig. 4.14 shows the ratio of inclusive electron to photonic background as a function of p_T. The bars (boxes) on the data points indicate the size of statistical (systematic) errors. A significant excess of electrons with respect to the background has been observed; and these excess electrons are mostly from heavy quark semi-leptonic decays. In Run-5 there was an increase in the amount of material producing photon conversions in the STAR experimental configuration than for Run-3 and Run-4. This leads to inclusive electron to photonic background ratios from Run-5 systematically lower than those from Run-3 and Run-4 [Abe06b].

4.5 Method for Extraction of e-h Azimuthal Correlation Signal

The physics signal in this analysis is the non-photonic electron ($Non\text{-}Pho$) azimuthal correlations with charged hadrons. The background is the photonic electron azimuthal correlations with charged hadrons. In order to extract the e-h azimuthal correlation signal, we start with the semi-inclusive electron sample ($Semi\text{-}Inc$). The inclusive electron sample (Inc) includes all tracks that pass our electron identification cuts. We remove the $OppSign$ sample from the inclusive electron sample. The remaining electrons form the semi-inclusive electron sample. Eq. 4.3 shows the relationship of these samples.

$$\begin{aligned} Semi\text{-}Inc &= Inc - OppSign \\ &= Inc - (Reco\text{-}Pho + SameSign) \\ &= Inc - (Pho - Not\text{-}Reco\text{-}Pho + SameSign) \\ &= Non\text{-}Pho + Not\text{-}Reco\text{-}Pho - SameSign \end{aligned} \tag{4.3}$$

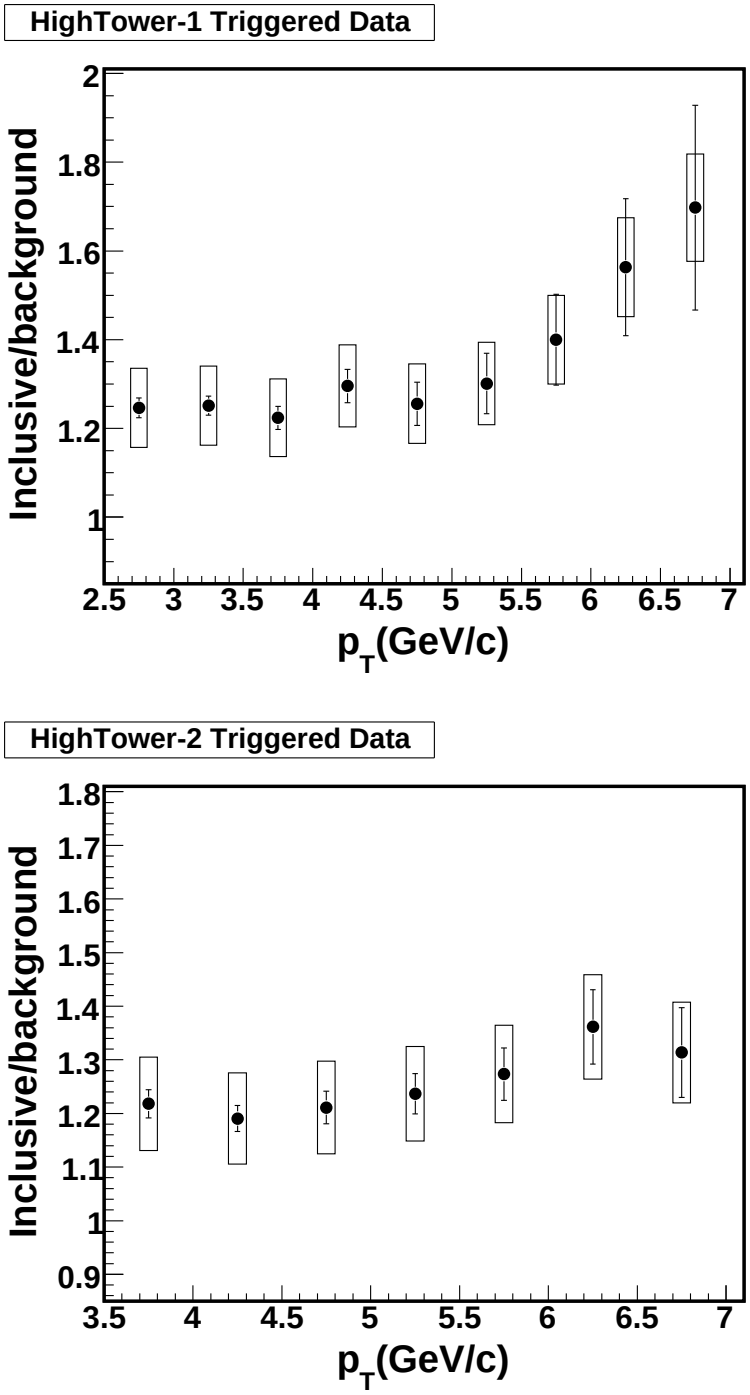

Figure 4.14: The ratio of inclusive electron to photonic background as a function of p_T in Run-5 p+p collisions for HighTower-1 triggered data in upper panel and HighTower-2 triggered data in bottom panel.

where we have used equation 4.1. Therefore the e-h azimuthal correlation signal can be obtained by Eq. 4.4.

$$\Delta\varphi_{Non\text{-}Pho} = \Delta\varphi_{Semi\text{-}Inc} - \Delta\varphi_{Not\text{-}Reco\text{-}Pho} + \Delta\varphi_{SameSign} \tag{4.4}$$

$\Delta\varphi_{Not\text{-}Reco\text{-}Pho}$ can be calculated using $\Delta\varphi_{Reco\text{-}Pho}$ by an efficiency correction after removing the photonic partner of the reconstructed-photonic electron. The photonic background has two parts: reconstructed-photonic electrons and not-reconstructed-photonic electrons. In non-photonic electron yield or v_2 analyses, the not-reconstructed-photonic part can just be calculated by reconstructed-photonic part after an efficiency correction as shown in Eq. 4.5.

$$Not\text{-}Reco\text{-}Pho = (\frac{1}{\varepsilon} - 1) \times Reco\text{-}Pho \tag{4.5}$$

where ε is the photonic electron reconstruction efficiency. However, the situation is different in e-h correlation analysis. For the reconstructed-photonic electron the photonic partner is found while for not-reconstructed-photonic electron the partner is missing. The resulting e-h correlations for reconstructed photonic electrons and not reconstructed photonic electrons are different and cannot be related to each other by multiplicative an efficiency correction factor alone. If we use the reconstructed-photonic azimuthal angular correlation to calculate the not-reconstructed-photonic azimuthal angular correlation, we have to remove the conversion partner of the reconstructed-photonic electron. Therefore $\Delta\varphi_{Not\text{-}Reco\text{-}Pho}$ can be obtained by Eq. 4.6, where ε is the photonic electron reconstruction efficiency and $\Delta\varphi_{Reco\text{-}Pho\text{-}No\text{-}Partner}$ is the reconstructed photonic electron azimuthal correlation with charged hadrons after removing the conversion partner, $\Delta\varphi_{OppSign\text{-}No\text{-}Partner}$ is $OppSign$ electron azimuthal correlation with charged hadrons after removing the conversion partner and $\Delta\varphi_{SameSign\text{-}No\text{-}Partner}$ is $SameSign$ electron azimuthal correlation with charged hadrons after removing the conversion partner.

$$\begin{aligned}\Delta\varphi_{Not\text{-}Reco\text{-}Pho} &= (\frac{1}{\varepsilon} - 1) \times \Delta\varphi_{Reco\text{-}Pho\text{-}No\text{-}Partner} \\ &= (\frac{1}{\varepsilon} - 1) \times (\Delta\varphi_{OppSign\text{-}No\text{-}Partner} - \Delta\varphi_{SameSign\text{-}No\text{-}Partner})\end{aligned} \tag{4.6}$$

The final equation used to extract the e-h azimuthal correlation signal is presented in Eq. 4.7. Each item on the right side of the equation can be directly measured

experimentally, or in the case of ε, calculated using simulations.

$$\begin{aligned}&\Delta\varphi_{Non\text{-}Pho} = \Delta\varphi_{Semi\text{-}Inc} + \Delta\varphi_{SameSign} \\ &-(\frac{1}{\varepsilon} - 1) \times (\Delta\varphi_{OppSign\text{-}No\text{-}Partner} - \Delta\varphi_{SameSign\text{-}No\text{-}Partner})\end{aligned} \tag{4.7}$$

Suppose the number of $\Delta\varphi_{Semi\text{-}Inc}$ counts is $N(\Delta\varphi_{Semi\text{-}Inc})$, then the error is $\sqrt{N(\Delta\varphi_{Semi\text{-}Inc})}$. The same for the other items. The corresponding error of Eq. 4.7 can be obtained from Eq. 4.8.

$$\begin{aligned}&(\delta N(\Delta\varphi_{Non\text{-}Pho}))^2 = (\delta N(\Delta\varphi_{Semi\text{-}Inc}))^2 + (\delta N(\Delta\varphi_{SameSign}))^2 \\ &+(\frac{1}{\varepsilon} - 1)^2 \times (\delta N(\Delta\varphi_{OppSign\text{-}No\text{-}Partner}))^2 \\ &+(\frac{1}{\varepsilon} - 1)^2 \times (\delta N(\Delta\varphi_{SameSign\text{-}No\text{-}Partner}))^2 \\ &= N(\Delta\varphi_{Semi\text{-}Inc}) + N(\Delta\varphi_{SameSign}) \\ &+(\frac{1}{\varepsilon} - 1)^2 \times N(\Delta\varphi_{OppSign\text{-}No\text{-}Partner}) \\ &+(\frac{1}{\varepsilon} - 1)^2 \times N(\Delta\varphi_{SameSign\text{-}No\text{-}Partner})\end{aligned} \tag{4.8}$$

The non-photonic electron azimuthal correlations with charged hadrons can also be calculated by starting with the inclusive electron sample as was done in the determination of non-photonic electron yields and in v_2 analyses. The equation is shown in Eq. 4.9, and the corresponding equation determining the error is shown in Eq. 4.10.

$$\begin{aligned}&\Delta\varphi_{Non\text{-}Pho} = \Delta\varphi_{Inc} - (\Delta\varphi_{Reco\text{-}Pho} + \Delta\varphi_{Not\text{-}Reco\text{-}Pho}) \\ &= \Delta\varphi_{Inc} - (\Delta\varphi_{OppSign} - \Delta\varphi_{SameSign}) \\ &-(\frac{1}{\varepsilon} - 1) \times (\Delta\varphi_{OppSign\text{-}No\text{-}Partner} - \Delta\varphi_{SameSign\text{-}No\text{-}Partner})\end{aligned} \tag{4.9}$$

$$\begin{aligned}&(\delta N(\Delta\varphi_{Non\text{-}Pho}))^2 = N(\Delta\varphi_{Inc}) + N(\Delta\varphi_{OppSign}) + N(\Delta\varphi_{SameSign}) \\ &+(\frac{1}{\varepsilon} - 1)^2 \times N(\Delta\varphi_{OppSign\text{-}No\text{-}Partner}) \\ &+(\frac{1}{\varepsilon} - 1)^2 \times N(\Delta\varphi_{SameSign\text{-}No\text{-}Partner})\end{aligned} \tag{4.10}$$

Comparing Eq. 4.8 to Eq. 4.10, we can clearly see the advantage of the method starting with the semi-inclusive electron sample. The method using the semi-inclusive

electrons starts with a smaller and purer non-photonic electron sample and can often lead to smaller overall uncertainties.

Fig. 4.15 shows the distributions of azimuthal correlations for each item on the right side of Eq. 4.7 used to extract the signal in four electron trigger p_T regions with associated hadron $p_T > 0.3$ GeV/c. The signal of e-h azimuthal correlations, $\Delta\varphi_{Non\text{-}Pho}$, is shown in Fig. 4.16 for four electron trigger p_T cuts with associated hadron $p_T > 0.3$. The distributions are scaled by the number of non-photonic electron triggers. The error bars are statistical only.

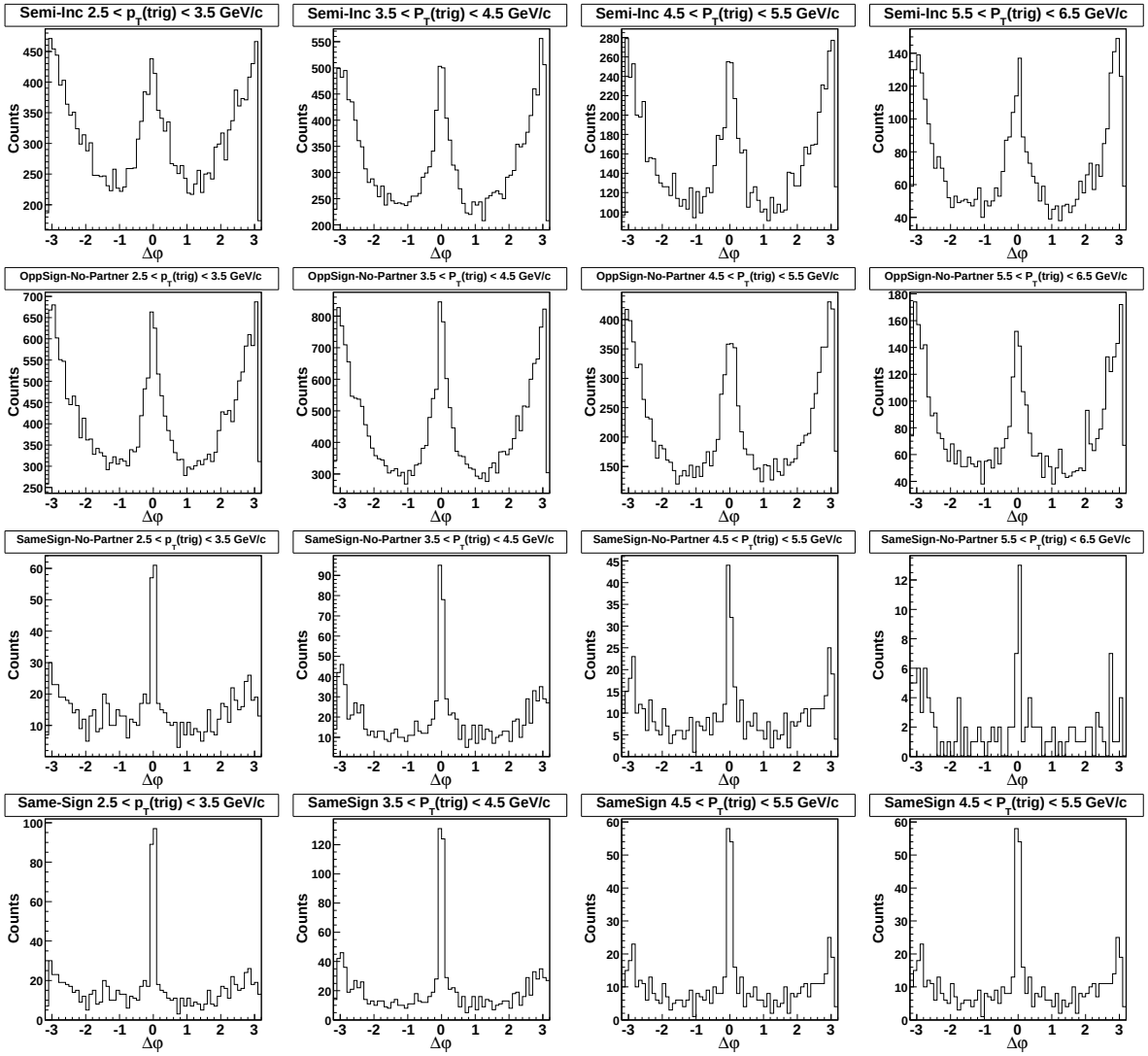

Figure 4.15: The $\Delta\varphi$ distributions for each item on the right side of Eq. 4.7 used to extract the signal in four electron trigger p_T regions with associated hadron $p_T > 0.3$ GeV/c.

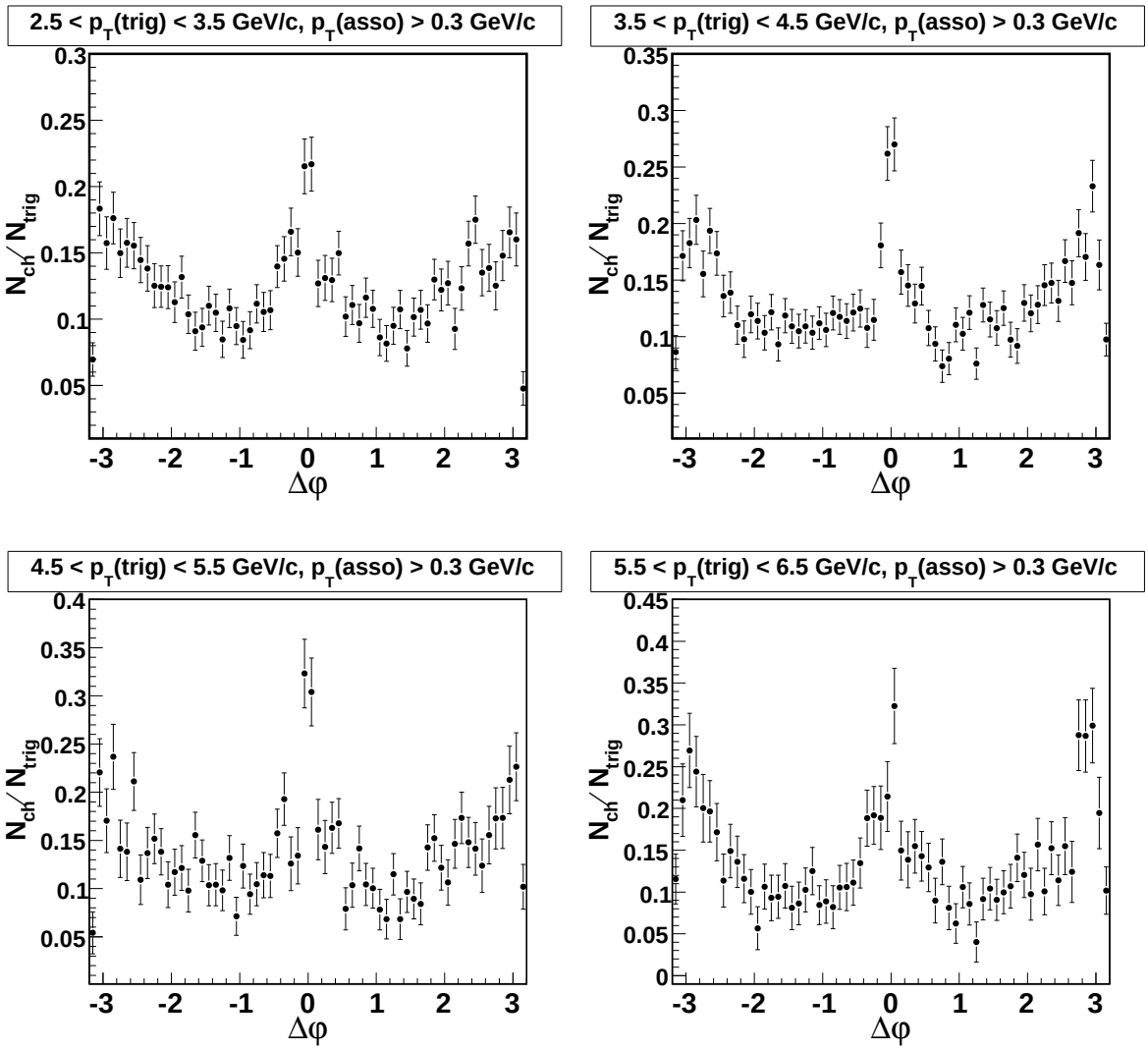

Figure 4.16: The $\Delta\varphi_{Non\text{-}Pho}$ distributions for four electron trigger p_T regions with associated hadron $p_T > 0.3$ GeV/c in p+p collisions at $\sqrt{s_{NN}} = 200$ GeV. The distributions are scaled by the number of non-photonic electron triggers.

CHAPTER 5

Results and Discussion

5.1 Fit Results

Fig. 5.1 shows the $\Delta\varphi_{Non\text{-}Pho}$ distributions in comparison to PYTHIA simulations for four electron trigger cuts with associated hadron $p_T(assoc) > 0.3$ GeV/c. The data are shown as dots, while the blue dashed curves and the red dotted curves are from PYTHIA simulations for B decays and for D decays, respectively. We use PYTHIA curves to fit the data points with the B contribution as a parameter in the fit function:

$$\Delta\varphi_{exp} = R \times \Delta\varphi_B + (1 - R) \times \Delta\varphi_D \tag{5.1}$$

where R is the B contribution, $B/(B + D)$. The fits are shown as green solid curves in Fig. 5.1, with the fit range in $\Delta\varphi$ from -1.5 to $+1.5$.

Fig. 5.2 shows the $B/(B + D)$ ratio as a function of the fit range in $\Delta\varphi$. In Fig. 5.2 factors are used to scale the $B/(B + D)$ ratios of each trigger p_T region so that the data points can be separated well. The fit results are consistent within statistical errors when we vary the fit range in $\Delta\varphi$ from ± 1 to $\pm\pi$. The difference of the $B/(B + D)$ ratio introduced by the variation of the fit range will be one source for the systematic uncertainties of our final result.

As a cross check, we fixed the $B/(B+D)$ ratio to see how the fit χ^2 changes. Fig. 5.3 shows the fit χ^2 as a function of the $B/(B + D)$ ratio with the fit range in $\Delta\varphi$ from -1.5 to $+1.5$. As presented in Fig. 5.3, the χ^2 is sensitive to the $B/(B + D)$ ratio; and a similar sensitivity is seen for other fit ranges.

As a check on systematics, we allowed an overall normalization factor in the fit

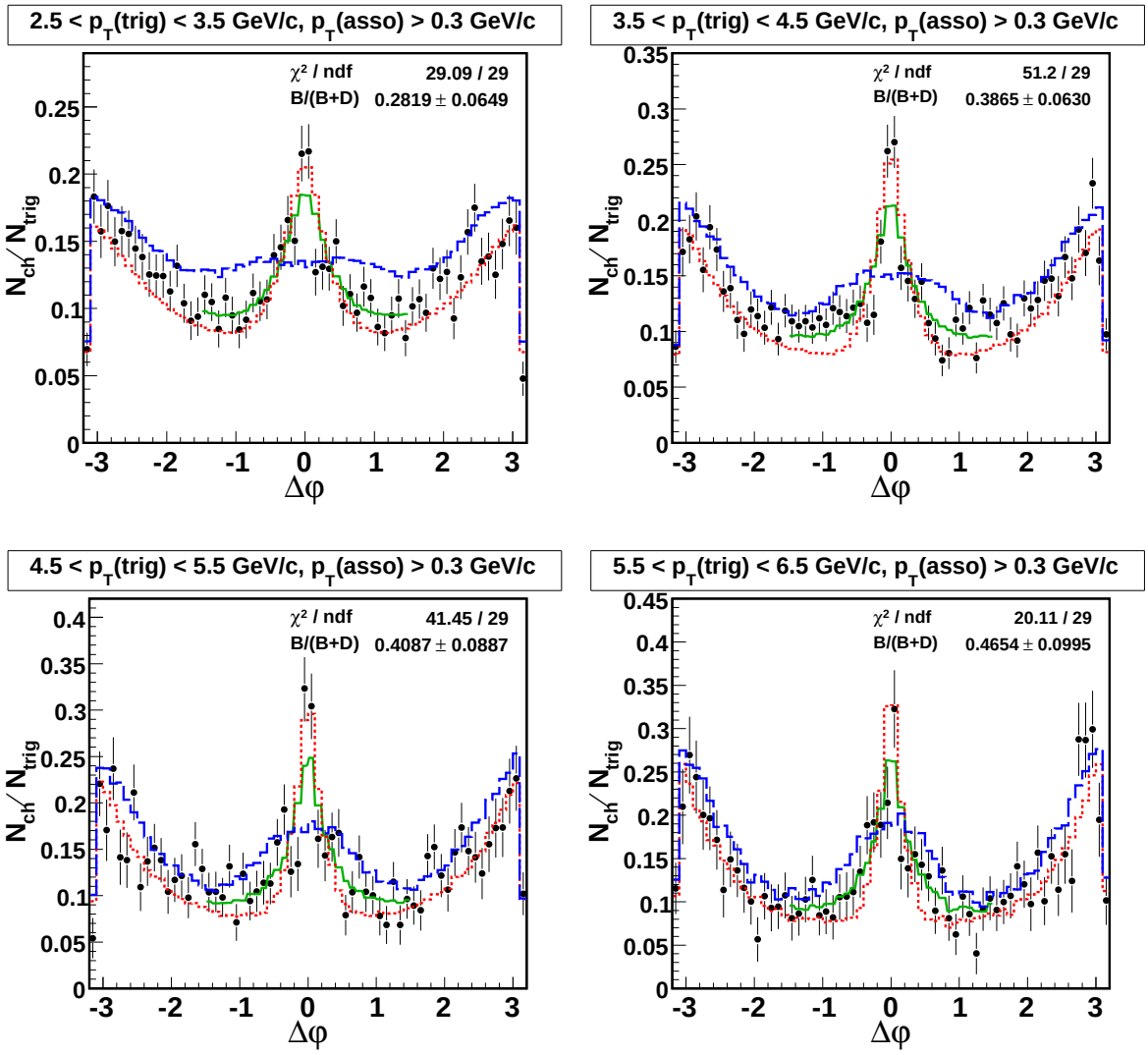

Figure 5.1: The comparisons of $\Delta\varphi_{Non\text{-}Pho}$ distributions to PYTHIA simulations for four electron trigger p_T regions with associated hadron $p_T > 0.3$ GeV/c. The simulations are depicted by blue dashed lines from B meson decays and red dotted lines for D meson decays. The green solid curves are the fits to data points using PYTHIA curves.

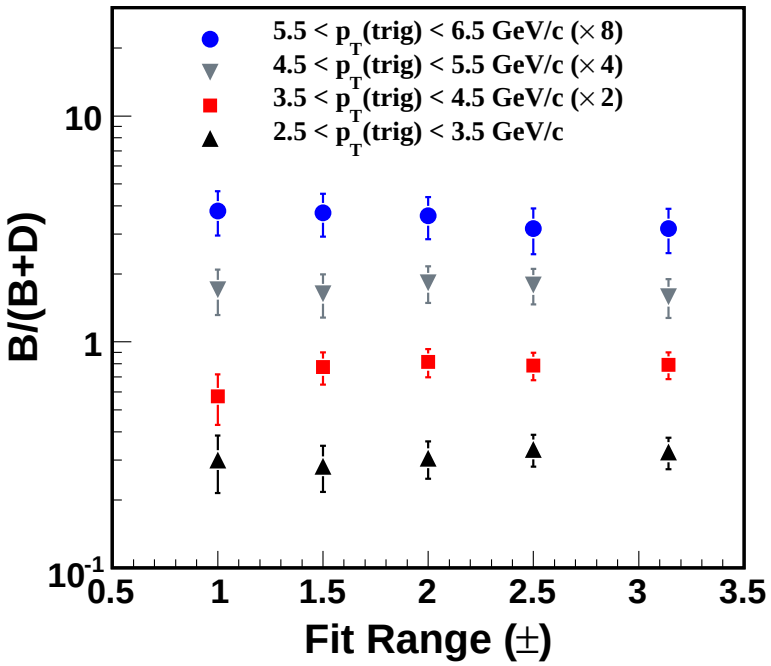

Figure 5.2: The $B/(B+D)$ ratio as a function of the fit range in $\Delta\varphi$. Scaling factors are used in order to separate the data points cleanly.

function to float, i.e.,

$$\Delta\varphi_{exp} = A \times [R \times \Delta\varphi_B + (1-R) \times \Delta\varphi_D] \tag{5.2}$$

where R is the B contribution, $B/(B+D)$, and A is the overall normalization factor. The overall normalization factor A reflects the uncertainties in the normalization which possibly arises from the counting of the number of non-photonic triggers and tracking efficiency for the associated tracks. The fit result gives a normalization factor close to unity; and the $B/(B+D)$ ratios obtained from the fit functions given by equations 5.1 and 5.2 are consistent. We also added an adjustable constant to the fit function, i.e.,

$$\Delta\varphi_{exp} = R \times \Delta\varphi_B + (1-R) \times \Delta\varphi_D + C \tag{5.3}$$

where R is the B contribution, $B/(B+D)$, and C is the added constant. The added constant C freely adjusts the overall background level and it contains soft particle pro-

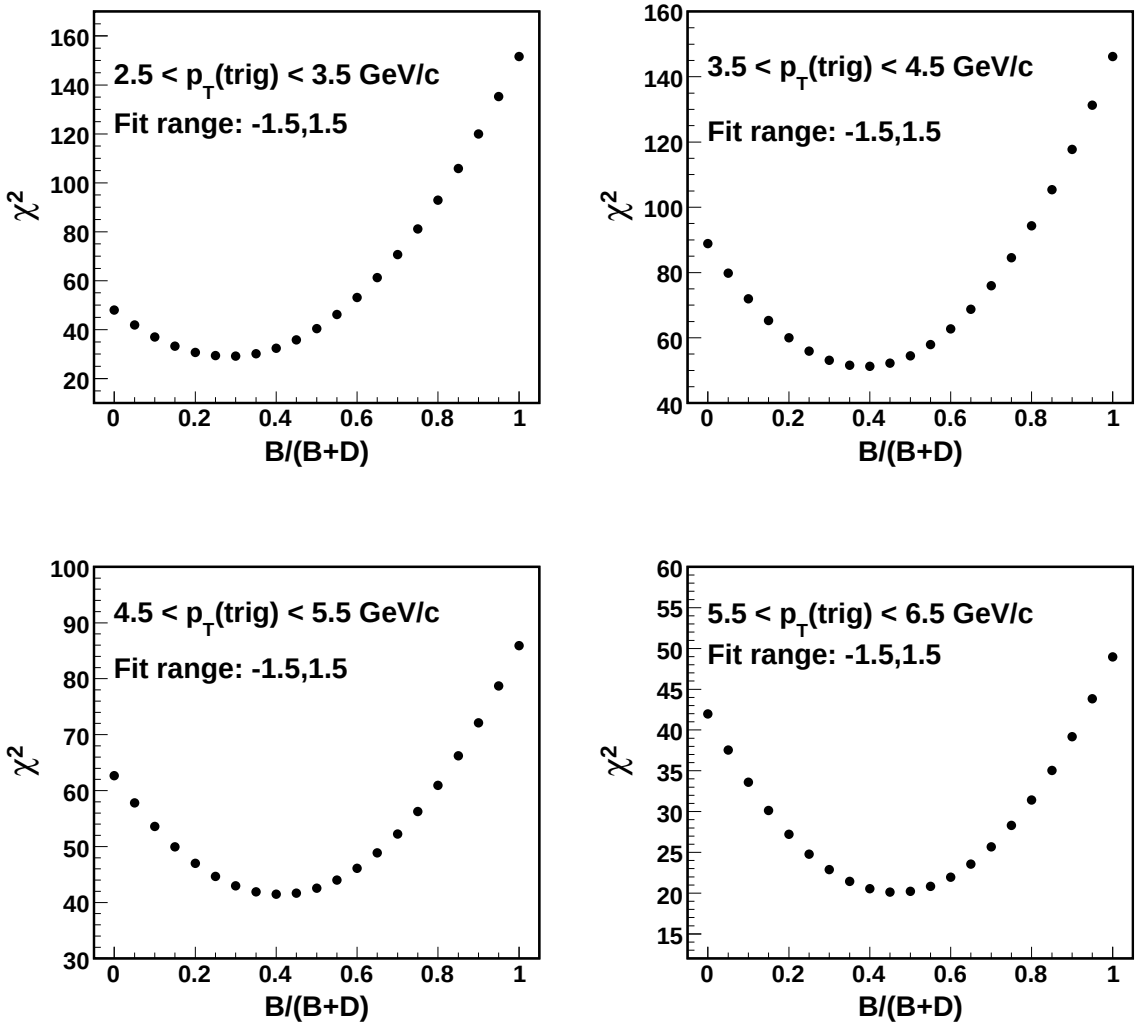

Figure 5.3: The fit χ^2 as a function of the $B/(B+D)$ ratio.

duction. The fit result gives a value for the constant C close to zero, and the $B/(B+D)$ ratios obtained from the fit functions given by equations 5.1, 5.2 and 5.3 are consistent.

These systematic checks show that our approach is not susceptible to large variations beyond our estimate for systematic uncertainties. The PYTHIA Monte Carlo events can reasonably describe the underlying p+p collisions at RHIC. The difference for the B contribution introduced by using different fit functions will be included in the systematic uncertainties of our final result.

5.2 B Semi-Leptonic Decay Contribution to Non-Photonic Electrons

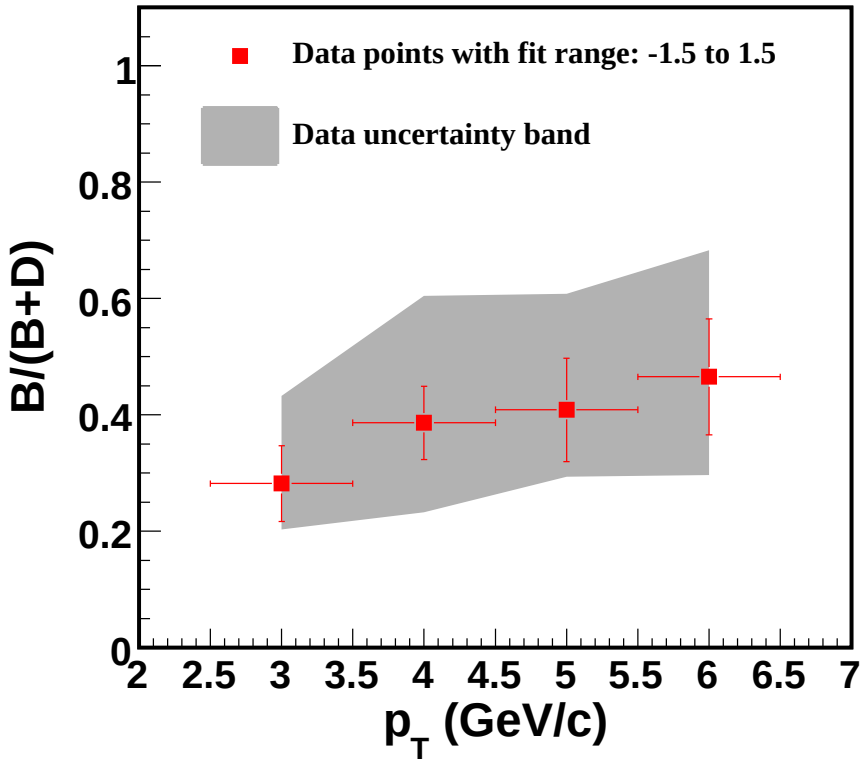

Figure 5.4: The relative B meson semi-leptonic decay contribution to non-photonic electrons as a function of electron p_T.

Our result for the B meson semi-leptonic decay contribution to the yield of non-photonic electrons is shown in Fig. 5.4 as a function of electron p_T. The bars show the size of statistical errors. The grey band indicates the data uncertainties including statistical errors and systematic uncertainties. The sources for systematic uncertainties are listed in the following:

- The uncertainty of the photonic electron reconstruction efficiency, which is the dominant source.
- The difference introduced by the different fit functions.
- The difference introduced by the different fit ranges.

A finite B contribution to the yield of non-photonic electrons in the p_T region of $2.5-6.5$ GeV/c has been measured. Within the current statistical and systematic errors, our measured $B/(B+D)$ ratio indicates that at $p_T \sim 4.0-6.0$ GeV/c the measured B contribution to non-photonic electrons is comparable to the D contribution.

5.3 Comparison with FONLL pQCD Calculation

Fig. 5.5 shows the comparison of the measured $B/(B+D)$ ratios to the FONLL pQCD calculations [CNV05]. The blue solid curves show the range of relative bottom contribution from the FONLL calculations, with the variation due to NLO uncertainties of quark mass, factorization scale μ_F, renormalization scale μ_R, parton density function (PDF) and fragmentation functions (FF), etc. The dashed line is the $B/(B+D)$ ratio in FONLL used for the default non-photonic electron R_{AA} calculation. The FONLL theoretical calculations are consistent with our measured $B/(B+D)$ ratios within uncertainties.

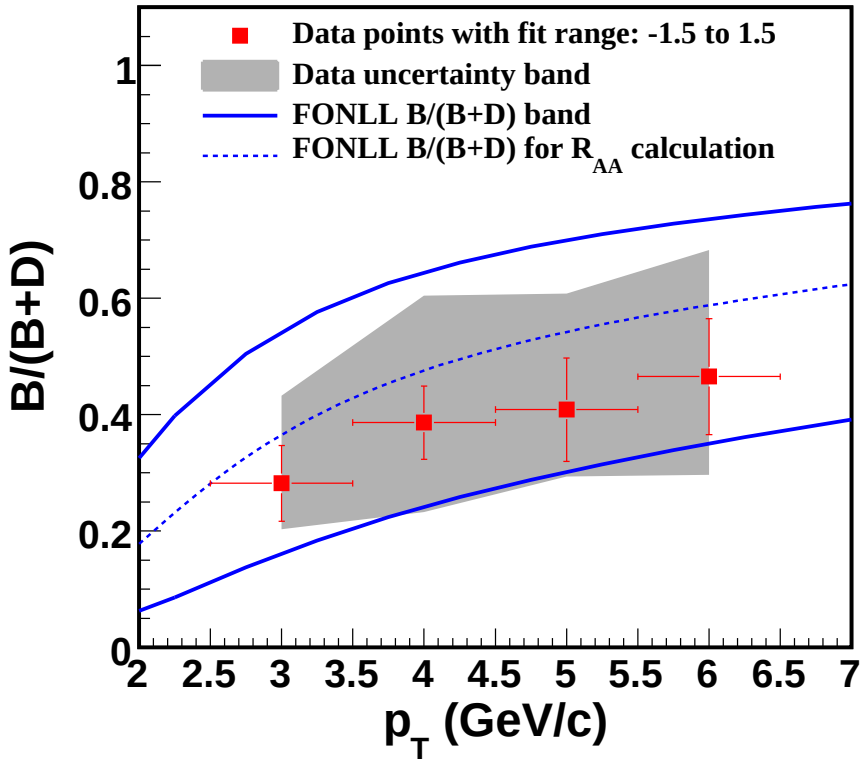

Figure 5.5: The measured $B/(B+D)$ ratios in comparison with the FONLL pQCD calculations.

5.4 Discussion

5.4.1 Bottom Suppression

Fig. 5.6 shows the partonic level jet quenching of heavy quark and the corresponding heavy quark decayed non-photonic electron quenching from the DGLV theory of radiative energy loss [DGV06]. Due to the color Casimir factor, and small in-medium mass, gluon quenching is the largest effect. The dead cone effect [DK01] can be seen between charm quark and light quark quenching at $p_T < 10$ GeV/c. Above 10 GeV/c, the mass difference between charm quark and light quarks will be almost negligible since $p_T > 10$ GeV/c $>> m_c$. Because of the large mass of bottom quark, even for p_T up to 20 GeV/c,

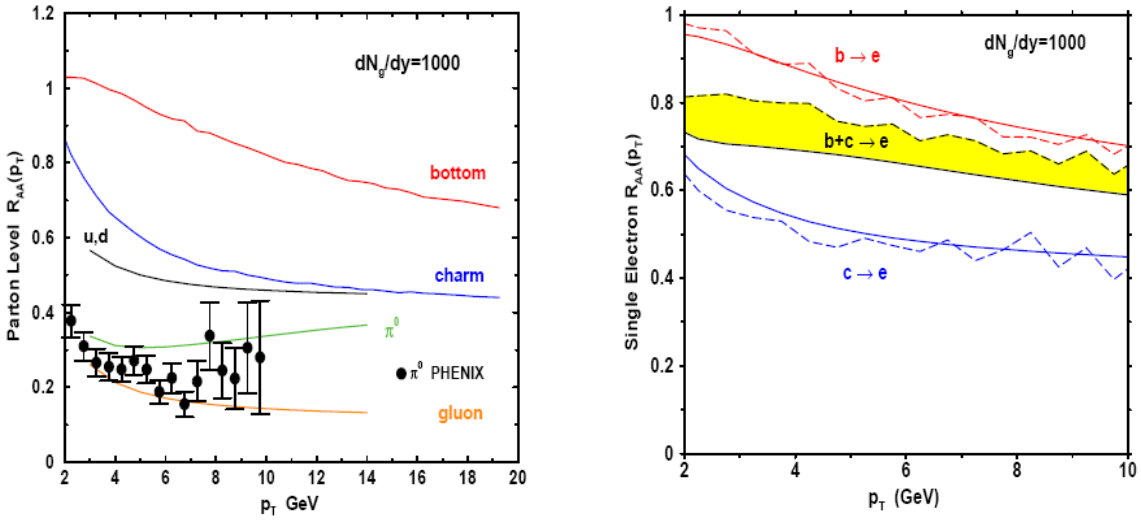

Figure 5.6: Left: The partonic level jet quenching of charm quark and bottom quark in comparison with light quark (u, d) and gluon quenching from the DGLV theory of radiative energy loss. Right: The corresponding R_{AA} for the non-photonic electrons from heavy quarks. Figures taken from [DGV06].

p_T/m_b is not large; the bottom quark is significantly less quenched than the charm quark and light quarks for $p_T < 20$ GeV/c. This reduced bottom quenching strongly limits the corresponding quenching for bottom decay electrons as shown in the right panel of Fig. 5.6.

We have provided the first measurement for the contribution from B semi-leptonic decays to non-photonic electron yields in p+p collisions at RHIC. Together with the observation in Au+Au collisions at high p_T of a large suppression of non-photonic electrons and a tendency for the non-photonic v_2 to decrease as p_T increases, our measured $B/(B+D)$ ratios imply that the bottom quark may be suppressed in central Au+Au collisions at RHIC, which is in contrast to the prediction from the DGLV theory of radiative energy loss.

A recent theoretical calculation, taking into account the short formation times of D and B mesons, found that the suppression of non-photonic electrons from heavy mesons,

including B mesons, is compatible with the measured large quenching for heavy flavor. This calculation predicts that the suppression of B mesons is comparable to that of D mesons at transverse momentum as low as $p_T \sim 10$ GeV/c [AV06].

5.4.2 Low Material RUN at STAR

In the heavy ion collision environment, a large number of π^0 will be created, leading to a large amount of decay photons. Those photons will convert into electron-positron pairs when interacting with materials. In the STAR detector system, there is considerable material surrounding the collision region, including beam pipe, SVT, Silicon Strip Detetor (SSD), Inner Field Cage (IFC), and the TPC gas. The large photonic background is the most important source that contributes to the large uncertainties in STAR non-photonic electron measurements. Studies have shown that if the SVT is removed, the probability for photon conversion will decrease by a factor of 4 [Don06]. STAR is going to have a low material run within the next year or so; that is, a run where the present STAR inner tracking detectors (SVT and SSD) are removed. This will significantly improve the signal to background ratio.

5.4.3 Vertex Detector Upgrade at STAR

The STAR experiment has been developing a vertex detector upgrade — the Heavy Flavor Tracker (HFT) [Xu06]. The HFT will replace the existing STAR SVT and sit inside the the STAR Time Projection Chamber. It will cover ± 1.0 units in pseudorapidity and 20 cm in length for collisions at the center of the colliding region. The HFT will use active pixel sensor technology for the detector elements and have two tracking layers at radii 1.5 cm and 5.0 cm, covering the full azimuth. The high precision ($< 10\mu m$ vertex resolution) measurements of the vertex position will allow us to reconstruct open charm and bottom hadrons directly and cleanly. With the help of the HFT the precise measurements of total cross section of heavy flavor production, heavy flavor energy loss, heavy flavor azimuthal anisotropy and the correlation measurements for heavy flavored mesons, etc will be feasible. The open questions in current heavy flavor measurements

at RHIC will then be resolved without ambiguity.

The STAR HFT upgrade is expected to be ready to take data in year 2010. The completion of the program will yield more beautiful data at RHIC which will provide an insightful probe of the QGP properties and shed more light on the QCD production of heavy quarks at RHIC.

APPENDIX A

Kinematic Variables

In relativistic heavy ion collisions, it is convenient to use kinematic variables that are Lorentz invariant or transform trivially under Lorentz boost.

The transverse momentum p_T is defined by using the momentum transverse components p_x and p_y

$$p_T = \sqrt{p_x^2 + p_y^2}. \tag{A.1}$$

p_T is a Lorentz invariant variable under a Lorentz boost along the z axis, i.e., the direction of the beam.

The transverse mass for a particle with mass m_0 is defined by

$$m_T = \sqrt{p_T^2 + m_0^2}. \tag{A.2}$$

The transverse kinetic energy of a particle is given by $m_T - m_0$.

The rapidity (y) of a particle, a dimensionless quantity, is defined by

$$y = \frac{1}{2} \ln \left(\frac{E + p_z}{E - p_z} \right), \tag{A.3}$$

where $E = \sqrt{p^2 + m_0^2}$ is the total energy of the particle. The rapidity of a particle is Lorentz boost invariant. It is additive by a constant under Lorentz transformations.

In high energy experiment, it is common to have $|\vec{p}| \approx E$. Then

$$y = \frac{1}{2} \ln \left(\frac{E + p_z}{E - p_z} \right) \approx \frac{1}{2} \ln \left(\frac{|\vec{p}| + p_z}{|\vec{p}| - p_z} \right) = \ln \left(\sqrt{\frac{1 + \cos\theta}{1 - \cos\theta}} \right) = -\ln[\tan(\theta/2)] \equiv \eta, \tag{A.4}$$

where θ is the angle between the particle momentum and the beam axis, and η is called pseudorapidity. The pseudorapidity (η) of a particle is used to characterize the emission

of the particle with respect to the beam direction. Note that the pseudorapidity, unlike the rapidity, can be calculated without knowing the mass of the particle .

APPENDIX B

The STAR Collaboration

B.I. Abelev,[50] J. Adams,[2] M.M. Aggarwal,[30] Z. Ahammed,[45] J. Amonett,[20] B.D. Anderson,[20] M. Anderson,[6] D. Arkhipkin,[13] G.S. Averichev,[12] Y. Bai,[28] J. Balewski,[17] O. Barannikova,[9] L.S. Barnby,[2] J. Baudot,[18] S. Bekele,[29] V.V. Belaga,[12] A. Bellingeri-Laurikainen,[40] R. Bellwied,[48] F. Benedosso,[28] S. Bhardwaj,[35] A. Bhasin,[19] A.K. Bhati,[30] H. Bichsel,[47] J. Bielcik,[50] J. Bielcikova,[50] L.C. Bland,[3] S-L. Blyth,[22] B.E. Bonner,[36] M. Botje,[28] J. Bouchet,[40] A.V. Brandin,[26] A. Bravar,[3] M. Bystersky,[11] R.V. Cadman,[1] X.Z. Cai,[39] H. Caines,[50] M. Calderón de la Barca Sánchez,[6] J. Castillo,[28] O. Catu,[50] D. Cebra,[6] Z. Chajecki,[29] P. Chaloupka,[11] S. Chattopadhyay,[45] H.F. Chen,[38] J.H. Chen,[39] J. Cheng,[43] M. Cherney,[10] A. Chikanian,[50] W. Christie,[3] J.P. Coffin,[18] T.M. Cormier,[48] M.R. Cosentino,[37] J.G. Cramer,[47] H.J. Crawford,[5] D. Das,[45] S. Das,[45] M. Daugherity,[42] M.M. de Moura,[37] T.G. Dedovich,[12] M. DePhillips,[3] A.A. Derevschikov,[32] L. Didenko,[3] T. Dietel,[14] P. Djawotho,[17] S.M. Dogra,[19] W.J. Dong,[7] X. Dong,[38] J.E. Draper,[6] F. Du,[50] V.B. Dunin,[12] J.C. Dunlop,[3] M.R. Dutta Mazumdar,[45] V. Eckardt,[24] W.R. Edwards,[22] L.G. Efimov,[12] V. Emelianov,[26] J. Engelage,[5] G. Eppley,[36] B. Erazmus,[40] M. Estienne,[18] P. Fachini,[3] R. Fatemi,[23] J. Fedorisin,[12] K. Filimonov,[22] P. Filip,[13] E. Finch,[50] V. Fine,[3] Y. Fisyak,[3] J. Fu,[49] C.A. Gagliardi,[41] L. Gaillard,[2] M.S. Ganti,[45] V. Ghazikhanian,[7] P. Ghosh,[45] J.E. Gonzalez,[7] Y.G. Gorbunov,[10] H. Gos,[46] O. Grebenyuk,[28] D. Grosnick,[44] S.M. Guertin,[7] K.S.F.F. Guimaraes,[37] Y. Guo,[48] N. Gupta,[19] T.D. Gutierrez,[6] B. Haag,[6] T.J. Hallman,[3] A. Hamed,[48] J.W. Harris,[50] W. He,[17] M. Heinz,[50] T.W. Henry,[41] S. Hepplemann,[31] B. Hippolyte,[18] A. Hirsch,[33] E. Hjort,[22] G.W. Hoffmann,[42] M.J. Horner,[22] H.Z. Huang,[7] S.L. Huang,[38] E.W. Hughes,[4] T.J. Humanic,[29] G. Igo,[7] P. Jacobs,[22] W.W. Jacobs,[17] P. Jakl,[11] F. Jia,[21] H. Jiang,[7] P.G. Jones,[2] E.G. Judd,[5] S. Kabana,[40] K. Kang,[43] J. Kapitan,[11] M. Kaplan,[8] D. Keane,[20] A. Kechechyan,[12] V.Yu. Khodyrev,[32] B.C. Kim,[34] J. Kiryluk,[23] A. Kisiel,[46] E.M. Kislov,[12] S.R. Klein,[22] D.D. Koetke,[44] T. Kollegger,[14] M. Kopytine,[20] L. Kotchenda,[26] V. Kouchpil,[11] K.L. Kowalik,[22] M. Kramer,[27] P. Kravtsov,[26] V.I. Kravtsov,[32] K. Krueger,[1] C. Kuhn,[18] A.I. Kulikov,[12] A. Kumar,[30] A.A. Kuznetsov,[12] M.A.C. Lamont,[50] J.M. Landgraf,[3] S. Lange,[14] S. LaPointe,[48] F. Laue,[3] J. Lauret,[3] A. Lebedev,[3] R. Lednicky,[13] C-H. Lee,[34] S. Lehocka,[12] M.J. LeVine,[3] C. Li,[38] Q. Li,[48] Y. Li,[43] G. Lin,[50] X. Lin,[49] S.J. Lindenbaum,[27] M.A. Lisa,[29] F. Liu,[49] H. Liu,[38] J. Liu,[36] L. Liu,[49] Z. Liu,[49] T. Ljubicic,[3] W.J. Llope,[36] H. Long,[7] R.S. Longacre,[3] M. Lopez-Noriega,[29] W.A. Love,[3] Y. Lu,[49] T. Ludlam,[3] D. Lynn,[3] G.L. Ma,[39] J.G. Ma,[7] Y.G. Ma,[39] D. Magestro,[29] D.P. Mahapatra,[15] R. Majka,[50] L.K. Mangotra,[19] R. Manweiler,[44] S. Margetis,[20] C. Markert,[42] L. Martin,[40] H.S. Matis,[22] Yu.A. Matulenko,[32] C.J. McClain,[1] T.S. McShane,[10] Yu. Melnick,[32] A. Meschanin,[32] M.L. Miller,[23] N.G. Minaev,[32] S. Mioduszewski,[41] C. Mironov,[20] A. Mischke,[28] D.K. Mishra,[15] J. Mitchell,[36] B. Mohanty,[45] L. Molnar,[33] C.F. Moore,[42] D.A. Morozov,[32] M.G. Munhoz,[37] B.K. Nandi,[16] C. Nattrass,[50] T.K. Nayak,[45] J.M. Nelson,[2] P.K. Netrakanti,[45] V.A. Nikitin,[13] L.V. Nogach,[32] S.B. Nurushev,[32] G. Odyniec,[22] A. Ogawa,[3] V. Okorokov,[26] M. Oldenburg,[22] D. Olson,[22] M. Pachr,[11] S.K. Pal,[45] Y. Panebratsev,[12] S.Y. Panitkin,[3] A.I. Pavlinov,[48] T. Pawlak,[46] T. Peitzmann,[28] V. Perevoztchikov,[3] C. Perkins,[5] W. Peryt,[46] V.A. Petrov,[48] S.C. Phatak,[15] R. Picha,[6] M. Planinic,[51] J. Pluta,[46] N. Poljak,[51] N. Porile,[33] J. Porter,[47] A.M. Poskanzer,[22] M. Potekhin,[3] E. Potrebenikova,[12] B.V.K.S. Potukuchi,[19] D. Prindle,[47] C. Pruneau,[48] J. Putschke,[22] G. Rakness,[31] R. Raniwala,[35] S. Raniwala,[35] R.L. Ray,[42] S.V. Razin,[12] J. Reinnarth,[40] D. Relyea,[4] F. Retiere,[22] A. Ridiger,[26] H.G. Ritter,[22] J.B. Roberts,[36] O.V. Rogachevskiy,[12] J.L. Romero,[6] A. Rose,[22] C. Roy,[40] L. Ruan,[22] M.J. Russcher,[28] R. Sahoo,[15] S. Salur,[50] J. Sandweiss,[50] M. Sarsour,[41] P.S. Sazhin,[12] J. Schambach,[42] R.P. Scharenberg,[33] N. Schmitz,[24] K. Schweda,[22] J. Seger,[10] I. Selyuzhenkov,[48] P. Seyboth,[24] A. Shabetai,[22] E. Shahaliev,[12] M. Shao,[38] M. Sharma,[30] W.Q. Shen,[39] S.S. Shimanskiy,[12] E Sichtermann,[22] F. Simon,[23] R.N. Singaraju,[45] N. Smirnov,[50] R. Snellings,[28] G. Sood,[44] P. Sorensen,[3] J. Sowinski,[17] J. Speltz,[18] H.M. Spinka,[1] B. Srivastava,[33] A. Stadnik,[12] T.D.S. Stanislaus,[44] R. Stock,[14] A. Stolpovsky,[48] M. Strikhanov,[26] B. Stringfellow,[33] A.A.P. Suaide,[37] E. Sugarbaker,[29] M. Sumbera,[11] Z. Sun,[21] B. Surrow,[23] M. Swanger,[10] T.J.M. Symons,[22] A. Szanto de Toledo,[37] A. Tai,[7] J. Takahashi,[37] A.H. Tang,[3] T. Tarnowsky,[33] D. Thein,[7] J.H. Thomas,[22] A.R. Timmins,[2] S. Timoshenko,[26] M. Tokarev,[12] T.A. Trainor,[47] S. Trentalange,[7] R.E. Tribble,[41] O.D. Tsai,[7] J. Ulery,[33] T. Ullrich,[3] D.G. Underwood,[1] G. Van Buren,[3] N. van der Kolk,[28] M. van Leeuwen,[22] A.M. Vander Molen,[25] R. Varma,[16] I.M. Vasilevski,[13] A.N. Vasiliev,[32] R. Vernet,[18] S.E. Vigdor,[17] Y.P. Viyogi,[15] S. Vokal,[12] S.A. Voloshin,[48] W.T. Waggoner,[10] F. Wang,[33] G. Wang,[7] J.S. Wang,[21] X.L. Wang,[38] Y. Wang,[43] J.W. Watson,[20] J.C. Webb,[44] G.D. Westfall,[25]

A. Wetzler,[22] C. Whitten Jr.,[7] H. Wieman,[22] S.W. Wissink,[17] R. Witt,[50] J. Wood,[7] J. Wu,[38] N. Xu,[22] Q.H. Xu Z. Xu,[3] P. Yepes,[36] I-K. Yoo,[34] V.I. Yurevich,[12] W. Zhan,[21] H. Zhang,[3] W.M. Zhang,[20] Y. Zhang,[38] Z.P. Zhang,[38] Y. Zhao,[38] C. Zhong,[39] R. Zoulkarneev,[13] Y. Zoulkarneeva,[13] A.N. Zubarev,[12] and J.X. Zuo[39]

(STAR Collaboration)

[1]*Argonne National Laboratory, Argonne, Illinois 60439*
[2]*University of Birmingham, Birmingham, United Kingdom*
[3]*Brookhaven National Laboratory, Upton, New York 11973*
[4]*California Institute of Technology, Pasadena, California 91125*
[5]*University of California, Berkeley, California 94720*
[6]*University of California, Davis, California 95616*
[7]*University of California, Los Angeles, California 90095*
[8]*Carnegie Mellon University, Pittsburgh, Pennsylvania 15213*
[9]*University of Illinois, Chicago*
[10]*Creighton University, Omaha, Nebraska 68178*
[11]*Nuclear Physics Institute AS CR, 250 68 Řež/Prague, Czech Republic*
[12]*Laboratory for High Energy (JINR), Dubna, Russia*
[13]*Particle Physics Laboratory (JINR), Dubna, Russia*
[14]*University of Frankfurt, Frankfurt, Germany*
[15]*Institute of Physics, Bhubaneswar 751005, India*
[16]*Indian Institute of Technology, Mumbai, India*
[17]*Indiana University, Bloomington, Indiana 47408*
[18]*Institut de Recherches Subatomiques, Strasbourg, France*
[19]*University of Jammu, Jammu 180001, India*
[20]*Kent State University, Kent, Ohio 44242*
[21]*Institute of Modern Physics, Lanzhou, China*
[22]*Lawrence Berkeley National Laboratory, Berkeley, California 94720*
[23]*Massachusetts Institute of Technology, Cambridge, MA 02139-4307*
[24]*Max-Planck-Institut für Physik, Munich, Germany*
[25]*Michigan State University, East Lansing, Michigan 48824*
[26]*Moscow Engineering Physics Institute, Moscow Russia*
[27]*City College of New York, New York City, New York 10031*
[28]*NIKHEF and Utrecht University, Amsterdam, The Netherlands*
[29]*Ohio State University, Columbus, Ohio 43210*
[30]*Panjab University, Chandigarh 160014, India*
[31]*Pennsylvania State University, University Park, Pennsylvania 16802*
[32]*Institute of High Energy Physics, Protvino, Russia*
[33]*Purdue University, West Lafayette, Indiana 47907*
[34]*Pusan National University, Pusan, Republic of Korea*
[35]*University of Rajasthan, Jaipur 302004, India*
[36]*Rice University, Houston, Texas 77251*
[37]*Universidade de Sao Paulo, Sao Paulo, Brazil*
[38]*University of Science & Technology of China, Hefei 230026, China*
[39]*Shanghai Institute of Applied Physics, Shanghai 201800, China*
[40]*SUBATECH, Nantes, France*
[41]*Texas A&M University, College Station, Texas 77843*
[42]*University of Texas, Austin, Texas 78712*
[43]*Tsinghua University, Beijing 100084, China*
[44]*Valparaiso University, Valparaiso, Indiana 46383*
[45]*Variable Energy Cyclotron Centre, Kolkata 700064, India*
[46]*Warsaw University of Technology, Warsaw, Poland*
[47]*University of Washington, Seattle, Washington 98195*
[48]*Wayne State University, Detroit, Michigan 48201*
[49]*Institute of Particle Physics, CCNU (HZNU), Wuhan 430079, China*
[50]*Yale University, New Haven, Connecticut 06520*
[51]*University of Zagreb, Zagreb, HR-10002, Croatia*

References

[Abe06a] B. I. Abelev et al. "Identified baryon and meson distributions at large transverse momenta from Au + Au collisions at s(NN)**(1/2) = 200-GeV." *Phys. Rev. Lett.*, **97**:152301, 2006. nucl-ex/0606003.

[Abe06b] B. I. Abelev et al. "Transverse momentum and centrality dependence of high-p(T) non-photonic electron suppression in Au + Au collisions at s(NN)**(1/2) = 200-GeV." 2006. nucl-ex/0607012.

[Abr00] P. Abreu et al. "Identified Charged Particles in Quark and Gluon Jets." *Eur. Phys. J.*, **C17**:207–222, 2000. hep-ex/0106063.

[ACD06] Nestor Armesto, Matteo Cacciari, Andrea Dainese, Carlos A. Salgado, and Urs Achim Wiedemann. "How sensitive are high-p(T) electron spectra at RHIC to heavy quark energy loss?" *Phys. Lett.*, **B637**:362–366, 2006. hep-ph/0511257.

[Ack03] K. H. Ackermann et al. "STAR detector overview." *Nucl. Instrum. Meth.*, **A499**:624–632, 2003.

[Ada97] M. Adamovich et al. "Measurements of charmed meson production in interactions between 350-GeV/c pi- particles and nuclei." *Nucl. Phys.*, **B495**:3–34, 1997.

[Ada03] John Adams et al. "Transverse momentum and collision energy dependence of high p(T) hadron suppression in Au + Au collisions at ultrarelativistic energies." *Phys. Rev. Lett.*, **91**:172302, 2003. nucl-ex/0305015.

[Ada04] John Adams et al. "Particle dependence of azimuthal anisotropy and nuclear modification of particle production at moderate p(T) in Au + Au collisions at s(NN)**(1/2) = 200-GeV." *Phys. Rev. Lett.*, **92**:052302, 2004. nucl-ex/0306007.

[Ada05a] John Adams et al. "Experimental and theoretical challenges in the search for the quark gluon plasma: The STAR collaboration's critical assessment of the evidence from RHIC collisions." *Nucl. Phys.*, **A757**:102–183, 2005. nucl-ex/0501009.

[Ada05b] John Adams et al. "Open charm yields in d + Au collisions at s(NN)**(1/2) = 200-GeV." *Phys. Rev. Lett.*, **94**:062301, 2005. nucl-ex/0407006.

[Ada06a] A. Adare et al. "Energy loss and flow of heavy quarks in Au + Au collisions at s(NN)**(1/2) = 200-GeV." 2006. nucl-ex/0611018.

[Ada06b] A. Adare et al. "Measurement of high-p(T) single electrons from heavy-flavor decays in p + p collisions at s**(1/2) = 200-GeV." *Phys. Rev. Lett.*, **97**:252002, 2006. hep-ex/0609010.

[Adc02] K. Adcox et al. "Measurement of single electrons and implications for charm production in Au + Au collisions at s(NN)**(1/2) = 130- GeV." *Phys. Rev. Lett.*, **88**:192303, 2002. nucl-ex/0202002.

[Adl03a] S. S. Adler et al. "Elliptic flow of identified hadrons in Au + Au collisions at s(NN)**(1/2) = 200-GeV." *Phys. Rev. Lett.*, **91**:182301, 2003. nucl-ex/0305013.

[Adl03b] S. S. Adler et al. "Scaling properties of proton and anti-proton production in s(NN)**(1/2) = 200-GeV Au + Au collisions." *Phys. Rev. Lett.*, **91**:172301, 2003. nucl-ex/0305036.

[Adl06a] S. S. Adler et al. "Common suppression pattern of eta and pi0 mesons at high transverse momentum in Au + Au collisions at s(NN)**(1/2) = 200-GeV." *Phys. Rev. Lett.*, **96**:202301, 2006. nucl-ex/0601037.

[Adl06b] S. S. Adler et al. "Nuclear modification of electron spectra and implications for heavy quark energy loss in Au + Au collisions at s(NN)**(1/2) = 200-GeV." *Phys. Rev. Lett.*, **96**:032301, 2006. nucl-ex/0510047.

[ADS05] Nestor Armesto, Andrea Dainese, Carlos A. Salgado, and Urs Achim Wiedemann. "Testing the color charge and mass dependence of parton energy loss with heavy-to-light ratios at RHIC and LHC." *Phys. Rev.*, **D71**:054027, 2005. hep-ph/0501225.

[AG04] Azfar Adil and Miklos Gyulassy. "Energy systematics of jet tomography at RHIC: s**(1/2) = 62.4-AGeV vs 200-AGeV." *Phys. Lett.*, **B602**:52–59, 2004. nucl-th/0405036.

[Alv96] G. A. Alves et al. "Feynman-x and transverse momentum dependence of D meson production in 250-GeV pi, K and p nucleon interactions." *Phys. Rev. Lett.*, **77**:2392–2395, 1996.

[And03] M. Anderson et al. "The STAR time projection chamber: A unique tool for studying high multiplicity events at RHIC." *Nucl. Instrum. Meth.*, **A499**:659–678, 2003. nucl-ex/0301015.

[AV06] Azfar Adil and Ivan Vitev. "Collisional dissociation of heavy mesons in dense QCD matter." 2006. hep-ph/0611109.

[Bau75] H. G. Baumgardt et al. "SHOCK WAVES AND MACH CONES IN FAST NUCLEUS-NUCLEUS COLLISIONS." *Z. Phys.*, **A273**:359–371, 1975.

[Bed03] M. Beddo et al. "The STAR barrel electromagnetic calorimeter." *Nucl. Instrum. Meth.*, **A499**:725–739, 2003.

[Bet03] Siegfried Bethke. "alpha(s) 2002." *Nucl. Phys. Proc. Suppl.*, **121**:74–81, 2003. hep-ex/0211012.

[Bie03] F. S. Bieser et al. "The STAR trigger." *Nucl. Instrum. Meth.*, **A499**:766–777, 2003.

[Bjo82] J. D. Bjorken. "Energy Loss of Energetic Partons in Quark - Gluon Plasma: Possible Extinction of High p(t) Jets in Hadron - Hadron Collisions." 1982. FERMILAB-PUB-82-059-THY.

[BKG03] S. Batsouli, S. Kelly, M. Gyulassy, and J. L. Nagle. "Does the charm flow at RHIC?" *Phys. Lett.*, **B557**:26–32, 2003. nucl-th/0212068.

[Bla06] J. P. Blaizot. "Ultrarelativistic heavy ion collisions: Theoretical overview." *J. Phys. Conf. Ser.*, **50**:1–7, 2006.

[BR93] W. Blum and Gigi Rolandi. "Particle detection with drift chambers." 1993. Berlin, Germany: Springer 348 p.

[BSZ00] R. Baier, D. Schiff, and B. G. Zakharov. "Energy loss in perturbative QCD." *Ann. Rev. Nucl. Part. Sci.*, **50**:37–69, 2000. hep-ph/0002198.

[CNV05] Matteo Cacciari, Paolo Nason, and Ramona Vogt. "QCD predictions for charm and bottom production at RHIC." *Phys. Rev. Lett.*, **95**:122001, 2005. hep-ph/0502203.

[CP75a] N. Cabibbo and G. Parisi. "EXPONENTIAL HADRONIC SPECTRUM AND QUARK LIBERATION." *Phys. Lett.*, **B59**:67, 1975.

[CP75b] John C. Collins and M. J. Perry. "SUPERDENSE MATTER: NEUTRONS OR ASYMPTOTICALLY FREE QUARKS?" *Phys. Rev. Lett.*, **34**:1353, 1975.

[CPR02] T. M. Cormier, A. I. Pavlinov, M. V. Rykov, V. L. Rykov, and K. E. Shestermanov. "STAR Barrel Electromagnetic Calorimeter absolute calibration using 'minimum ionizing particles' from collisions at RHIC." *Nucl. Instrum. Meth.*, **A483**:734–746, 2002. hep-ex/0107081.

[DES04] X. Dong, S. Esumi, P. Sorensen, N. Xu, and Z. Xu. "Resonance decay effects on anisotropy parameters." *Phys. Lett.*, **B597**:328–332, 2004. nucl-th/0403030.

[DGV06] Magdalena Djordjevic, Miklos Gyulassy, Ramona Vogt, and Simon Wicks. "Influence of bottom quark jet quenching on single electron tomography of Au + Au." *Phys. Lett.*, **B632**:81–86, 2006. nucl-th/0507019.

[DK01] Yuri L. Dokshitzer and D. E. Kharzeev. "Heavy quark colorimetry of QCD matter." *Phys. Lett.*, **B519**:199–206, 2001. hep-ph/0106202.

[Don05] X Dong. 2005. Ph.D Thesis, University of Science and Technology of China.

[Don06] W.J. Dong. 2006. Ph.D Thesis, University of California, Los Angeles.

[FMN98] Stefano Frixione, Michelangelo L. Mangano, Paolo Nason, and Giovanni Ridolfi. "Heavy-quark production." *Adv. Ser. Direct. High Energy Phys.*, **15**:609–706, 1998. hep-ph/9702287.

[FMN03] R. J. Fries, B. Muller, C. Nonaka, and S. A. Bass. "Hadronization in heavy ion collisions: Recombination and fragmentation of partons." *Phys. Rev. Lett.*, **90**:202303, 2003. nucl-th/0301087.

[GK04] V. Greco and C. M. Ko. "Effect of resonance decays on hadron elliptic flows." *Phys. Rev.*, **C70**:024901, 2004. nucl-th/0402020.

[GKL03] V. Greco, C. M. Ko, and P. Levai. "Parton coalescence and antiproton/pion anomaly at RHIC." *Phys. Rev. Lett.*, **90**:202302, 2003. nucl-th/0301093.

[GKR04] V. Greco, C. M. Ko, and R. Rapp. "Quark coalescence for charmed mesons in ultrarelativistic heavy-ion collisions." *Phys. Lett.*, **B595**:202–208, 2004. nucl-th/0312100.

[Gla03] Leonid Gladilin. "Charm hadronisation in gamma p collisions with ZEUS at HERA." 2003. hep-ex/0309044.

[GVW01] M. Gyulassy, I. Vitev, and X. N. Wang. "High p(T) azimuthal asymmetry in noncentral A + A at RHIC." *Phys. Rev. Lett.*, **86**:2537–2540, 2001. nucl-th/0012092.

[GVW03] Miklos Gyulassy, Ivan Vitev, Xin-Nian Wang, and Ben-Wei Zhang. "Jet quenching and radiative energy loss in dense nuclear matter." 2003. nucl-th/0302077.

[GW73] D. J. Gross and Frank Wilczek. "ULTRAVIOLET BEHAVIOR OF NON-ABELIAN GAUGE THEORIES." *Phys. Rev. Lett.*, **30**:1343–1346, 1973.

[HGR06] Hendrik van Hees, Vincenzo Greco, and Ralf Rapp. "Heavy-quark probes of the quark-gluon plasma at RHIC." *Phys. Rev.*, **C73**:034913, 2006. nucl-th/0508055.

[HKH01] P. Huovinen, P. F. Kolb, Ulrich W. Heinz, P. V. Ruuskanen, and S. A. Voloshin. "Radial and elliptic flow at RHIC: Further predictions." *Phys. Lett.*, **B503**:58–64, 2001. hep-ph/0101136.

[HSS74] J. Hofmann, H. Stocker, W. Scheid, and W. Greiner. 1974. Bear Mountain Workshop, New York.

[HY03a] Rudolph C. Hwa and C. B. Yang. "Scaling behavior at high p(T) and the p/pi ratio." *Phys. Rev.*, **C67**:034902, 2003. nucl-th/0211010.

[HY03b] Rudolph C. Hwa and C. B. Yang. "Scaling distributions of quarks, mesons and proton for all p(T), energy and centrality." *Phys. Rev.*, **C67**:064902, 2003. nucl-th/0302006.

[JW05] Peter Jacobs and Xin-Nian Wang. "Matter in extremis: Ultrarelativistic nuclear collisions at RHIC." *Prog. Part. Nucl. Phys.*, **54**:443–534, 2005. hep-ph/0405125.

[Kar02] Frithjof Karsch. "Lattice QCD at high temperature and density." *Lect. Notes Phys.*, **583**:209–249, 2002. hep-lat/0106019.

[KH03] Peter F. Kolb and Ulrich W. Heinz. "Hydrodynamic description of ultrarelativistic heavy-ion collisions." 2003. nucl-th/0305084.

[Kho04] Alexander Khodjamirian. "Quantum chromodynamics and hadrons: An elementary introduction." 2004. hep-ph/0403145.

[Kir03] J. Kiryluk. "Relative luminosity measurement in STAR and implications for spin asymmetry determinations." *AIP Conf. Proc.*, **675**:424–428, 2003.

[Lee74] T.D. Lee. 1974. Bear Mountain Workshop, New York.

[LK02] Zi-wei Lin and C. M. Ko. "Flavor ordering of elliptic flows at high transverse momentum." *Phys. Rev. Lett.*, **89**:202302, 2002. nucl-th/0207014.

[LM03] Zi-wei Lin and Denes Molnar. "Quark coalescence and elliptic flow of charm hadrons." *Phys. Rev.*, **C68**:044901, 2003. nucl-th/0304045.

[LW74] T. D. Lee and G. C. Wick. "VACUUM STABILITY AND VACUUM EXCITATION IN A SPIN 0 FIELD THEORY." *Phys. Rev.*, **D9**:2291, 1974.

[MFB05] B. Muller, R. J. Fries, and S. A. Bass. "Thermal recombination: Beyond the valence quark approximation." *Phys. Lett.*, **B618**:77–83, 2005. nucl-th/0503003.

[Mus05] Munshi G. Mustafa. "Energy loss of charm quarks in the quark-gluon plasma: Collisional vs radiative." *Phys. Rev.*, **C72**:014905, 2005. hep-ph/0412402.

[MV03] Denes Molnar and Sergei A. Voloshin. "Elliptic flow at large transverse momenta from quark coalescence." *Phys. Rev. Lett.*, **91**:092301, 2003. nucl-th/0302014.

[NO00] Paolo Nason and Carlo Oleari. "A phenomenological study of heavy-quark fragmentation functions in e+ e- annihilation." *Nucl. Phys.*, **B565**:245–266, 2000. hep-ph/9903541.

[NS00] E. Norrbin and T. Sjostrand. "Production and hadronization of heavy quarks." *Eur. Phys. J.*, **C17**:137–161, 2000. hep-ph/0005110.

[Pen95] Olivier Pene. "An Introduction to lattice QCD." 1995. hep-ph/9504271.

[Pol73] H. David Politzer. "RELIABLE PERTURBATIVE RESULTS FOR STRONG INTERACTIONS?" *Phys. Rev. Lett.*, **30**:1346–1349, 1973.

[PSS83] C. Peterson, D. Schlatter, I. Schmitt, and Peter M. Zerwas. "SCALING VIOLATIONS IN INCLUSIVE e+ e- ANNIHILATION SPECTRA." *Phys. Rev.*, **D27**:105, 1983.

[Rap01] R. Rapp. "Signatures of thermal dilepton radiation at RHIC." *Phys. Rev.*, **C63**:054907, 2001. hep-ph/0010101.

[Ris04] Dirk H. Rischke. "The quark-gluon plasma in equilibrium." *Prog. Part. Nucl. Phys.*, **52**:197–296, 2004. nucl-th/0305030.

[RS03] R. Rapp and E. V. Shuryak. "D-meson production from recombination in hadronic collisions." *Phys. Rev.*, **D67**:074036, 2003. hep-ph/0301245.

[Sch04] Kai Schweda. "Highlights from STAR." *J. Phys.*, **G30**:S693–S700, 2004. nucl-ex/0403032.

[Sch06] G. Schroeder. "http://www.bnl.gov/rhic/." 2006.

[Sjo01] Torbjorn Sjostrand et al. "High-energy-physics event generation with PYTHIA 6.1." *Comput. Phys. Commun.*, **135**:238–259, 2001. hep-ph/0010017.

[SLM01] Torbjorn Sjostrand, Leif Lonnblad, and Stephen Mrenna. "PYTHIA 6.2: Physics and manual." 2001. hep-ph/0108264.

[Sor99] H. Sorge. "Highly sensitive centrality dependence of elliptic flow: A novel signature of the phase transition in QCD." *Phys. Rev. Lett.*, **82**:2048–2051, 1999. nucl-th/9812057.

[Sor06] P. R. Sorensen. "Identified particle spectra and jet interactions with the medium." *Nucl. Phys.*, **A774**:247–256, 2006. nucl-ex/0510052.

[Sta] http://www.star.bnl.gov/STAR/html/.

[Tai04] An Tai. "Measurement of open charm production in d + Au collisions at s(NN)**(1/2) = 200-GeV." *J. Phys.*, **G30**:S809–S818, 2004. nucl-ex/0404029.

[TW02] Boris Tomasik and Urs Achim Wiedemann. "Central and non-central HBT from AGS to RHIC." 2002. hep-ph/0210250.

[VBH92] R. Vogt, Stanley J. Brodsky, and Paul Hoyer. "Systematics of charm production in hadronic collisions." *Nucl. Phys.*, **B383**:643–684, 1992.

[VG02] Ivan Vitev and Miklos Gyulassy. "High-p(T) tomography of d + Au and Au + Au at SPS, RHIC, and LHC." *Phys. Rev. Lett.*, **89**:252301, 2002. hep-ph/0209161.

[Vit06] Ivan Vitev. "Testing the theory of QGP-induced energy loss at RHIC and the LHC." *Phys. Lett.*, **B639**:38–45, 2006. hep-ph/0603010.

[Vog02] R. Vogt. "Systematics of heavy quark production at RHIC." 2002. hep-ph/0203151.

[Vog03] R. Vogt. "The A dependence of open charm and bottom production." *Int. J. Mod. Phys.*, **E12**:211–270, 2003. hep-ph/0111271.

[WG92] Xin-Nian Wang and Miklos Gyulassy. "Gluon shadowing and jet quenching in A + A collisions at s**(1/2) = 200-GeV." *Phys. Rev. Lett.*, **68**:1480–1483, 1992.

[WHD05] Simon Wicks, William Horowitz, Magdalena Djordjevic, and Miklos Gyulassy. "Heavy quark tomography of A + A including elastic and inelastic energy loss." 2005. nucl-th/0512076.

[Wil82] Frank Wilczek. "QUANTUM CHROMODYNAMICS (QCD): THE MODERN THEORY OF THE STRONG INTERACTION." *Ann. Rev. Nucl. Part. Sci.*, **32**:177–209, 1982.

[Won94] C. Y. Wong. "Introduction to high-energy heavy ion collisions." 1994. Singapore, Singapore: World Scientific 516 p.

[Xu06] Z. Xu et al. "A heavy flavor tracker for STAR." 2006. LBNL-PUB-5509.

[Zha07] Yifei Zhang. "Identify bottom contribution in non-photonic electron spectra and v(2) from Au Au collisions at RHIC." *Nucl. Phys.*, **A783**:489–492, 2007. hep-ph/0611182.

[Zho07] Chen Zhong. "Scaling of the charm cross-section and modification of charm p(T) spectra at RHIC." 2007. nucl-ex/0702014.

[ZWW04] Ben-Wei Zhang, Enke Wang, and Xin-Nian Wang. "Heavy quark energy loss in nuclear medium." *Phys. Rev. Lett.*, **93**:072301, 2004. nucl-th/0309040.